HARVARD UNIVERSITY
Graduate School of Arts and Sciences

DISSERTATION ACCEPTANCE CERTIFICATE

The undersigned, appointed by the

School of Engineering and Applied Sciences

have examined a dissertation entitled:

"Three-dimensional nanofabrication of silver structures in polymer with direct laser writing "

presented by : Kevin Lalitchandra Vora

candidate for the degree of Doctor of Philosophy and here by certify that it is worthy of acceptance.

Signature _____

Typed name: Professor E. Mazur

Signature _____

Typed name: Professor F. Capasso

Signature _____

Typed name: Professor K. Crozier

Date: *February 24, 2014*

Three-dimensional nanofabrication of silver structures in polymer with direct laser writing

A dissertation presented

by

Kevin Lalitchandra Vora

to

The School of Engineering and Applied Sciences

in partial fulfillment of the requirements

for the degree of

Doctor of Philosophy

in the subject of

Applied Physics

Harvard University

Cambridge, Massachusetts

February 2014

Dissertation advisor: Professor Eric Mazur Kevin Lalitchandra Vora

Three-dimensional nanofabrication of silver structures in polymer with direct laser writing

Abstract

This dissertation describes methodology that significantly improves the state of femtosecond laser writing of metals. The developments address two major shortcomings: poor material quality, and limited 3D patterning capabilities. In two dimensions, we grow monocrystalline silver prisms through femtosecond laser irradiation. We thus demonstrate the ability to create high quality material (with limited number of domains), unlike published reports of 2D structures composed of nanoparticle aggregates. This development has broader implications beyond metal writing, as it demonstrates a one-step fabrication process to localize bottom-up growth of high quality monocrystalline material on a substrate. In three dimensions, we direct laser write fully disconnected 3D silver structures in a polymer matrix. Since the silver structures are embedded in a stable matrix, they are not required to be self-supported, enabling the one-step fabrication of 3D patterns of 3D metal structures that need-not be connected. We demonstrate sub-100-nm silver structures. This latter development addresses a broader limitation in fabrication technologies, where 3D patterning of metal structures is difficult. We demonstrate several 3D silver patterns that cannot be obtained through any other fabrication technique known to us. We expect these advances to contribute to the development of new devices in optics, plasmonics, and metamaterials. With further improvements in the fabrication methods, the list of potential applications broadens to include electronics (e.g. 3D microelectronic circuits), chemistry (e.g. catalysis), and biology (e.g. plasmonic biosensing).

Contents

Citations to published work

Parts of this dissertation cover research reported in the following articles:

1. K. Vora, C. Evans, E. Mazur, "The effects of laser exposure parameters on 3D silver growth in gelatin," *Manuscript in preparation*, 2014.
2. M. Moebius,* K. Vora,* P. Munoz, G. Deng, S. Kang, E. Mazur, "3D optical diffraction gratings and zone plates in gelatin," *Manuscript in preparation*, 2014.
3. K. Vora,* S. Kang,* M. Moebius, E. Mazur, "Femtosecond light-induced growth of hexagonal silver nanocrystals," *Manuscript in preparation*, 2014.
4. S. Kang,* K. Vora,* E. Mazur, "Direct laser writing inside a gelatin matrix for sub-100 nm 3D silver nanostructures," *Manuscript in preparation*, 2014.
5. K. Vora, S. Kang, E. Mazur, "A method to fabricate disconnected silver nanostructures in 3D," *Journal of Visualized Experiments*, 69, e4399, 2012.
6. K. Vora, S. Kang, S. Shukla, E. Mazur, "Fabrication of disconnected three-dimensional silver nanostructures in a polymer matrix," *Applied Physiscs Letters*, 100, 063120, 2012.
7. K. Vora, S. Kang, S. Shukla, E. Mazur, "Three-dimensional silver nanostructure fabrication through multiphoton photoreduction," *Proc. SPIE Frontiers in Ultrafast Optics: Biomedical, Scientific, and Industrial Applications XII* (San Francisco, CA), 824710, 2012.

*co-first authors

Acknowledgements

The past seven years have been a time of tremendous learning and growth for me both professionally and personally. I would not have been able to complete my graduate studies at Harvard without the support and guidance of my advisor, colleagues, thesis committee, friends and—most importantly—my family.

First, I'd like to thank Eric Mazur for his insight and mentorship, and for creating a collaborative, congenial work atmosphere for his graduate students. Eric has been there for the breakthroughs and the stumbling blocks, and for that I am grateful. My labmates with whom I worked over the years—Michael Moebius, SeungYeon Kang, Phil Munoz, Shobha Shukla, Chris Evans, Guoliang Deng, Renee Sher, Yu-Ting Lin, Eric Diebold, Yang Li, Levent Sahin, Ravi Bathe, Bongchul Kang—are a brilliant group of scientists. It has been a true pleasure working with them. The Mazur group is made up of scholars who are dedicated both to their research and to one another. Thank you to Jason Dowd, Paul Peng, Kasey Phillips, Jin Suntivich, Thierry Sarnet, Haifei Zhang, Ben Franta, Kelly Miller, Hemi Gandhi, Sebastien Courvoisier, Sarah Griesse-Nascimento, Nabiha Saklayen, Julie Schell, Laura Tucker, Brian Lukoff, Prakriti Tayalia, Cleber Mendonca, James Fraser, Orad Reshef, and Virginia Casas for making the group such a fulfilling place to spend the last seven years. I would also like to thank Marko Loncar, Jonathan Fan and Jeremy Munday for mentoring me when I started my graduate studies at Harvard, and Federico Capasso and Ken Crozier for guiding me from the beginning to the end as part of my thesis committee.

Being at Harvard has given me the opportunity to explore academic interests outside of my research in a deeply fulfilling way. Thank you to my mentors, Fawwaz Habbal and Paul Bottino, for sharing your time and knowledge with me. Similarly, in my time as a Dudley Fellow, I was able to connect with a wide network of the amazing students at the University. Thank you to Susan Zawalich and Garth McCavana for your confidence in me.

Lastly, I would like to thank my friends—especially Mary Ruth, Alison, Stephanie, Chryssi, and Anton—and family—my parents and my brother. I could not have completed this journey without your support. I want to especially express my gratitude to Erin. Thank you for your support and encouragement, especially towards the end. I am indebted to all of you for your love, support and encouragement through everything. I could not have done it without you. Thank you.

Kevin Vora

Cambridge, Massachusetts

February 2014

Acknowledgements of Financial Support

The research described in this thesis was supported by the AFOSR under grants FA9550-09-1-0546 and FA9550-10-1-0402, with additional funding from the Harvard University Center for the Environment, and the Fonds Québécois de la Recherche sur la Nature et les Technologies.

To my loving family.

Chapter 1

Introduction

Fabrication methods, whether macroscopic or microscopic, are critical to the development of technology because they allow theories to be tested and applied into real-world applications. There is a constant need for pushing the boundaries of the materials we can manipulate, and the scales at which we can manipulate them.

Recent progress in, for example, metamaterials, plasmonics, and more broadly, optics, has highlighted the need for further developments in fabrication technologies. Metamaterial theorists have designed perfect absorbers, perfect lenses, terahertz antennas, and invisibility cloaks, which have led to the need to pattern composite materials in three-dimensions with micro- and nano-scale feature sizes [1]. These new needs in fabrication technology motivated us to explore femtosecond laser processing to expand the scope of structures that could be realized through direct laser writing. More specifically, we focused on metal fabrication through femtosecond laser pulse irradiation, which has thoroughly lacked development compared to femtosecond laser glass micromachining and two-photon polymerization. Although our original motivation was to develop a technique that could create optical devices, broader potential applications include electronics,

biology and chemistry. Examples include three-dimensional (3D) microelectronic circuits, plasmonic biosensors, and chemical catalysis.

We present femtosecond laser processing methods to fabricate metal micro- and nano-structures in both two- and three-dimensions using ultrashort laser pulses. The methods allow us to create structures that were not possible through alternate techniques. We use high-intensity femtosecond laser pulses to induce the reduction of metal ions through multiphoton absorption. We are able to create structures that range from sizes much smaller than the diffraction limit of light, to several times the laser beam spot size. Metal photoreduction can also be achieved through an ultraviolet light source. However, the non-linear nature of the multiphoton process allows us to access the bulk of a material, thus propelling the technique to three dimensions under certain conditions. This thesis outlines the fabrication processes we have developed, the various experiments we have conducted, as well as the results we have obtained.

1.1 Research motivation

Developments in fabrication methods are critical to the progression of scientific research and technology. Advancing research in many fields now relies on the manipulation of matter at micrometer and sub-micrometer scales. Micro- and nano-fabrication play crucial roles in fields ranging from electronics, to photonics, to chemistry, to biology.

Standard nanofabrication toolkits available to scientists contain several bottom-up and top-down techniques that enable material synthesis or high resolution patterning. Bottom-up methods can be used to make large quantities of nanoparticles through liquid phase synthesis. Top-down approaches are usually used to pattern complicated nanosystems. There are too many techniques

to enumerate here (which is beyond the scope of this thesis), but electron beam lithography (EBL) and ultraviolet (UV) photolithography are two examples of commonly used patterning methods. EBL produces patterns in dielectric media with very high resolutions. It can be used in combination with metal deposition steps, for example, to create high resolution metal patterns. UV photolithography produces micron scale structures in polymers over large areas. It can also be used in combination with metal deposition steps, for example, to create metal patterns over large areas. EBL is primarily used for applications requiring high resolution 2D patterns, whereas UV photolithography is preferred for scalability.

Many new applications require patterning in three dimensions: one such example is the emerging field of metamaterials. Metamaterials have been the subject of significant research recently because of the strange and sometimes counterintuitive behavior exhibited by electromagnetic waves propagating through them. Their properties are engineered for tailored electromagnetic responses which cannot usually be found in nature. Metamaterials are composed of arrays of unit cells, each cell with a size that is typically an order of magnitude smaller than the operating wavelength. Manipulating visible and infrared light requires that unit cells be comprised of nanostructures with sizes on the order of 40–2,000 nanometers. Researchers have relied heavily on EBL and UV photolithography in combination with material deposition steps for creating metamaterials. EBL is used when very high resolution is necessary, and UV photolithography is used when the resolution requirements are on the micron scale. Many metamaterial applications require metal and dielectric structures, thus requiring multiple material deposition steps. Furthermore, many applications require a large number of layers in order to create bulk devices (where a single layer can be compared to the equivalent of a monolayer of material). This requires

a large number of processing steps during fabrication since EBL and UV photolithography are inherently 2D. For example, steps to create planar metal structures using ultraviolet photolithography and electron-beam lithography can include sample exposure, sample development, metal deposition, and metal liftoff. To create 3D metal patterns, the sequence is repeated multiple times while adding additional material deposition steps. The complexity and difficulty of stacking and aligning multiple layers (which is not flat after a layer is patterned) limits practical implementations of 3D metal structuring using standard nanofabrication tools, especially if the individual micro- and nanostructures themselves have 3D depth.

To overcome these fabrication limitations, some researchers have turned to two-photon polymerization (TPP), which enables the direct patterning of 3D polymer structures [2, 3]. This is an emerging method that has seen rapid development over the past decade. A resin, usually a negative-tone photoresist, is coated onto a substrate, and irradiated with femtosecond laser pulses. A two-photon absorption process initiates oligomer polymerization or polymer chain crosslinking, depending on the specific type of negative-tone resist. The sample is then bathed in a solvent, leaving behind a polymer pattern created by the laser. In the structure, there are open voids in between polymer structures that can be filled with other materials. For example, TPP has been skillfully used in combination with chemical vapor deposition and electroplating [4, 5] to create 3D metal-dielectric metamaterials.

Although TPP provides an avenue to create 3D samples, the technique is unable to produce vertically disconnected 3D structures: 3D placement of 3D metal structures that are not connected to each other, including those stacked on top of each other, as opposed to 3D metal structures positioned in 2D. Such disconnected metal structures are necessary for realizing certain types of

metamaterials in bulk [1]. This example highlights a broader practical limitation of current micro- and nanofabrication tools: the difficulty of producing 3D metal patterns, particularly those with metal features that are disconnected from each other in all three spatial dimensions.

Femtosecond lasers have been used to grow metal structures directly [6-12]. However, several fabrication hurdles have limited the development and use of these techniques. At an MRS conference in 2012, Georg von Freymann, a prominent scientist in TPP and metamaterials [3-5], once colloquially referred to direct laser writing of high quality metals in 3D with high resolution as "the Holy Grail" for metamaterial fabrication. The combination of need and opportunity was the basis for our exploration of femtosecond laser fabrication of silver. We applied the accumulated expertise in our research group in direct laser writing [13] towards exploring new silver writing methods for both two and three dimensions. The emerging field of metamaterials, which provided our original motivation, more broadly helped us recognize limitations in fabrication technology that we could contribute towards. We hope our developments will spur increased research interest in femtosecond laser fabrication of metals and its applications.

1.2 2D and 3D metal patterning

The standard nanofabrication toolkit includes techniques primarily aimed at creating 2D patterns in dielectric media. Creating metal patterns on a submicron scale requires a combination of several fabrication tools and material processing steps. For example, steps to create planar metal structures using UV photolithography and EBL can include sample exposure, sample development, metal deposition, and metal liftoff. To create 3D metal structures, the sequence is repeated multiple times, with several additional steps. The complexity and difficulty of stacking and aligning

multiple layers (which are normally not flat after being patterned) limits practical implementations of 3D metal structuring using standard nanofabrication tools.

Table 1 lists a few methods used to create metal patterns. From the table it can be seen that many options exist to create metal patterns at micro- and nanometer scales; most metal-containing devices can be made using any one of these techniques. Unfortunately, there exist gaps these methods cannot fill. For example, a simple process for growing high quality single crystal silver particles at specific positions on a substrate that could be used for plasmonics devices, or a process for creating silver patterns with disconnected unit cells in three dimensions for bulk metamaterial applications. Some applications may be sensitive to processing conditions (e.g. chemical reagents or temperatures) that make them incompatible with the options in Table 1. Other applications may require a combination of nanoscale feature sizes and large areas that cannot be produced by these techniques. There are several opportunities to broaden the scope of devices that can be created through advances in metal fabrication. Femtosecond laser direct writing of metals has been omitted from Table 1 since it is the subject of this thesis and is described later.

Table 1: Comparison of a few common metal micro- and nanofabrication technologies.

Technology	**Characteristics**
UV photolithography used with metal deposition and liftoff or etching.	Can pattern large areas in 2D. Many steps involved in the creation of a single layer pattern. Multiple layers can be patterned on top of each other, but difficult to create more than a handful of layers, or complex 3D structures. Harsh chemicals are required for the processing steps. Features sizes are on the order of 500 nm and larger.
Deep and extreme UV photolithography used with metal deposition and liftoff or etching.	Can achieve much higher resolution than UV photolithography, but the cost is much higher. Commonly used for applications at scale.
Nanoimprint lithography used with metal deposition.	Can achieve very high resolution with low costs. Can produce 2D and simple 3D structures (subject to distortion) in a 2D pattern. Requires multiple steps.
EBL used with metal deposition and liftoff or etching.	Very high resolution. Can pattern small areas, or stitch together smaller patterns to create larger samples in 2D. Multiple steps are involved, and layered fabrication is difficult for 3D.
Focused ion-beam (FIB) lithography used with multiple material deposition steps.	Very high resolution. To achieve 3D structure, multiple materials can be layered through deposition steps, and patterned through material removal with FIB. Many steps are involved, and only simple 3D patterns can be created.
TPP used with metal deposition.	Can create complex 3D samples. However, to fill voids with metals, the voids must be accessible—connected such that material can enter. This precludes the ability to pattern disconnected metal structures in 3D.
Direct-write assembly using conductive ink.	Can pattern large areas in 3D, including on curved surfaces. Metal fabrication is limited to features sizes on order of 2 μm. Cannot create disconnected metal structures in 3D.
Bottom-up methods (broadly encompassing chemical synthesis methods).	Many chemical methods exist for growing metal particles. They can be inexpensive, and produce high volumes of material with high quality (such as single crystal growth). However, the techniques do not enable arbitrary patterning as top-down methods do.

The table lists two techniques that are inherently 3D: TPP and direct-write assembly. As discussed previously, metal deposition can be added to the TPP process to create metal patterns.

However, there is a limitation when disconnected metal structures are required. Direct-write assembly, which prints structures through a small nozzle, can directly create 3D metal structures with a resolution around 2 μm [14]. However, the method cannot achieve submicron metal features or create disconnected metal patterns in the vertical direction. These limitations can be overcome through the direct laser writing of metals.

1.3 Dissertation development and objectives

Femtosecond laser fabrication has been developed significantly over the past two decades for patterning glasses and polymers in 3D. However, the development of metal fabrication with femtosecond lasers has lagged significantly. The aim of our work was to develop metal fabrication to overcome several obstacles that may have contributed to slowing developments in this area. We present experimental work we hope will spur significantly more interest and research in using femtosecond lasers to fabricate metals in 2D and 3D given the unique samples that can be generated. The research described in this thesis shows significant developments in both 2D and 3D laser writing of silver. We hope future work will concentrate on improving the methods and techniques discussed in this thesis to create practical devices.

1.4 Organization of the dissertation

This dissertation reports our developments in femtosecond laser fabrication of silver in two- and three-dimensions. We also demonstrate diffractive structures fabricated using these methods.

Chapter 2 is an overview of background information on femtosecond laser fabrication of metals and describes the main experimental methods used in this research.

Chapter 3 describes our work in 2D fabrication of silver. We describe and compare our results with previous work and show our developments in 2D metal laser fabrication: we produce crystalline silver growth through irradiation with femtosecond light.

Chapter 4 describes our work in 3D fabrication of silver. We describe the new capabilities we have developed that allow for the fabrication of disconnected silver nanostructures inside polymer.

Chapter 5 explores the effect of pulse energy and exposure time on silver fabrication in gelatin. We show that both linear and nonlinear absorption are important to silver growth. We further expand on the 3D fabrication capabilities of the method.

Chapter 6 reports on simple applications of the fabrication technique. We fabricate and characterize 3D diffraction gratings and zone plates. We also fabricate patterns based on metamaterial designs.

Chapter 7 concludes and summarizes the dissertation and provides an outlook for future work.

Chapter 2

Background and methods

In this chapter, we discuss background information about femtosecond laser fabrication, with an emphasis on the femtosecond laser fabrication of metals. We also discuss the materials preparation methods, optical setup, and characterization techniques we used for the research discussed in this thesis.

2.1 Defining spatial dimensionality

A variety of methods exist to create patterns in two- and three-dimensions. Before embarking on a brief discussion of some of these techniques, we will make several distinctions in the terminology used to describe dimensionality, as the terms two-dimensional and three-dimensional are often used without considering important subtleties.

2D fabrication typically leads to creating structures in a plane, even though these structures have non-zero size in the normal direction. These fabricated structures are usually either 2D shapes with some depth, or simple 3D structures (with hemispherical or triangular shapes in the third dimension, for example). Thus, a 2D technique typically produces 2D patterns of simple 3D structures (Figure 1a and Figure 1b).

Chapter 2 - Background and methods

Typically, any sample with significant depth in the *z*-dimension, in addition to spanning the *x* and *y* dimensions, is viewed as being 3D. However, we distinguish between three types of 3D structures. Figure 1 shows examples of the distinctions we make. The first type of 3D structure can be broken down as a 2D pattern of 3D structures, such as the one shown in Figure 1c. The second type is a more complex 3D structure that has significant depth, and cannot necessarily be considered a 2D array (Figure 1d). All these structures are self-supporting. The scope of these first two types of 3D objects can overlap; the most important distinction comes with the third type of 3D pattern. This type includes 3D structures that are disconnected in all three spatial dimensions. They are embedded structures that can be stacked in the vertical direction without being connected. One example includes glass with a 3D pattern of voids, or higher index glass, embedded inside. Another example includes a composite material with one material patterned and embedded inside another. In this type of pattern, the structures do not need to be self-supporting since they are embedded in a background matrix: it is possible to create 3D arrays of 2D or 3D structures as well as more complex 3D patterns that can be stacked above one another without being connected. We refer to these structures as being disconnected in all three spatial dimensions (Figure 1e).

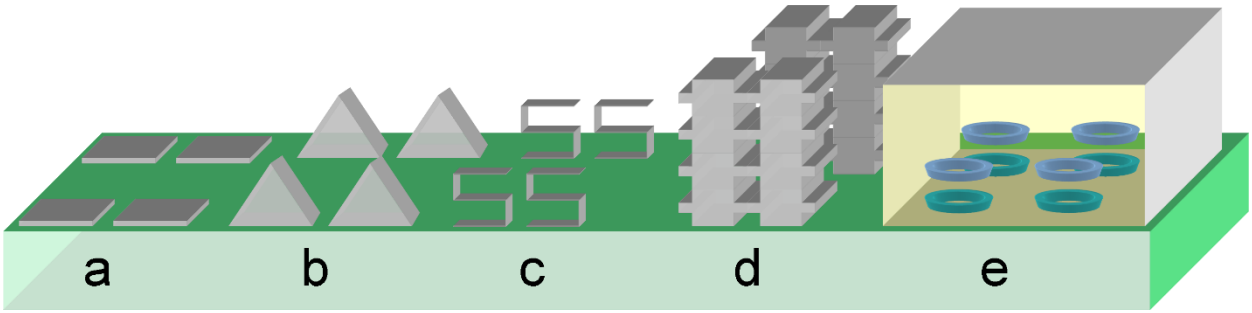

Figure 1: Schematics of (a) simple 2D pattern, (b) 2D pattern of silver 3D structures, (c) 2D pattern of complex 3D structures, (d) 3D self-supporting pattern and (e) 3D pattern of disconnected structure.

The example in Figure 1e shows horizontally oriented rings. These types of rings may be created through a repetition of several planar processes. However, if there are additional layers, or if the rings are oriented vertically, the pattern becomes much more difficult, or even impossible, to realize through planar techniques.

2.2 Femtosecond laser fabrication

Intense femtosecond laser pulses can be absorbed in transparent materials and modify their refractive properties through nonlinear light-matter interactions. Because the target materials are transparent to the laser wavelength, the pulses can be focused at arbitrary points in the bulk (Figure 2). Thus, devices can be patterned in three dimensions using *x*-, *y*- and *z*-translation. In glass, multi-photon absorption of femtosecond laser pulses leads to densification that is localized to the focal volume of the beam [15-17]. This approach to material modification can be used in a variety of applications: examples of three-dimensionally integrated optical components using this technique include waveguides, splitters, couplers, interferometers and data storage devices [15-17]. Patterns include waveguides as long as 30 mm (limited by sample size) and sub-micrometer dots [15-17].

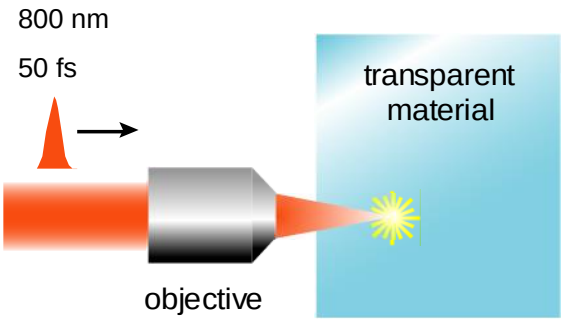

Figure 2: A femtosecond laser pulse tightly focused in the bulk of a transparent material used for micromachining through nonlinear absorption. Adapted from Reference [13].

The same fabrication principle—multiphoton absorption inside transparent media—can be used to fabricate freestanding structures. As described in Chapter 1, in TPP, a substrate is coated with a resin and photoinitiator mixture, and then irradiated with tightly focused femtosecond laser pulses. The resin contained within the focal volume of a pulse polymerizes via two-photon absorption in the photoinitiator (assuming that the resin is a negative-tone resist). By controlling the position of the focus with a three-axis translation stage, we can fabricate complex polymeric microstructures in three-dimensions [18, 19]. An example of a 3D polymer pattern is shown in Figure 3**.**

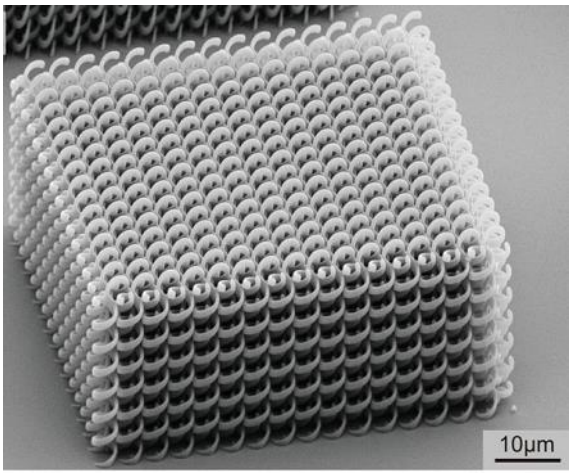

Figure 3: Scanning electron micrograph of femtosecond laser fabricated 3D polymer structures. Adapted from Reference [3].

Nonlinear optical absorption can also be used to grow metal. A dielectric material—water, glass, or polymer, for example—is mixed with metal ions and irradiated with femtosecond laser pulses to grow metal structures through multi-photon induced reduction. This process begins in a small volume where the laser is most intensely focused, allowing the fabrication of structures smaller than the diffraction limit of light. Figure 3 shows a scanning electron microscopy (SEM) image of large 2D silver lines drawn on a glass substrate using this process.

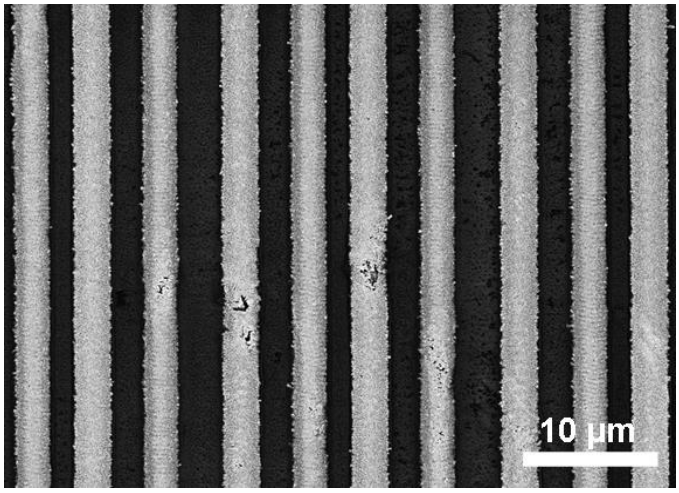

Figure 4: SEM image of silver lines written on a glass substrate with femtosecond laser irradiation.

To gain some insight into the relative developmental stages of the three aforementioned areas of femtosecond laser fabrication, we can look at their relative numbers of publications. Simple searches on Web of Science, on January 1, 2014, for *two-photon polymerization* and *femtosecond micromachining* showed 1,035 and 740 publications, respectively. For comparison, the number of publications on direct metal writing with femtosecond laser pulses is on the order of 20 [2]. To add further perspective on the developmental stage of metal writing, we note that despite the large amount of research on TPP, there are still unknowns towards fully understanding TPP processes [20]. As it currently stands, the field of direct laser writing of metals is underdeveloped.

2.3 Multiphoton absorption

Light can propagate through a transparent material because there is little to no single-photon absorption. However, if the intensity of light is high enough, it can be absorbed through a nonlinear process: multiphoton absorption (MPA). MPA was predicted theoretically in 1931 by Maria

Goppert-Mayer [21]. MPA depends nonlinearly upon the intensity of light, and thus can be located inside the bulk of a transparent medium. If the pulses are focused in a material with a microscope objective, it is possible to localize photochemical or photophysical changes to a focal volume inside the material.

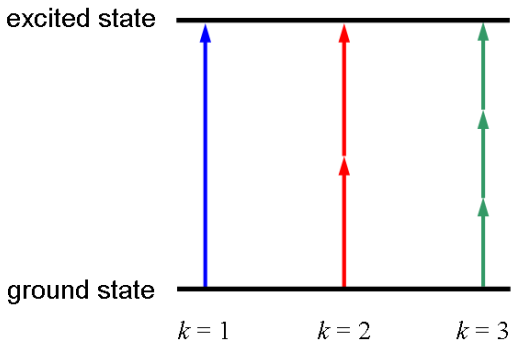

Figure 5: Diagram of the excitation of electrons from the ground state to an excited state during absoprtion. Absorption is proportional to the k^{th} power of the intensity, where k is the number of photons absorbed simultaneously.

In MPA, two or more photons collectively bridge an energy gap to drive an electronic transition; they are absorbed simultaneously (Figure 5). The absorption depends on the intensity of light. For example, in a two-photon process, two photons in sum have in the requisite amount of energy to drive a transition. The absorption cross section σ is proportional to the intensity of light,

$$\sigma = \sigma^{(2)} I, \tag{2.1}$$

where $\sigma^{(2)}$ is a coefficient that describes the strength of the two-photon absorption process and I is the laser intensity. The atomic transition rate R scales with

$$R = \frac{\sigma I}{\hbar\omega} = \frac{\sigma^{(2)} I^2}{\hbar\omega} \tag{2.2}$$

for two-photon absorption [22], where $\hbar$ is the reduced Planck constant, and ω is the photon angular frequency. Two-photon absorption is thus proportional to the square of the intensity of the laser. This relationship can be extrapolated to higher orders of multiphoton absorption.

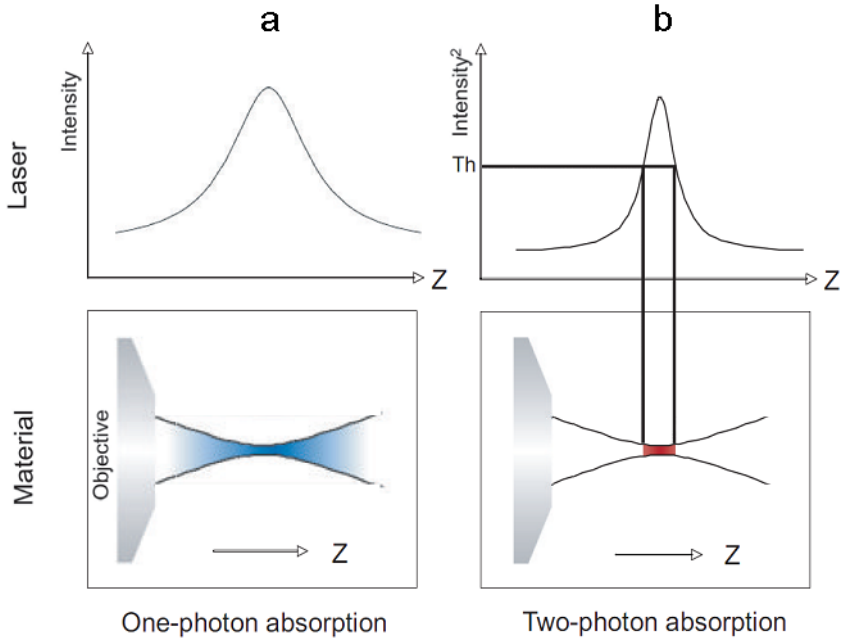

Figure 6: (a) Photons with sufficient energy are linearly absorbed throughout the beam path. (b) Photons with insufficient energy are only absorbed in a small high intensity volume through nonlinear processes. Adapted from Reference [23].

The absorption cross-section for MPA is very small (many orders of magnitude smaller than the cross-section for linear absorption at wavelengths where single photons can be absorbed). The high intensity required for nonlinear absorption can be obtained with ultrafast lasers. Thus, when a femtosecond laser pulse is tightly focused inside a transparent material with a microscope objective, it is possible to obtain nonlinear absorption in a small focal volume in the bulk of the material.

Figure 6 illustrates how the intensity dependence of absorption can be used to spatially localize the absorption process. A microscope objective focuses laser light toward the right, and

the corresponding intensity for the beam profile is plotted below the diagram. The intensity (which is a function of power and beam spot size) peaks at the focus, where the cross-sectional area is minimized. Linear absorption is directly proportional to the intensity and will occur throughout the beam path in the sample (shaded in blue in Figure 6a). Standard optical techniques rely on linear absorption. In the nonlinear case, MPA occurs in regions of high intensity. Thus, when the laser pulse energy is chosen carefully, absorption can be localized to a small focal volume (area shaded in red in Figure 6b shows an example of two-photon absorption) where the intensity is high enough. The effect becomes more dramatic for higher orders of absorption. For material modification processes that have an energy threshold, the material before and after the laser focus remains unmodified. The pulse energy must be chosen to provide high enough intensity for material modification in the desired volume, and low enough to avoid MPA further away.

In femtosecond laser direct writing, the laser wavelength is chosen such that photons are not linearly absorbed in the target medium. When the laser pulse duration is compressed to the femtosecond time scale and the radiation is tightly focused inside the target, the high intensity induces a significant amount of MPA, which leads to material modification. Using this approach, one can create structures in the bulk of a material rather than on its surface.

2.4 Femtosecond laser metal writing

Several reports describe direct laser writing of metals with femtosecond laser pulses. The methods can be separated into two broad categories: fabrication in liquid, and fabrication in a matrix.

The group of S. Kawata has published several reports of femtosecond laser metal fabrication in an aqueous solution [6, 7, 9, 10]. Their chemical preparations range from a simple

mixture of silver nitrate in water [9], to including two-photon dyes [10], surfactants [6], and fatty salts[7]. Figure 7 shows an image of their results with silver nitrate in water: they obtain sub-micrometer resolution, but there is a large variability in shape and roughness at all sizes. Their chemical iterations yield some improvements in resolution (to approximately 200 nm) [6], but there is no improvement in the morphology of the silver structures. This highlights a shortcoming of patterning silver inside a liquid: turbulence and bubble formation in the liquid can have a negative impact on metal features. For example, metal particle growth can be rapidly followed by bubble formation that destroys nearby patterns [9]. Structures fabricated in a liquid solution also need to be self-supporting.

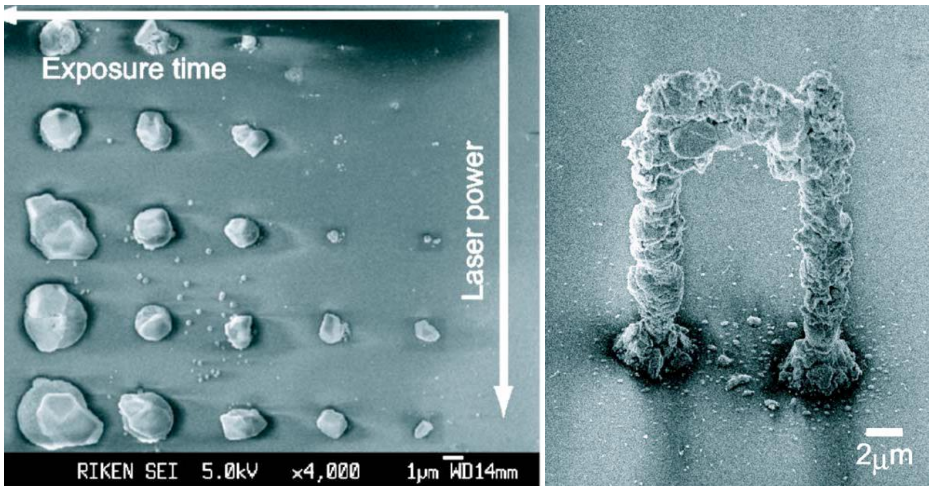

Figure 7: Silver fabrication in an aqueous solution of $AgNO_3$ through irradiation of femtosecond laser pulses. Adapted from Reference [9].

Metals can also be fabricated inside a matrix. The choice of the matrix material is crucial for the generation of metal structures in solids. Metal patterning inside hard inorganic solids remains a challenge because of poor mobility of metal blocks or dispersed ions: high mobility is necessary for the metal assembly process [24].

Stellacci et al. show 3D fabrication in a polyvinylcarbazole matrix containing a combination of $AgBF_4$, alkanethiol-coated silver nanoparticle seeds, and a photoreducing dye [12]. They demonstrate the microfabrication of a woodpile structure with a resolution of approximately 2 μm. However, conductivity measurements show their material has a resistivity value three orders of magnitude larger than bulk silver [12]. Thus, the material composition of their fabricated structure is uncertain.

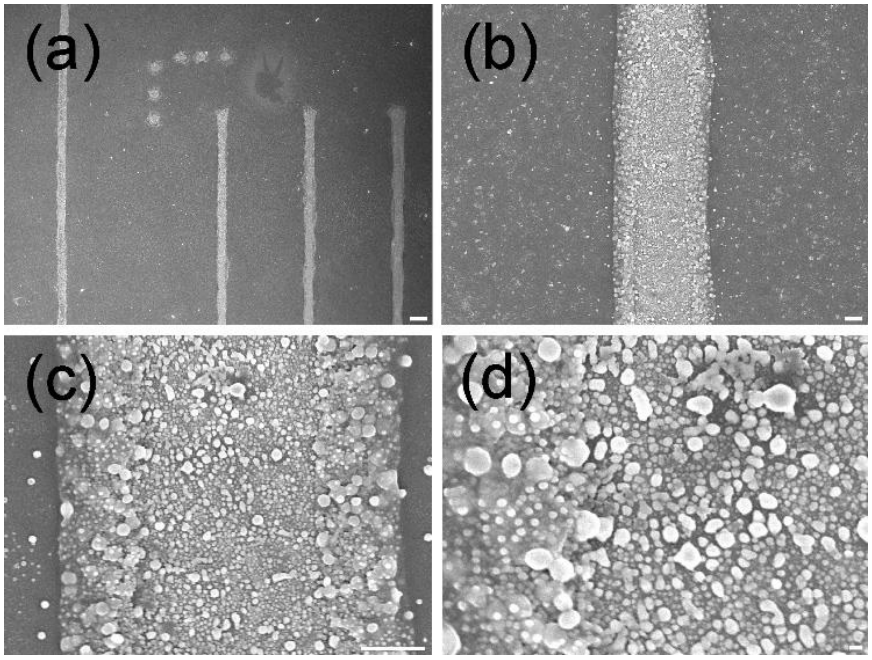

Figure 8: SEM images of representative photodeposited silver structures at different degrees of magnification. Panels (b)-(d) show close-ups of the second line from the left in panel (a). The lengths of the scale bars are 10 μm in (a), 1 μm in (b) and (c), and 100 nm in (d). Adapted from Reference [11].

Baldacchini et al. use a mixture of $AgNO_3$, ethanol, water, and PVP for femtosecond laser writing silver [11]. They use an excitation source centered at 780 nm producing 250 fs pulses at a 76 MHz repetition rate and an average power of 35 mW. They show 5 μm lines, where the lines are sparse aggregates of silver nanoparticles (as shown in Figure 8) [11]. They suggest a growth

process through a combination of multiphoton absorption and local heating because silver growth was not obtained when the laser was not modelocked, and the feature sizes were much larger than the diffraction limited spot size. Maruo et al. use the same chemistry as Baldacchini et al. and demonstrate sub-micrometer linewidths by using tight laser focusing (with a numerical aperture of 1.25) [8]. The sub-micrometer lines are also aggregates of silver nanoparticles. They show larger linewidth features to be electrically conductive, with a resistivity 22 times higher than bulk silver. Their laser produces 200 fs pulses centered at 752 nm with a 76-MHz repetition rate, and an average power between 1 and 5 mW. Their stage translation speeds range between 1 and 100 μm/s. In both reports of silver growth in PVP, the PVP matrix must be removed after patterning. The samples degrade very quickly at ambient conditions and become opaque. Thus, this specific chemical formulation is not suited to provide a support matrix for fabricated silver structures.

The methods described here for femtosecond laser metal writing show that it is possible to grow metals using femtosecond laser pulses. However, none of them allow for the patterning of disconnected metal nanostructures in 3D because of one or more of the following issues: absence of a support matrix, large feature size, or poor structure morphology.

2.5 Materials, sample preparation, and optical setup

This section provides a general outline of the experimental methods used for sample preparation and fabrication. Exact chemicals and preparation parameters are tuned for specific experiments, and specified in the relevant chapters.

This section covers research reported in: K. Vora, S. Kang, and E. Mazur, "A method to fabricate disconnected silver nanostructures in 3D," *Journal of Visualized Experiments,* 69, e4399, 2012.

2.5.1 Substrate preparation

The substrates onto which the metal-ion doped polymer films are coated need to be optically transparent, flat, and rigid. The transparency allows in-situ imaging during fabrication. The flatness and rigidity are necessary so that coatings can be applied uniformly and repeatably onto the substrate. We primarily use clear microscopy glass slides. The slides are treated through plasma cleaning, and silanization with (3-acryloxypropyl)trimethoxysilane. The process takes several hours to complete, and improves the adhesion of silver to the surface.

2.5.2 Preparation of metal-ion doped polymer film

The reagent list required for chemical preparation is relatively simple. The preparation requires a metal precursor, a polymer and one or more solvents. The polymer will constitute the background matrix of the sample, and the metal precursor will be the source of metal ions that are reduced when irradiated. The polymer and metal precursor sometimes require different solvents. The following steps describe a specific example where we use the same solvent for the polymer and metal precursor, polyvinylpyrrolidone (PVP), and silver nitrate ($AgNO_3$), respectively. Both chemicals are in powder form.

1. Measure 8 mL of deionized water in a beaker.
2. Add 206 mg of PVP to water. Mix using magnetic stirrer or vortex mixer until the solution is clear.

3. Add 210 mg of $AgNO_3$ to solution. Mix using magnetic stirrer or vortex mixer until solution is clear. The $AgNO_3$ concentration is 0.155 M.
4. Keep the solution at room temperature in an area devoid of UV light to minimize degradation.

During step 3, the silver salt is dissociated into its ionic constituents, Ag^+ and NO_3^-, which disperse throughout the solvent. Thorough mixing is required to ensure full dissolution and uniform distribution in the mixture. At this stage, the mixture is a liquid solution due to an excess amount of water. In the next part of the process, we coat the substrate with the solution through one of two methods: spin coating or drop casting. Spin coating creates thin film coatings (on the order of 1 μm), whereas drop casting leads to thicker samples (on the order of 10 μm and thicker). The following steps describe the process we use to complete sample preparation for 3D patterning:

1. Place substrate on a flat surface. Use a pipette to coat glass slide with the liquid solution through drop casting (on the order of milliliters, depending on size of glass slide). For example, one milliliter of solution on a 2.5 cm x 2.5 cm glass slide approximately yields a 15-μm thick film through drop casting.
2. Place glass slide on a flat surface inside an oven set at 100 °C. Bake sample for 30 min.
3. Remove sample from oven and let cool for 30 min.

During the baking process, the solvent evaporates and leaves behind a solid film. If the baking and cooling times are insufficient, there will be undesired effects during fabrication: laser irradiation will lead to the formation of large bubbles (on the order of tens to hundreds of microns in size).

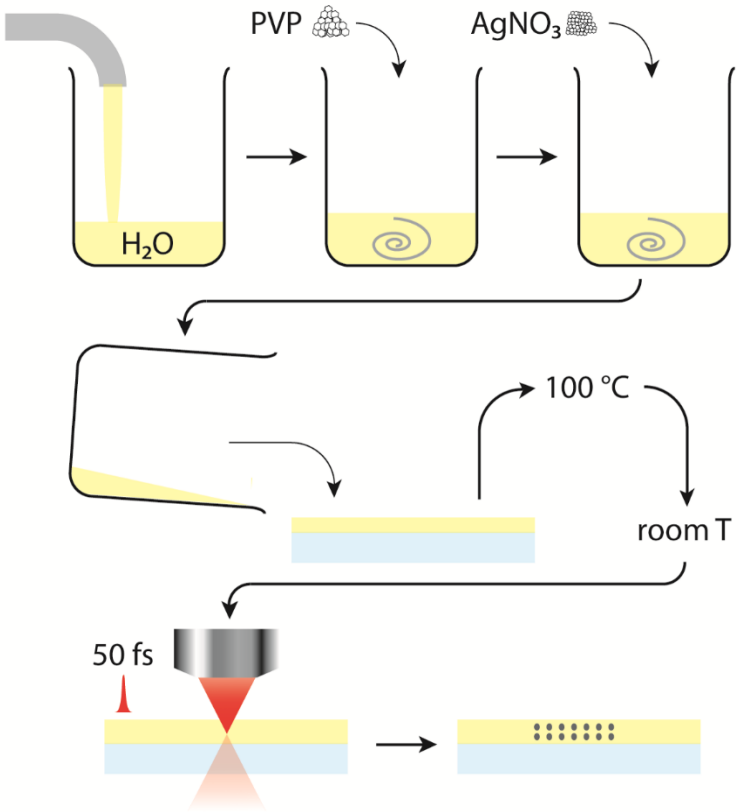

Figure 9: Diagram illustrating sample preparation. A sample is prepared by coating a glass slide with a mixture of PVP, $AgNO_3$, and H_2O. Once the sample is prepared, patterning is a single-step process.

The doped polymer film is now ready for patterning with femtosecond laser pulses. The diagram in Figure 9 illustrates steps from the sample preparation process. The steps and equipment required for sample preparation are relatively simple once the correct chemical formulation is developed.

2.5.3 Optical setup

This section details the optical setup we use to fabricate samples. Our fabrication setup is similar to those used by other research groups for TPP and glass micromachining. Figure 10 shows a schematic of our fabrication setup. The primary components of the setup include a femtosecond

laser, a Faraday isolator, a pulse compressor, an acousto-optic modulator (AOM), a set of neutral-density (ND) filters, a home-built microscope, a camera, and a high precision 3-axis translation stage. The entire setup is fixed to an optical table mounted on vibration isolators. Mirrors and lenses with dielectric coatings are used throughout the beam path.

We use a Ti:sapphire laser system that produces 50-fs pulses with a 795 nm center wavelength and 11 MHz repetition rate. A polarization-sensitive Faraday isolator is used to minimize back reflections produced by the beam path from entering the laser cavity.

The short femtosecond pulses undergo dispersion as they propagate through the various optical elements of the setup. A pulse shaper allows us to pre-compensate for the dispersion, ensuring the shortest possible pulse at the sample. The pulse shaper uses a spatial light modulator to vary the phase of different spectral components of the pulse. It allows for the compensation of high order dispersion, as well as the flexibility to produce complex pulse patterns. We have also used a prism compressor to perform the pre-compensation.

Both AOM and ND filters control the total laser exposure of samples. In our setup, the AOM serves a similar function to that of a mechanical shutter: it determines whether the laser beam travels along the optical path to the microscope. When in the beam path, the laser irradiation reaches the sample; otherwise, the optical power is dumped in a beam block. Mechanical shutters typically operate in the kilohertz frequency range, whereas an AOM can operate with megahertz frequency. The AOM allows us to control the exposure of samples with position and time. The set of ND filters following the AOM are used to attenuate the laser beam, and control the average power reaching the sample.

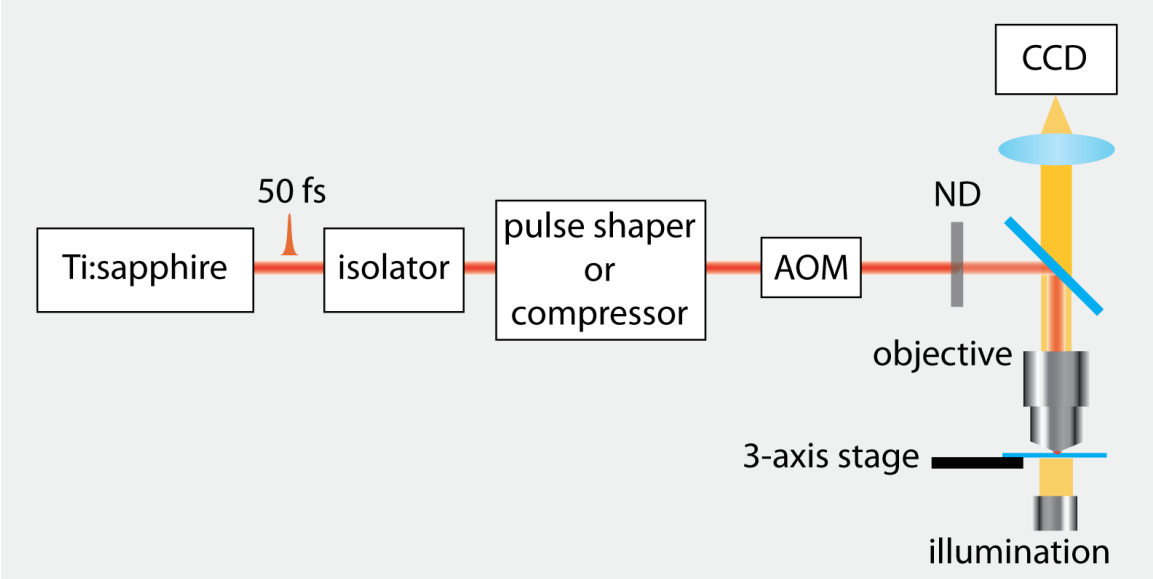

Figure 10: Laser fabrication setup. The primary components of our fabrication setup include a femtosecond laser, a Faraday isolator, a compressor, an AOM, a ND filter, a microscope with camera, a high precision 3-axis translation stage, and an optical table mounted on vibration isolators. The laser produces 50-fs laser pulses centered at 800 nm with a repetition rate of 11 MHz. The compressor pre-compensates for the dispersion in the optical beam path to obtain 50-fs pulses at the sample. The AOM and ND filter function as a shutter and an attenuator to control the laser exposure of the sample. We use a 0.8-NA microscope objective to simultaneously focus the laser beam and image the sample during fabrication. The sample position is controlled by a high-precision 3-axis translation stage.

We use a home-built microscope to simultaneously focus the laser beam and image the sample during fabrication. The microscope has an upright, transmission design. The main pieces of the microscope include an illumination source, a digital grayscale camera, and an objective. The microscope objective has a numerical aperture (NA) of 0.8. The sample position is controlled by a high-precision 3-axis air-bearing translation stage. The stage provides a combination of high resolution positioning and long travel distances in the x-, y- and z-directions.

Several measures are taken to mitigate environmental impacts on the performance of the optical elements. The laser is very sensitive to humidity, air flow, and temperature, which can affect the fabrication process. The stage is mounted on a 4-inch slab of polished granite, which

provides the flatness necessary to maintain high resolution positioning of the stage. The entire setup is mounted on an optical table with vibration isolation; vibration isolation is required to minimize noise in both sample and laser beam positioning. A computer is used to simultaneously control the AOM, camera, and translation stage. The following list provides an example of specific processing steps to creating 3D silver patterns in PVP.

1. Adjust compressor or pulse shaper to obtain 50-fs pulses after microscope objective.
2. Adjust neutral density filters to obtain 3-nJ pulses after the objective.
3. Ensure laser spot size is larger than back aperture of microscope objective.
4. Set AOM to produce 10-μs exposure windows, which will irradiate the sample with 110 pulses per voxel. A broad range of laser parameters can be used for silver growth (see Figure 11).
5. Block laser beam before it reaches the microscope and place sample onto translation stage. The beam path of the femtosecond laser pulses should pass through the imaging microscope objective and into the sample. Turn on microscope illumination source to observe the sample in-situ using camera.
6. Translate *z*-axis of stage to find interface between glass substrate and polymer film. Then, refocus microscope to the desired depth inside polymer for patterning bottom-most layer. *Z*-translation during patterning must be in the direction away from the glass-polymer interface to avoid scattering with fabricated structures.
7. Unblock laser-beam and set motion-controller software to translate sample in *x*-, *y*- and *z*-directions with speed of 100 μm/s. Irradiate single voxels with previously set exposure

windows (10 μs) and separate neighboring voxels by at least several micrometers for clear in-situ imaging. Laser exposed areas will contain silver structures.

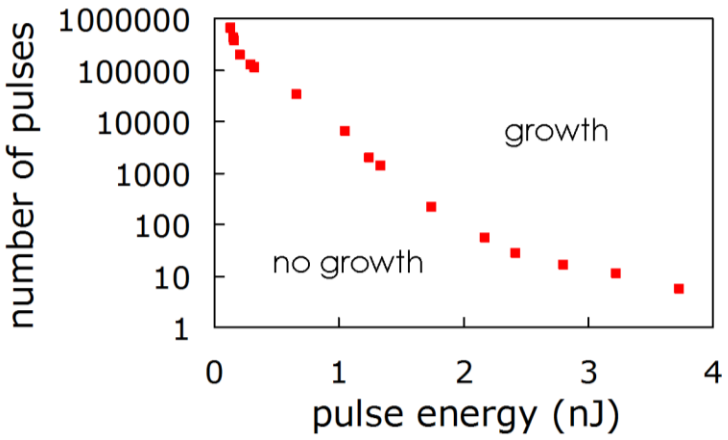

Figure 11: Number of laser pulses required for silver growth as a function of pulse energy. The data points show the minimum number of pulses required to observe silver growth with an in-situ optical microscope at each energy parameter. Exposure parameters to the right of the data points lead to silver growth, and parameters to the left do not yield silver structures that are observable using the in-situ microscope.

The actual patterning of the sample only occurs in step 7; once the samples are exposed to the laser irradiation, the writing process is complete. This is referred to as a single step writing process. For techniques such as TPP, additional steps are necessary after laser exposure to develop a pattern.

A key difference between laser processing of transparent structures, such as in TPP and glass micromachining, and metals, is the direction of travel over the sample depth (*z*-axis). In the former, motion can be in both positive and negative directions over the *z*-axis. However, for metals, the direction of travel must be oriented such that the sample moves further away from the objective when translating between layers. This is necessary to ensure that fabricated structures do not scatter laser light when patterning newer elements at different depths.

2.5.4 Sample processing for electron microscopy

Characterizing a sample using transmission electron microscopy (TEM) or SEM requires the removal of the polymer layer: the methods cannot image through the dielectric to obtain 3D images of embedded silver, and may also drive further silver growth. Thus, electron microscopy characterization occurs in 2D.

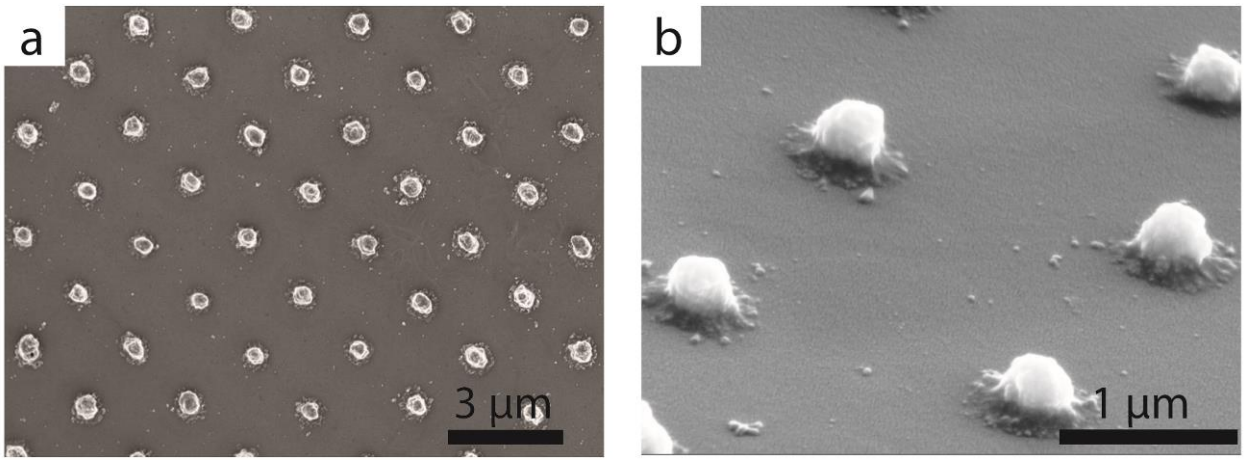

Figure 12: High-resolution SEM images of a patterned sample of silver dots on a glass substrate. (a) Image of a 2D array of silver dots. (b) Close up view of silver dots at a 61° tilt angle.

For TEM, we first wash samples in either ethanol or deionized water to dissolve the polymer. The grown metal structures are then transferred to a carbon coated TEM grid with a razor blade and ethanol. For SEM imaging, metal structures are grown at the polymer-substrate interface. The polymer is dissolved with ethanol, leaving behind structures strongly adhered to the substrate. The SEM images in Figure 12 show silver dots fabricated at the substrate interface. If the dots were fabricated further into the bulk of the polymer, they would have been washed away due to poor adhesion.

Conductive coatings are necessary to minimize charging effects during high resolution SEM imaging. We have used two different options, both of which are effective. In the first, the patterned substrate is coated with a thin layer of gold or carbon after the washing step. In the second, we use glass substrates that are pre-coated with a thin layer of indium tin oxide.

2.6 Summary

When used for fabrication, femtosecond lasers provide the flexibility of creating 3D patterns in a variety of material systems. They are often used for rapid prototyping since they do not require the creation of lithographic masks. Metal patterning with ultrafast lasers is relatively underdeveloped, but offers the promise of creating new types of devices. Finding the right experimental conditions (combination of chemical reagents, as well as laser parameters), is crucial for the fabrication of metal structures.

The methods we describe require commonly available chemicals for sample preparation, and laser processing methods that are similar to alternate femtosecond laser writing techniques. With these general methods, we create both 2D and 3D metal patterns, as described in the following chapters (with any processing deviations being specified). 2D samples consist of metal structures adhered to a glass substrate. 3D samples consist of silver embedded inside a polymer; creating a composite material where the positioning of each material phase is controlled through laser irradiation. These samples could be considered as structured nano-composites.

Chapter 3

Femtosecond laser fabrication of silver in 2D

In this chapter, we describe our work on multiphoton laser direct writing of silver structures in two dimensions. This work was inspired by the research of Baldacchini reported in 2005 [11]. We use the same materials and steps for our sample preparation, which requires a metal precursor, a polymer and two solvents. We reproduce similar results to Baldacchini et al. and create silver nanoparticle aggregates. In addition to these results, we also grow large silver particles with polygonal shapes: hexagonal shaped monocrystalline silver, as well as crystallites with several hexagonal crystals attached to each other.

3.1 Line fabrication

We prepare samples by first dissolving 0.25 grams of PVP in 10 mL of ethanol at room temperature. We then mix in a separately prepared solution of 0.4 grams of silver nitrate in 2 mL of deionized water. The mixed solution is stirred in the dark for 25 minutes at room temperature, at the end of which the solution assumes a translucent orange color. A glass substrate, treated

through plasma cleaning and silanization with (3-acryloxypropyl)trimethoxysilane, is then covered with the solution. The sample undergoes spin coating at 1000 rpm for 30 seconds to produce a film with a thickness of approximately 1 μm. Finally, the sample is baked at 110 °C for 30 minutes and cooled. The preparation is conducted in an area devoid of UV light to minimize degradation. The samples have short shelf-lives and degrade quickly.

To pattern lines, we irradiate samples continuously as they are translated; varying the translation speed changes the number of pulses irradiating the sample per unit distance. After laser writing, we bathe the samples in ethanol to remove the polymer layer while leaving fabricated silver attached to the substrate. Baldacchini et al. used an excitation source centered at 780 nm, with 250 fs pulses and 76 MHz repetition rate for their silver line writing experiments [11]. They showed 5 micron scale linewidths, where the lines are can be characterized as loose nanoparticle aggregates (as shown in Figure 8), with a translation speed of 80 μm/s, a 0.5-NA objective and a pulse energy of 0.46 nJ (35 mW average power) at the sample. We obtain similarly structured lines using a green laser (525-nm center wavelength) with 270-fs pulses and 11-MHz repetition rate, and a 0.65-NA objective. Figure 13a shows silver lines we fabricated with 1.4-nJ pulse energy and 100-μm/s translation speed; a close inspection reveals the lines are composed of silver nanoparticle aggregates. By increasing the translation speed, we obtain silver lines with smaller widths. Figure 13b shows silver linewidth as a function of scanning speed. The feature size decreases almost linearly between 100 and 450 μm/s. The pulse density (number of pulses as a function of linear distance) during exposure ranges from 110,000 pulses per micron to 24,000 pulses per micron.

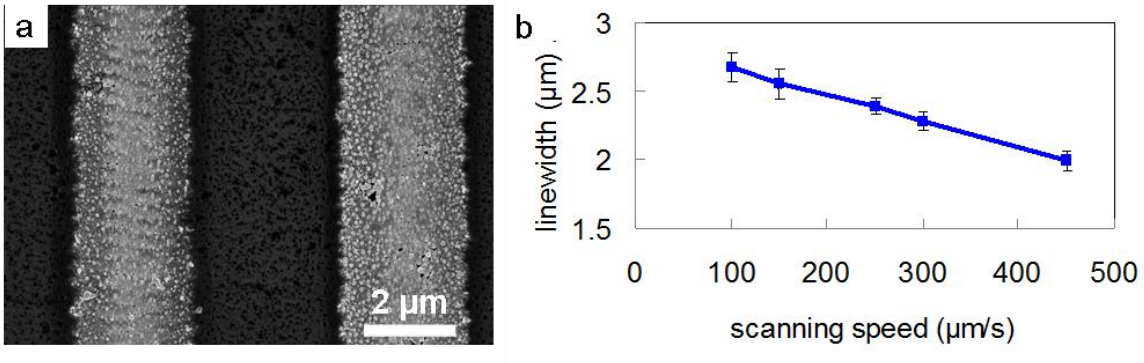

Figure 13: (a) Silver lines fabricated with a 100 µm/s translation speed. (b) Average silver linewidth as a function of translation speed. The error bars show the standard deviation obtained from 10 to 20 measurements at each point.

We analyze the elemental content of fabricated structures through energy dispersive x-ray spectroscopy (EDS), shown in Figure 14. The spectrum from the substrate next to the line (Figure 14b) does not have an Ag signal, as expected, since it is glass. The spectrum from a line (Figure 14a) shows a signal that is dominated by Ag. However, there is also a carbon signal in the EDS measurements (not shown). This indicates that the lines are composed of both silver and polymer. The presence of polymer in femtosecond laser grown silver is clearly seen in Figure 15 where portions of the silver from patterned lines have been removed. The dark structures are polymer, whereas the light structures are silver. PVP is soluble in ethanol, and thus should not be present on the sample after the washing process. However, the presence of polymer on the sample can be explained through crosslinking. Polyvinylpolypyrrolidone (PVPP) is a highly crosslinked form of PVP and can be generated from PVP through the action of heat [25-28]. Whereas PVP is highly soluble in water and ethanol, PVPP is not [25-28]. We hypothesize that the fabrication process, in addition to growing silver, also induces the local crosslinking of PVP, creating PVPP that remains on the sample after PVP is removed.

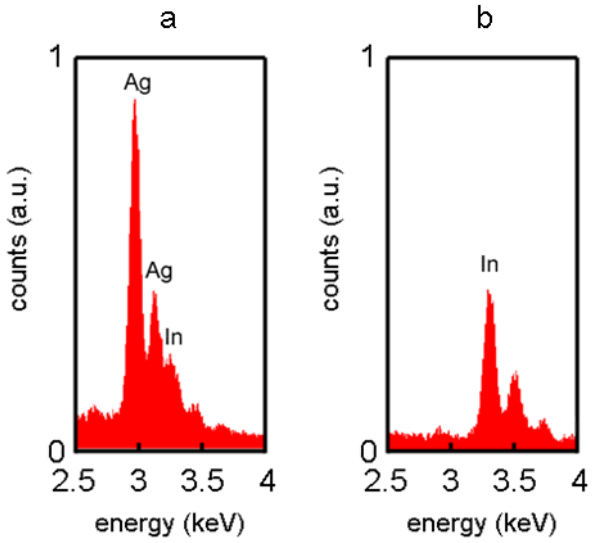

Figure 14: EDS spectra of (a) a patterned line, and (b) the surrounding area. The In signal is from an ITO coating on the substrate. Data courtesy of Michael Moebius.

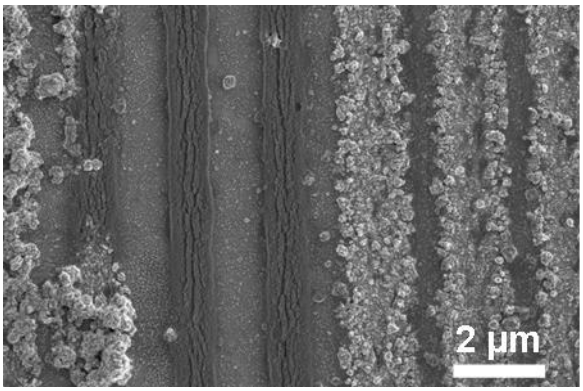

Figure 15: Array of silver lines. Part of the silver has been removed, exposing a polymer underlayer. Image courtesy of Michael Moebius and SeungYeon Kang.

We also obtain silver growth using different chemical reagents. For example, we grow silver using a combination of silver nitrate and ethylene glycol. The lines we obtain resemble filaments rather than nanoparticle aggregates (using an 800 nm laser source with 50-fs pulses). Figure 16a shows such a feature with a linewidth around 200 nm. Further analysis of these lines reveals that there is a change in the elemental composition of the structures: EDS measurements show an increased carbon content relative to silver. We also grow silver using a reagent mixture

of PVP, silver nitrate, and water (without ethanol), which is described further in Chapter 2 and Chapter 4. Unlike sample preparation using ethanol, these polymer films are stable for much longer periods of time. Using this chemical formulation, we observe high resolution linewidths with strong silver content. Figure 16b shows 600-nm silver lines grown in a zigzag pattern. It is also possible to grow metals other than silver using femtosecond laser writing. For example, we have fabricated gold structures using a mixture of chloroauric acid ($HAuCl_4$), deionized water and polyvinyl alcohol (PVA).

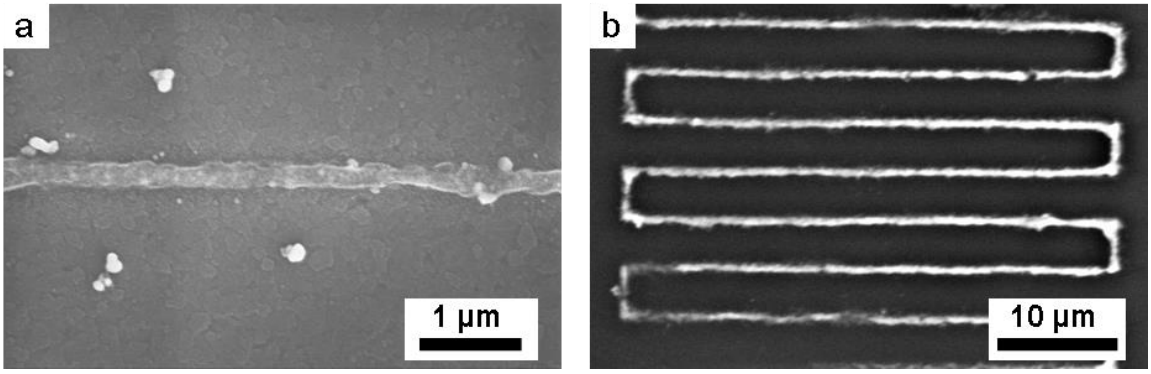

Figure 16: The resin chemistry can be modified for the silver growth process. (a) Thin 200 nm line fabricated with femtosecond laser irradiation of a sample with ethylene glycol. (b) (Image courtesy of SeungYeon Kang.) Thin 600 nm silver lines grown in a solution of PVP, deionized water, and $AgNO_3$.

Using the same chemical formulation as Baldacchini et al. [11], we show similar line structure growth using a 525-nm laser. These structures consist of silver nanoparticle aggregates. These lines are rough in appearance, and sub-optimal for applications that require smooth silver structures, such as plasmonic waveguides. However, the structures may have applications in areas such as SERS, where metal roughness can be an asset [29]. Sample preparation can have strong effects on silver growth, making it possible to tune the process. By applying modifications to the chemical composition of samples, we are able to grow lines with smaller widths and different

morphologies. Further research is necessary to characterize the quality of silver, and broaden the range of features that can be achieved.

3.2 High quality crystal growth

This section covers research reported in: K. Vora,* S. Kang,* M. Moebius, and E. Mazur (*co-first authors), "Femtosecond light-induced growth of hexagonal silver nanocrystals," *Manuscript in preparation*, 2014.

In the previous section, similarly to Baldacchini et al. [11], we showed how a mixture of PVP, $AgNO_3$, deionized water and ethanol can produce silver lines composed of an assemblage of silver nanoparticles. In this section, we show how the same chemical formulation can be used to grow single crystal silver.

Bottom-up growth methods and top-down patterning techniques are both used to fabricate metal nanostructures [30-40], each with a distinct advantage: one creates crystalline structures, and the other offers precise positioning. Here, we present a technique that localizes the growth of metal crystals to a laser focal volume, combining advantages from both approaches. We report the fabrication of silver nanoprisms—hexagonal silver nanocrystals—through irradiation with focused femtosecond laser pulses. The growth of these nanoprisms is due to a nonlinear optical interaction between femtosecond laser pulses and a polyvinylpyrrolidone film doped with silver nitrate. The hexagonal nanoprisms have bases hundreds of nanometers in size and the crystal growth occurs over exposure times of less than 1 ms (over 6 orders of magnitude faster than traditional chemical techniques [36-39, 41]). Electron backscatter diffraction analysis shows that the hexagonal nanoprisms are monocrystalline. The fabrication method combines advantages from both wet

chemistry and femtosecond laser direct-writing to grow silver crystals in targeted locations. The results presented in this section offer an approach to growing silver crystals on a substrate, which can be used for plasmonic devices.

Compared to bulk silver, nanocrystals have unique characteristics [42-44] that make them useful for various applications, such as catalysis, biomedical sensing and electronics [45-51]. A variety of techniques have been developed to fabricate silver nanoparticles [30-39]. Among these techniques, wet chemistry is popular for growing high-quality silver crystals in a multitude of shapes, including pyramids, bipyramids, cubes, triangular prisms, hexagonal prisms, and nanowires [36-39]. Implemented by itself, wet chemistry lacks patternability. Conversely, femtosecond laser direct-writing methods are used to grow silver in engineered patterns in two and three dimensions [6, 8-11, 41, 52, 53]. The resulting structures are composed of aggregates of much smaller silver nanoparticles, often with void or polymer inclusions [53]. We present a method that leads to rapid growth of monocrystalline hexagonal silver nanoprisms through irradiation with focused femtosecond laser pulses. The technique allows us to localize chemical reactions that lead to crystal growth to specific positions on a substrate. The silver structure yield, dominated by hexagonal prisms, also shows twinned crystals.

To fabricate the nanocrystals, we use a mixture of polyvinylpyrrolidone (PVP), silver nitrate ($AgNO_3$), ethanol, and water. We first prepare a solution by dissolving 0.25 g of PVP in 10 mL ethanol at room temperature. In a separate vial, we dissolve 0.4 g of $AgNO_3$ in 2 mL of deionized water. Once both mixtures are dissolved, we add them together and stir for 25 min. at room temperature. The solution is spin-coated onto a glass slide (1000 rpm for 30 s). Lastly, the sample is baked in an oven for 25 min. at 110 °C. These steps are done in a room filtered of ultraviolet

light to minimize unwanted silver nanoparticle formation. The resulting sample consists of a micron-thick polymer film doped with silver ions on a glass substrate.

We use a Ti:sapphire laser centered at 795 nm with an 11-MHz repetition rate and 300-fs pulse duration for the irradiation process. A description of the laser fabrication setup can be found in Chapter 2. The laser exposure is limited to individual voxels inside the PVP film, at the glass-polymer interface. The laser focal diameter is approximately 1 μm (full-width half-max).

In-situ optical imaging shows that patterned samples have silver growth at close to 100% of irradiation spots. However, after irradiation, the polymer film must be dissolved with water or ethanol for sample analysis, leaving behind only those silver nanostructures strongly adhered to the glass substrate. Scanning electron microscopy (SEM) image analysis reveals the yield of silver adhered to irradiation sites after polymer removal is approximately 5%. This low yield is due to insufficient adhesion between crystals and the substrate. Further work is necessary to improve adhesion; we expect to achieve higher yields with additional pre-treatment steps that increase adhesion. Within the adhered structures, 45% are crystals with hexagonal shaped bases (6 facets with 120º internal angles), 21% are partially ablated or cracked hexagonal crystals, 15% are crystals with hexagonal-like bases (which have small deformations, or greater than 6 facets, with additional facets positioned with 120º or -120º internal angles), and 12% are twinned crystals.

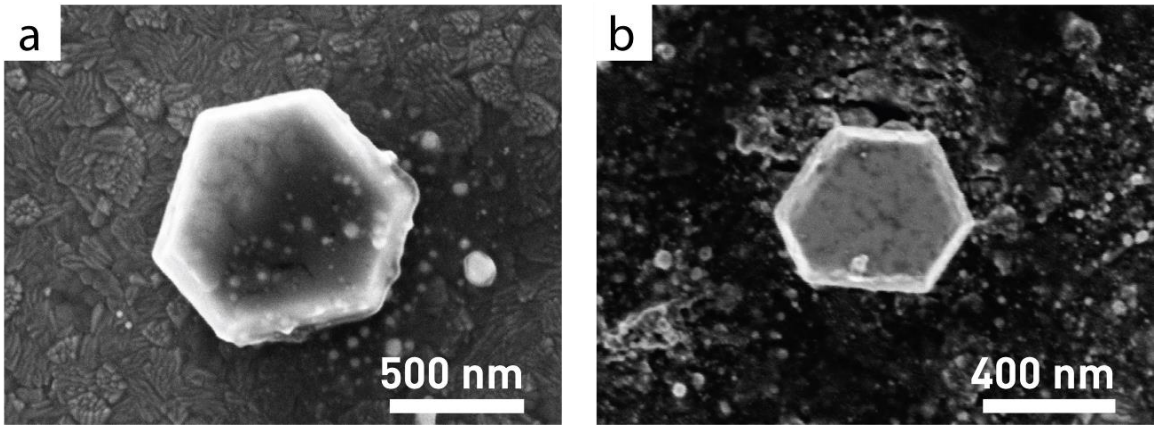

Figure 17: SEM images of (a) 900-nm and (b) 500-nm crystals grown by irradiation with a 795-nm femtosecond laser with a total exposure time of (a) 100 μs and 4.1 nJ per pulse and (b) 800 μs and 1.5 nJ per pulse.

Figure 17a shows an SEM image of a 900-nm crystal grown with a total exposure time of 100 μs and 4.1 nJ per pulse; Figure 17b shows an SEM image of a 500-nm crystal grown with an exposure of 800 μs and 1.5 nJ per pulse. The fabricated silver crystals vary in size between 400 nm and 1 μm. Figure 18a shows two hexagonal crystals grown next to each other with different sized bases (with a high magnification image in Figure 18b). Figure 18c shows six crystals grown in proximity to each other, each with varying deformations (two of the crystals are shown with higher magnification in Figure 18d).

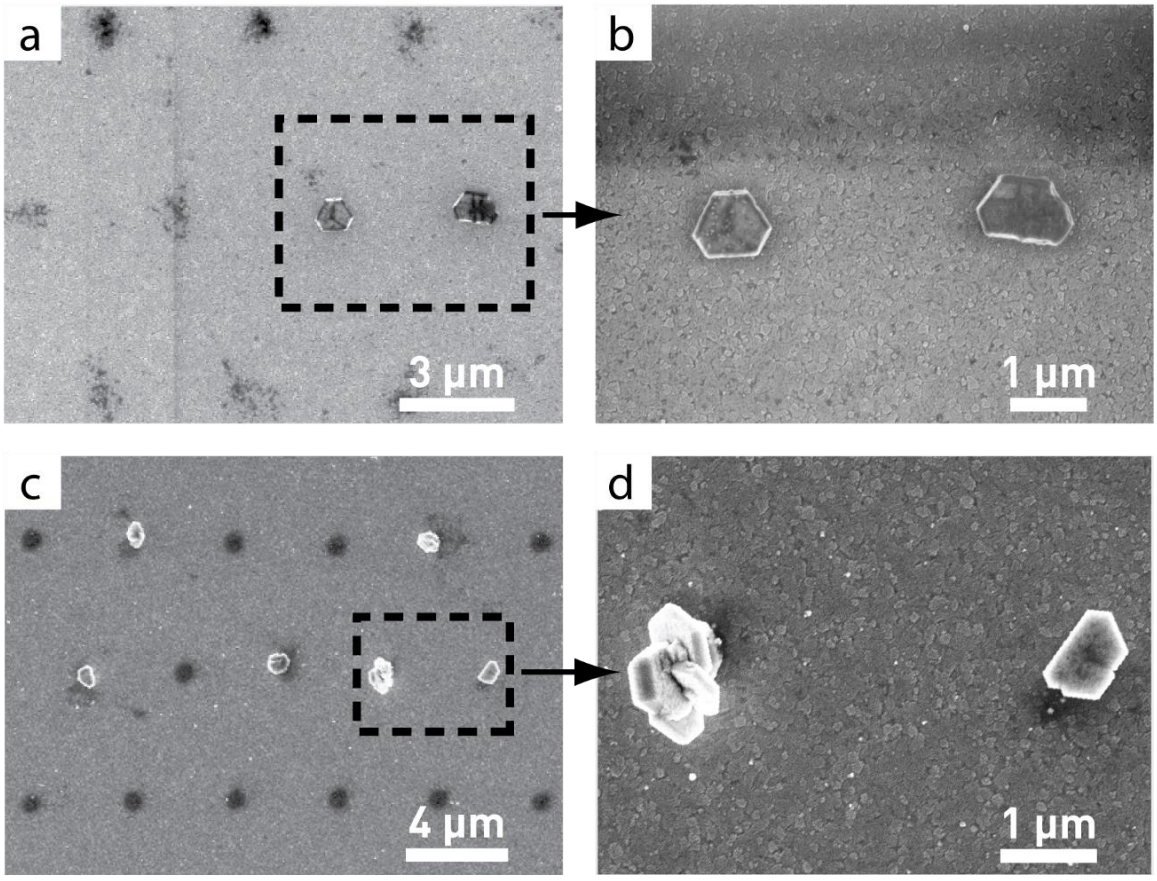

Figure 18: Sample preparation for SEM imaging removes all structures not strongly adhered to the substrate. These SEM images show silver crystals that remain attached to the glass. (a) Image showing two silver crystals grown in laser irradiation spots. (b) A close-up view reveals both crystals are hexagonally shaped and have different sized widths. (c) Image showing six crystals grown in proximity to each other. (d) A close-up view reveals two silver structures that are not single crystal hexagonal prisms. The left structure is a twinned crystal. The right structure is a crystal where the internal angles are ±120º.

Several factors affect crystal growth, including pulse energy and exposure time, laser focus position, laser stability, as well as local variations in the polymer or substrate. These conditions affect both shape and size of silver structures grown through femtosecond laser irradiation. Despite variations, the yield from the fabrication process is strongly dominated by prisms with hexagonal shapes.

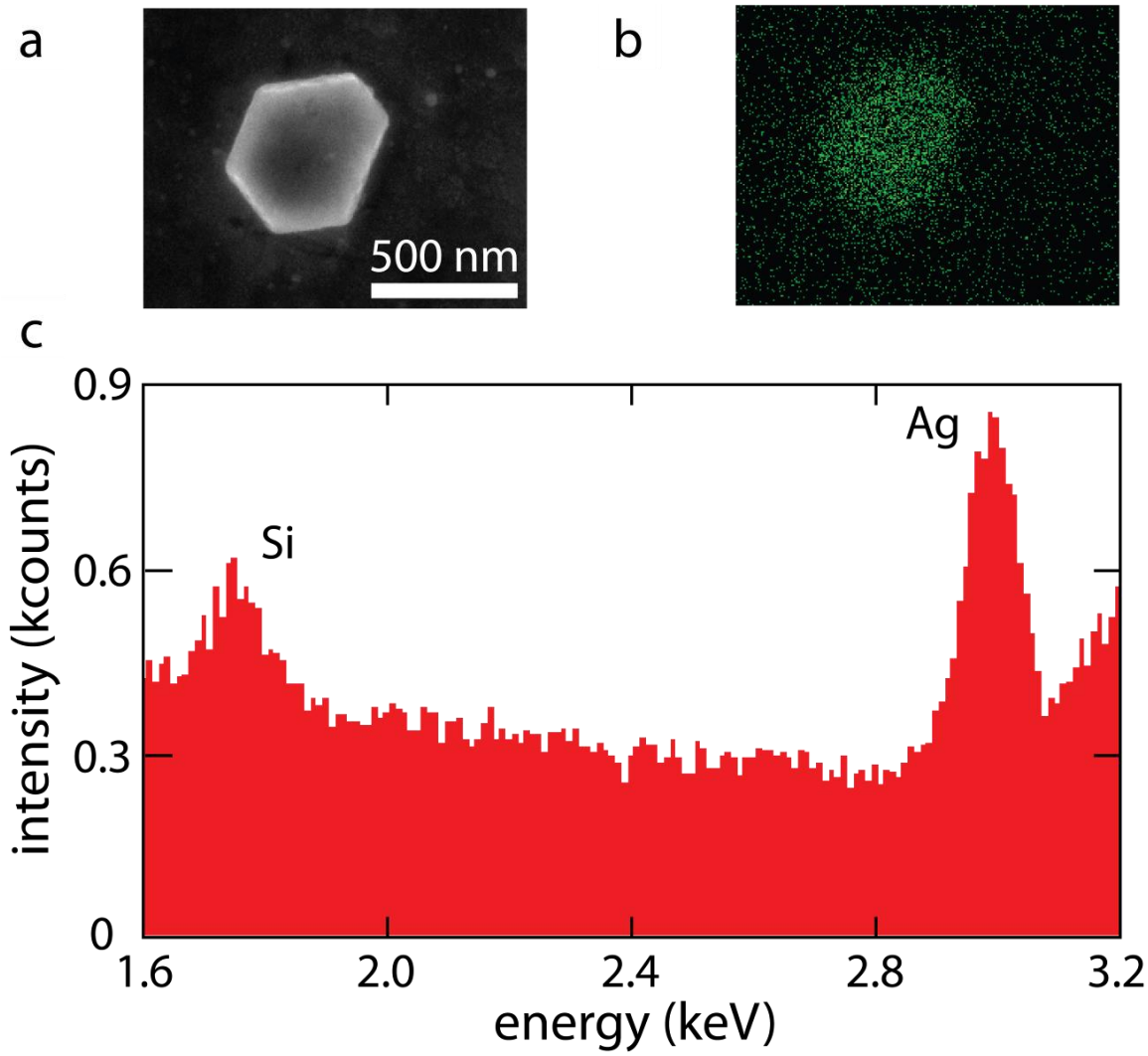

Figure 19: (a) SEM image of a 500-nm crystal, (b) corresponding silver EDS map, and (c) EDS spectrum. The map shows a silver signal concentrated at the location of the nanocrystal, demonstrating high silver content. The silicon signal originates from the sample substrate.

Figure 19 shows an SEM image of a hexagonal crystal grown at an exposure of 800 μs and its corresponding energy dispersion x-ray spectroscopy (EDS) maps. The EDS elemental maps show that the nanocrystal is composed of silver. We further characterized the crystals through electron backscatter diffraction (EBSD) measurements, which provide information on the orientation and crystal structure of a material. Figure 20 shows EBSD measurements indicating a single-crystal

FCC lattice structure in the hexagonal crystal (Figure 20a), consistent with monocrystalline silver. Figure 20b shows uniform grain orientation and phase distribution with no grain boundary and Figure 20d shows the crystallographic orientation of the fabricated silver nanocrystal. The (100) pole plot in Figure 20c represents a stereographic projection of the crystallographic directions present in the grains that make up the material. All individual point orientation measurements from the sample are shown together as three closely-packed clusters of points on the pole figure representing the (100), (010) and (001) planes of the sample. These results indicate that probed portions of the silver structure are single-crystal; the hexagonal silver structures are monocrystalline, unlike silver grown through previously reported femtosecond laser techniques [6, 8-11, 41, 52, 53]. From the EDS and EBSD analyses we conclude that under appropriate conditions, the femtosecond-laser direct metal writing leads to single-crystal nanoparticle growth.

In our 3D fabrication work (see Section 4.1), we used water rather than a mixture of water and ethanol to dissolve the solutes [53]. Even though the PVP-to-$AgNO_3$ ratio is the same in both experiments, we do not observe any monocrystalline silver structures in the absence of ethanol [53]. We therefore believe that ethanol promotes crystal growth.

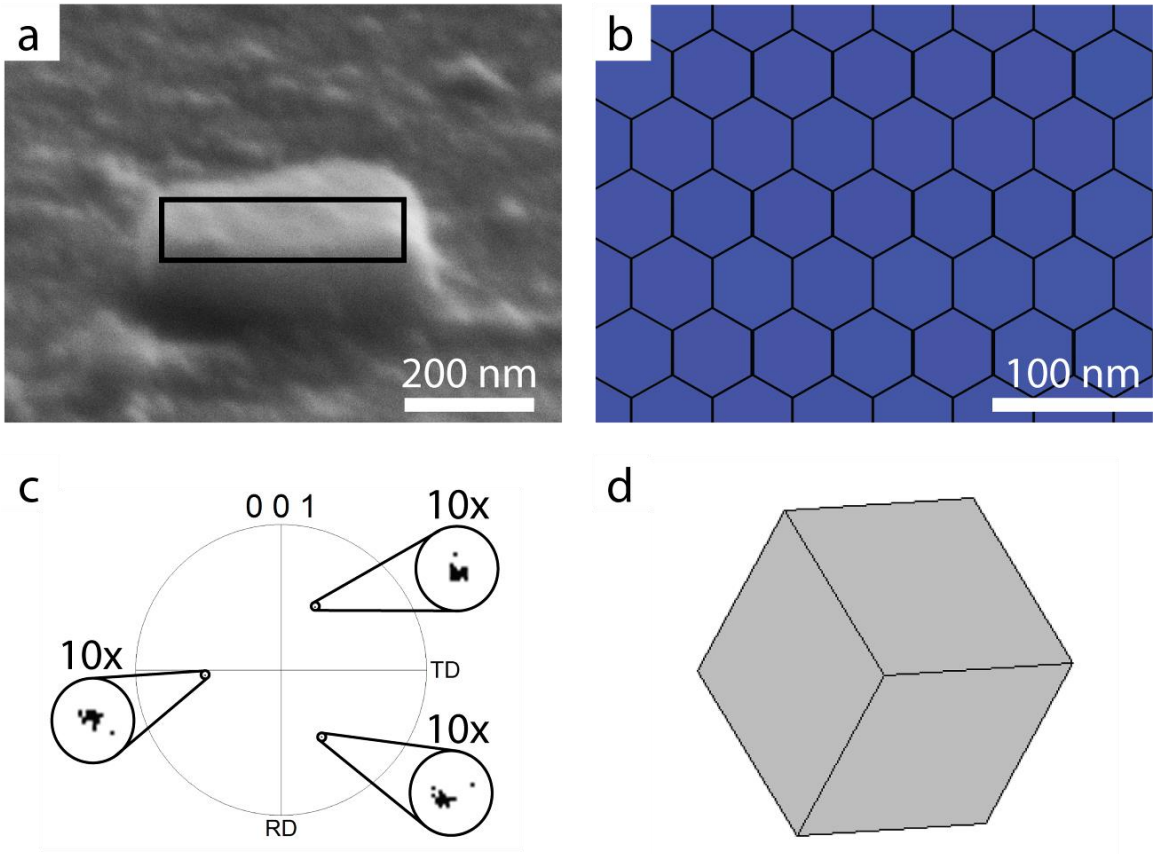

Figure 20: SEM image of a silver 400-nm nanocrystal and corresponding EBSD data showing single crystal structure. (a) SEM image taken from a 70° angle; outline shows the area mapped with EBSD. (b) The honeycomb contour in the EBSD map outlines the individually probed pixels; the color uniformity is indicative of single crystal orientation. (c) The (001) pole figure further highlights single crystal orientation; the insets show a 10x close-up. RD refers to sample rolling direction and TD refers to transverse direction. The silver crystal orientation is shown in (d), where the substrate is in the plane of the page.

During growth using wet chemistry, the shape and size of silver crystals can be tuned by varying the chemical composition [36-38]. The strong affinity of N and O atoms in the amide groups of PVP to surfaces of transition-metal clusters restrains the growth of these clusters. Because the PVP interacts preferentially with {100} planes in silver crystals, it leads to faster growth in specific crystal directions [37, 38]. However, the size and shape of the nanocrystals we produce with the laser technique are rarely observed using wet chemistry even when the same

chemical reagent mixture is used [36-39, 51]. This suggests that the non-equilibrium dynamics arising from the femtosecond excitation play a role in the growth of nanoprisms.

Traditional wet chemistry is relatively slow; at a typical refluxing temperature of 120 to 160 °C it takes between 0.5 and 30 hours to grow silver crystals between 80 nm and 280 nm in size [36-39]. We use exposure times that are over 6 orders of magnitude shorter, and yet obtain much larger crystals. Such ultrafast growth rate has not been previously reported. As described in Section 3.2.2, irradiation with femtosecond laser pulses leads to plasmon resonances and high temperatures in the irradiation focal volume during fabrication; we believe these factors contribute to the ultrafast growth process.

In conclusion, the method we describe localizes chemical reactions that lead to silver crystal growth at specific positions on a substrate. We grow silver structures with a yield dominated by hexagonal prisms. The use of femtosecond laser irradiation dramatically increases the growth speed and size of nanocrystals compared to traditional techniques; we obtain hexagonal shapes that are hundreds of nanometers in size with sub-millisecond laser exposure. By fine-tuning the laser parameters, chemical reagents, and silver adhesion, the technique outlined in this section may be modified to finely control the shape and size of silver crystals, and increase yield. This could present a significant advancement for the fabricating of plasmonics devices.

3.2.1 Methods

Sample fabrication

The excitation source for fabricating silver structures is a Ti:sapphire laser system producing 50-fs pulses with a center wavelength of 795 nm and a repetition rate of 11 MHz. A set of ND filters reduces the intensity of the pulses to a range between 1 and 5 nJ. The fabrication takes place under

an upright microscope. A 0.8-NA microscope objective focuses laser pulses inside the sample and provides in-situ imaging. A high-precision and long-travel three-axis translation stage scans the sample in the *x*-, *y*- and *z*-directions, while an acousto-optic modulator shutters the laser beam to control the exposure.

Imaging and analysis

To image and analyze fabricated structures, it is necessary to wash away the metal ion containing polymer matrix by dipping the sample in ethanol for 30 min. after femtosecond patterning. This leaves behind only structures fabricated at (and attached to) the substrate. The glass substrate is coated with a thin 20-nm layer of indium tin oxide— and also oxygen plasma treated and silanized with (3-acryloxypropyl) trimethoxysilane—before sample preparation to eliminate charging effects during imaging.

3.2.2 Simulations on temperature increase during fabrication

Fabrication parameters must be chosen carefully to avoid damage to the substrate. In the absence of a doped polymer film, direct damage of the ITO substrate required fluence greater than 54 kJ/m^2. However, during exposure in the presence of a silver doped PVP film, 3 kJ/m^2 was sufficient to damage the substrate. We expect that a combination of effects is responsible for the drop in damage threshold. Simulations indicate that the laser irradiation produces surface plasmon resonances in growing silver structures, increasing field intensity near the substrate. Additionally, growing silver particles increase the absorption of incident pulse energy, leading to higher temperatures in the laser focal volume. Both effects combine to reduce the damage threshold of the substrate.

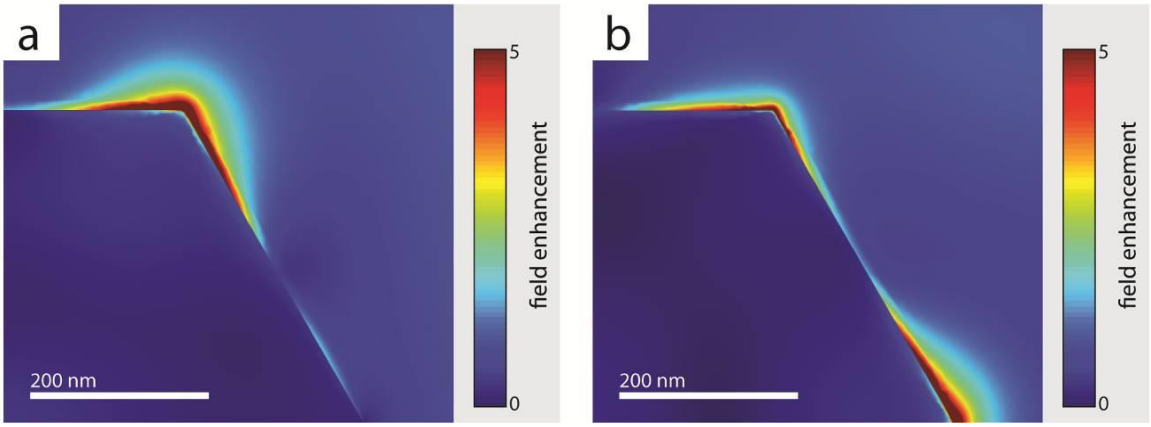

Figure 21: Plasmon enhancement map of the electric field magnitude around symmetric hexagonal silver crystals with a side length of 400 nm from COMSOL. Incident field is polarized (a) vertically and (b) horizontally and only one quarter of the crystal is simulated, taking advantage of the structure symmetry. The scale bar was set to saturate at 5 for visualization.

The plasma frequency of bulk silver lies in the ultraviolet; however, shape, size, and proximity of nanometer-sized particles can shift and broaden plasmon resonances [54]. A high refractive index cladding material will also red-shift plasmon resonances [54]. As a result, plasmon resonances in silver can be observed into the near infrared. We conducted simulations using finite element analysis (COMSOL Multiphysics) to estimate the magnitude and location of plasmon resonances in hexagonal crystals. As expected, resonances occur near vertices aligned with the incident light polarization (see Figure 21). Local electric field enhancements range from 3-18 (for wavelengths between 600-950 nm) and correspond well to the observed reduction in damage threshold. Figure 22 shows parameter sweeps of the maximum local field enhancement as a function of crystal size and incident light wavelength.

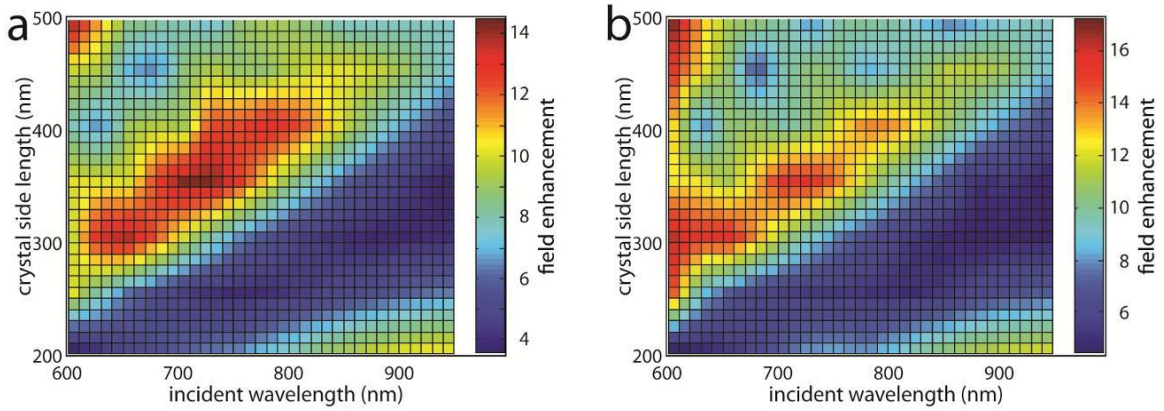

Figure 22: Parameter sweep of electric field enhancement as a function of crystal side length and incident light wavelength with field polarized (a) vertically and (b) horizontally.

COMSOL heat diffusion simulations indicate that temperature in the focal volume increases during fabrication, which also contributes to the growth process. We estimate a temperature increase to 400 K inside the laser focal volume with a dose of 3-nJ per pulse over 100 μs (at an 11 MHz repetition rate). We assume crystal growth begins with the formation of individual nanoparticles [11, 53] which leads to higher light absorption through multiple reflections and field enhancement.

3.3 Future work

In this chapter, we describe our work on multiphoton laser direct writing of silver structures in two dimensions. Using a mixture of PVP, $AgNO_3$, deionized water, and ethanol, we reproduce the structures obtained by Baldacchini et al. [11], and we also grow single crystal hexagonal silver prisms. We show that modifications in the sample chemistry and laser parameters can affect silver growth.

These results lay a path for future developments leading to improved direct laser metal writing: finer control over resolution, and crystallinity. Such work could lead to significant

developments for plasmonics device applications. Further work needs to be conducted to characterize the electrical properties of silver for potential use in microelectronic devices.

In addition, more fundamental work is needed to fully understand and characterize the metal growth process. There is very little literature that studies the growth process with femtosecond laser irradiation. Pump-probe spectroscopy experiments would greatly elucidate the silver growth mechanisms on short timescales.

Chapter 4

Femtosecond laser fabrication of silver in 3D

The standard nanofabrication toolkit includes techniques primarily aimed at creating 2D patterns in dielectric media. Creating metal patterns on a submicron scale requires a combination of nanofabrication tools and several material processing steps. For example, steps to create planar metal structures using ultraviolet photolithography and electron-beam lithography can include sample exposure, sample development, metal deposition, and metal liftoff. To create 3D metal structures, the sequence is repeated multiple times. The complexity and difficulty of stacking and aligning multiple layers limits practical implementations of 3D metal structuring using standard nanofabrication tools. Femtosecond laser direct writing has emerged as a preeminent technique for 3D nanofabrication [2, 3]. Femtosecond lasers are frequently used to create 3D patterns in polymers and glasses [13, 55-58]. The laser wavelength is chosen such that photons are not linearly absorbed in the target medium. When the laser pulse duration is compressed to the femtosecond time scale and the radiation is tightly focused inside the target, the extremely high intensity induces nonlinear absorption. Multiple photons are absorbed simultaneously to cause electronic transitions

that lead to material modification within the focused region. Using this approach, one can form structures in the bulk of a material rather than on its surface. Figure 23 shows a simple 3D pattern we created that would be very difficult to fabricate using standard tools: an array of silver dots floating on top of another array. To create this type of pattern, we need to embed one material inside another.

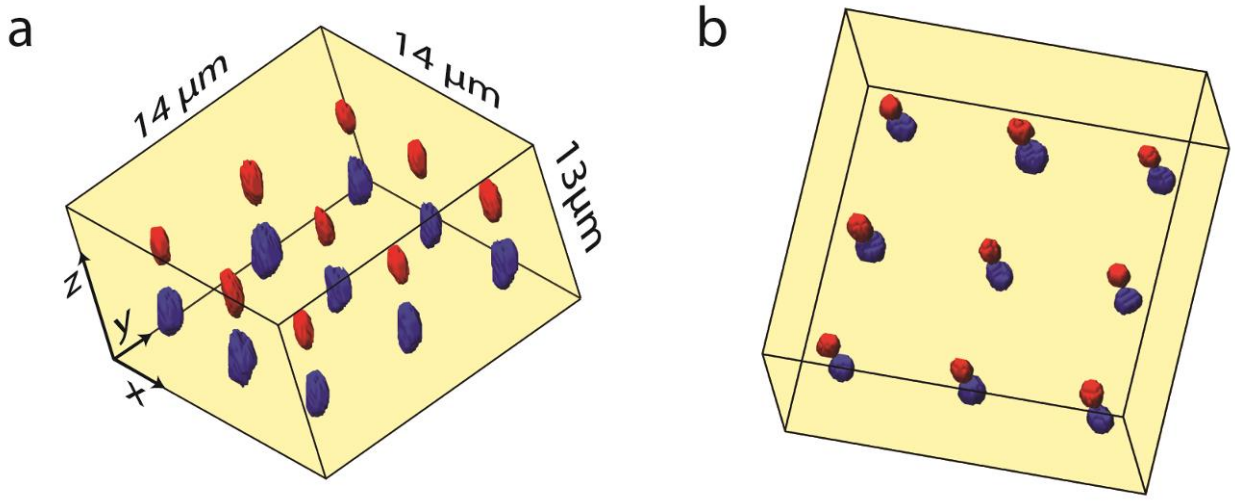

Figure 23: 3D rendered images of a silver dot array inside a matrix using a PVP based chemistry. Using an exposure of 110 pulses per voxel and 3 nJ per pulse, with the stage translating at 100 µm/s, the resulting silver structures are readily visible through the in-situ optical microscope. (a) 2-layer array of 18 silver dots created inside a matrix. For clarity, the two layers of dots are represented in different colors. The rendering was created by stacking sequential optical microscopy images. (b) A different view of the 3D array. Adapted from Reference [52].

Most work on 3D direct metal writing has focused on creating self-supported metal structures [6, 9, 10]. In this chapter, we focus on direct laser writing of metal to fabricate silver nanostructures that remain embedded inside a polymer matrix (such as in Figure 23). The method enables the fabrication of patterns not feasible using other techniques, such as 3D arrays of disconnected silver ellipsoids [53]. Disconnected 3D metal patterns are useful for metamaterials where unit cells are not in contact with each other [1], such as coupled metal dot [59, 60] or coupled

metal rod [10, 61] resonators. Potential applications include negative index metamaterials, invisibility cloaks, and perfect lenses.

We use two different combinations of polymer and silver salt: PVP with $AgNO_3$, and gelatin with $AgNO_3$. We first present a paper on 3D fabrication in a PVP based sample. We then present our work on 3D fabrication in a gelatin based sample.

4.1 3D fabrication in PVP

The following paper appears in *Applied Physics Letters*, 100, 063120 (2012).

Fabrication of disconnected three-dimensional silver nanostructures in a polymer matrix

Kevin Vora,[1] SeungYeon Kang,[1] Shobha Shukla,[1] Eric Mazur[1,2]

[1]School of Engineering and Applied Sciences and [2]Department of Physics, Harvard University, 9 Oxford Street, Cambridge, Massachusetts 02138

Abstract: We present a simple, one-step technique for direct-writing of a structured nanocomposite material with disconnected silver nanostructures in a polymer matrix. A nonlinear optical interaction between femtosecond laser pulses and a composite material creates silver structures that are embedded inside a polymer with submicrometer resolution (300 nm). We create complex patterns of silver nanostructures in three dimensions. The key to the process is the chemical composition of the sample that provides both a support matrix and controlled growth. The technique presented in this Letter may offer a cost-effective approach for the fabrication of bulk optical devices with engineered dispersion.

Chapter 4 - Femtosecond laser fabrication of silver in 3D

The burgeoning field of metamaterials has seen many ground-breaking theoretical advances in recent years, but experimental advances for infrared and optical devices have been hampered by the difficulty in patterning metals in three dimensions (3D) at the submicrometer scale [40]. Multiphoton absorption lithography, or femtosecond laser direct-writing, has emerged as a pre-eminent technique that addresses true 3D fabrication at the micro- and nano-scales [2, 3]. Structures much smaller than the diffraction limited laser spot size are now readily produced in transparent media such as glasses [13] and polymers [55-58]. What makes sub-wavelength structuring possible is the nonlinear optical interaction between the femtosecond laser pulses and material of interest. The excitation wavelength of the fabrication laser is chosen such that photons are not linearly absorbed in the target medium. Yet, when the laser emission is compressed to ultrashort pulses and tightly focused with a lens, multiple photons can converge in time and space to collectively bridge the target's energy gap and create an electronic transition. This multiphoton absorption can lead to material change that is confined to femtoliter or even attoliter volumes within the tightly focused region.

Femtosecond direct laser writing is mostly limited to the patterning of dielectric media, such as glasses and polymers. Only limited advances have been made in the direct-writing of metals, which are critical for applications of metamaterials such as negative refraction [40, 62-64]. One method for creating metal structures in 3D is to supplement the direct laser writing of polymer patterns with a metal deposition step, either by coating 3D polymer structures [5, 65-67] or by filling contiguous volumetric voids [4]. However, this approach precludes the creation of arbitrary 3D metal nanostructures that are disconnected, such as a volumetric array of metal dots. Three-dimensional arrays composed of fully disconnected metal features would enable the creation of

bulk optical and infrared metamaterials comprising coupled metal dot [59, 60] or coupled metal rod [61, 68] resonators.

In this Letter we present a silver growth technique for direct-writing disconnected silver nanostructures in 3D. We leverage nonlinear optical light-matter interactions and an accompanying photoreduction reaction to fabricate 3D silver structures at the nanoscale. Previous work on direct metal writing has largely been applied to generate two-dimensional (2D) structures [7, 8, 11, 12, 68], low resolution 3D structures [8, 12], or freestanding 3D structures [6, 9, 10]. We demonstrate the writing of disconnected silver structures in 3D with 300-nm resolution and writing speeds up to 100 μm/s. The silver is grown inside a polymer support matrix, enabling us to move beyond freestanding structures to create arbitrary 3D disconnected silver patterns with submicrometer resolution. The critical difference with previous work arises from the combination of chemical reagents we use. The chemical mixture from which our samples are fabricated consists of a 0.16M $AgNO_3$ solution, with polyvinylpyrrolidone (PVP) as support polymer and water (H_2O) as solvent. Our technique does not require addition of two-photon dyes, seed nanoparticles, or non-commercially available reagents.

Most work on high-resolution 3D femtosecond laser direct-writing involves reagent combinations that either include an alcohol solvent or omit the polymer. For example, a solution of $AgNO_3$ in H_2O can be used to direct-write silver nanostructures [9], but does not offer a solid matrix for support. In contrast, an alcohol based system using $AgNO_3$, PVP, H_2O and ethanol [8, 11] has a polymer that could act as a support matrix, but the redox interactions between ethanol – OH groups and Ag^+ ions begin immediately upon reagent mixing causing nanoparticle growth throughout the sample. Thus, the ethanol mediated growth technique, as it is, cannot be used to

provide a polymer support matrix for 3D laser writing. By omitting the alcohol solvent, however, we found that the reduction reactions decrease significantly. We retained PVP as support matrix because it helps control silver nanoparticle synthesis [37, 38]. By optimizing the concentration of PVP in H_2O we simultaneously gain control over the localization of Ag^+ reduction processes and obtain a polymer support matrix.

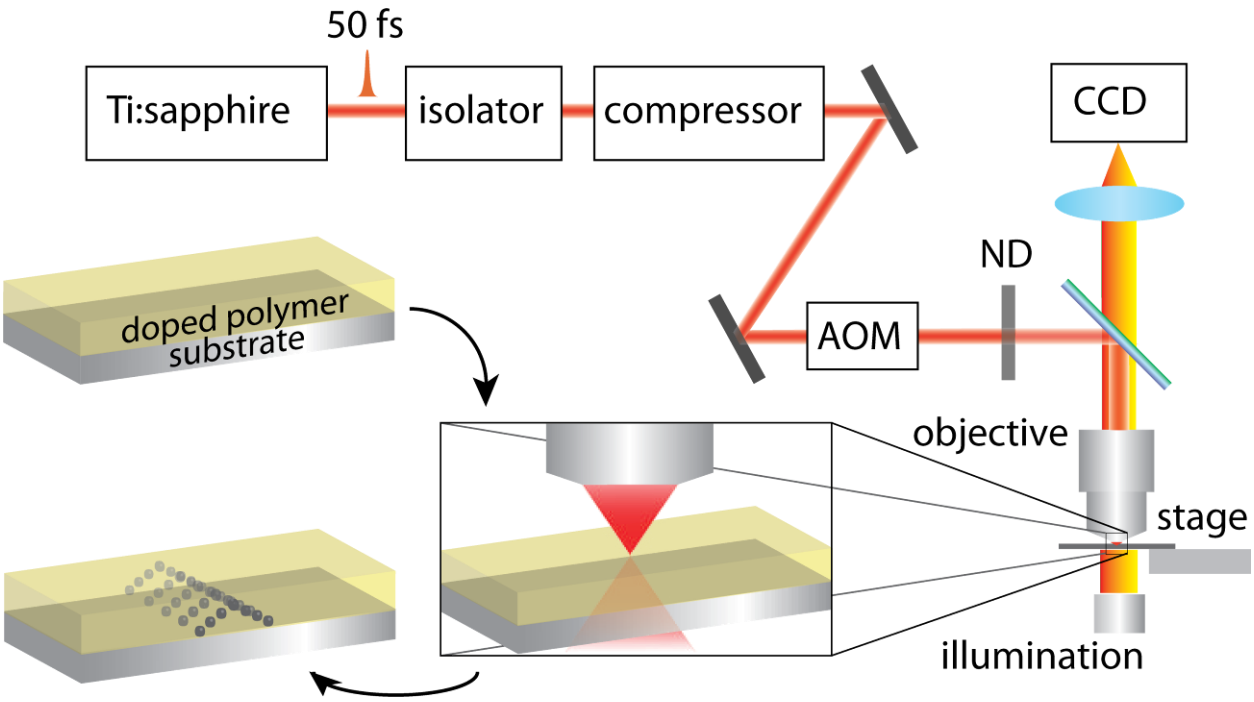

Figure 24: Schematic of the fabrication process. A microscope objective (NA 0.8) focuses laser pulses from an 11-MHz ultrafast Ti:sapphire laser system inside a doped polymer sample. The microscope objective also provides in-situ imaging. A high-precision and long-travel three-axis translation stage scans the sample in the *x*-, *y*- and *z*-directions while an acousto-optic modulator shutters laser pulses to control exposure. The result is a direct-written dielectric-embedded silver structure in 3D.

Figure 24 schematically depicts our multiphoton absorption lithography process. A solution of $AgNO_3$, PVP and H_2O is coated onto a substrate through a drop casting technique and the sample is baked to create a polymer matrix doped with silver ions. An objective with a numerical aperture (NA) of 0.8 focuses the pulses from a Ti:sapphire laser (795-nm center

wavelength, 11-MHz repetition rate, 50-fs pulse duration) into the sample. The exposure is controlled by an acousto-optic modulator and a high-precision translation stage selects the region that is exposed. At the focus, nonlinear light-matter interactions induce metal-ion photoreduction processes in a volume smaller than the diffraction-limited focal spot, initiating silver nanoparticle growth.

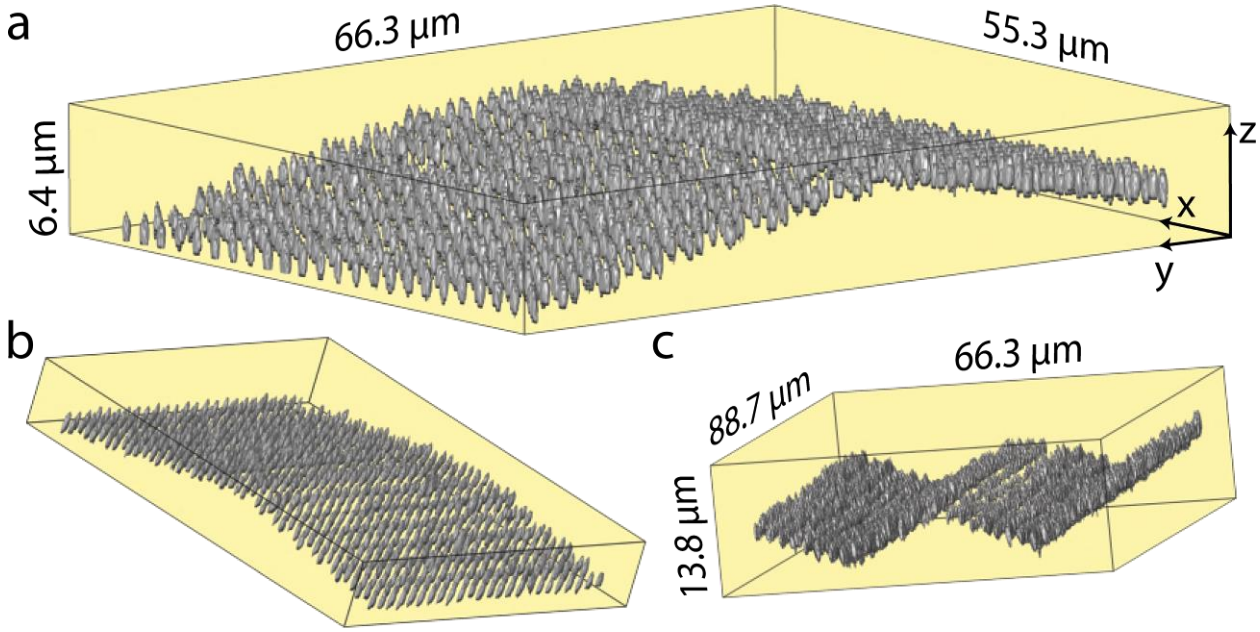

Figure 25: 3D rendering of stacks of sequential in-situ bright-field optical microscopy images of fabricated structures. For clarity, the *z*-scale is stretched by a factor of 1.6 relative to the *x*- and *y*-scales. (a,b) An array of silver dots fabricated in a tent structure at an exposure of 1.3×10^6 pulses with 0.15 nJ per voxel. Neighboring rows of dots are in different *z*-planes. The stage was translated at 10 µm/s during fabrication. (c) Portion of an array of tent structures fabricated using the same parameters.

By varying the laser parameters we can adjust the size of the resulting silver structures. At an exposure of 1.3×10^6 pulses per voxel with 0.15 nJ per pulse, we create structures clearly resolved by optical imaging. Figure 25 shows a 3D rendering of stacks of sequential 2D bright-field optical images taken of an array of silver voxels; adjacent rows of voxels are in different vertical planes. The images highlight a key attribute of our fabrication process: we can direct-write

silver structures that are disconnected in 3D inside a polymer. Figure 26 shows silver features created along the same vertical axis, further demonstrating disconnected features in the *z*-direction. When we reduce the laser exposure to 2.8×10^5 pulses per voxel with 0.2 nJ per pulse, the silver features are reduced to submicrometer scales (less than 300 nm, Figure 27). At the operating wavelength of 795 nm, the theoretical transverse resolution of our overfilled microscope objective is approximately 600 nm—about twice the size of the fabricated nanostructure in Figure 27c. Unlike most multiphoton absorption lithography techniques that use oil immersion objectives to achieve high resolution, our results were obtained with an NA of 0.8. Although higher-NA objectives have a smaller focal volume, the primary advantage of the lower-NA objective is a longer working distance (3.5 mm), which is useful for bulk 3D nanolithography. In addition to enabling 3D disconnected nanostructure fabrication, our process is approximately two orders of magnitude faster than other 3D direct-write techniques with similar resolution [6]— using an 11-MHz laser we achieve write speeds of 100 μm/s.

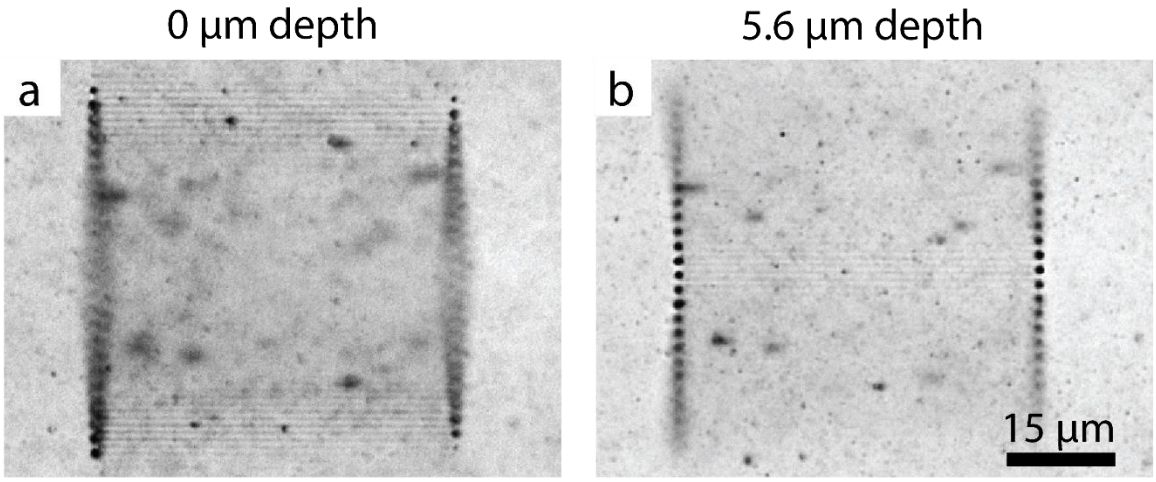

Figure 26: Stacks of sequential in-situ bright-field optical microscopy images of fabricated three-dimensional structures are used to create videos. Each image from the stack is taken at a different height by varying the distance between the sample and the microscope objective, bringing different silver features into focus. The videos show disconnected features in the z-direction by vertically scanning through structures. This sample consists of lines of dots patterned in a vertically oriented triangular pattern. (a) The optical image is focused on the bottommost layer, brining features on the top and bottom edges into focus. (b) The image is focused on the topmost layer, bringing the apex line of the triangular pattern into focus. This layer is 5.6 µm in depth compared to the bottommost layer. The dots on the left and right edges are created to be larger to help with visualization.

To determine the constituent elements in the direct written features, we used high-resolution energy dispersion x-ray spectroscopy (EDS) and scanning electron microscopy (SEM). Figure 27 shows SEM images of an array of dots fabricated on a glass substrate (see Section 4.1.1). Figure 27a and Figure 27b show the fabricated array and its corresponding high-resolution EDS silver elemental map, confirming that the fabricated dots contain silver. The presence of silver is corroborated by a strong silver signal in the EDS spectrum (Figure 28) of a patterned feature. Further characterization through transmission electron microscopy (TEM) (Figure 29) indicates that the silver does not grow as a single crystal in each irradiated voxel; rather, structures are composed of agglomerations of smaller silver nanoparticles. The inset of Figure 29 is a higher

magnification image of a single silver nanoparticle created during the fabrication process. Ultraviolet and visible micro-absorption and scattering spectroscopy (Figure 30) shows a characteristic silver surface plasmon peak centered around 425 nm. The broad extinction spectrum confirms polydispersity in the constituent silver nanoparticle size.

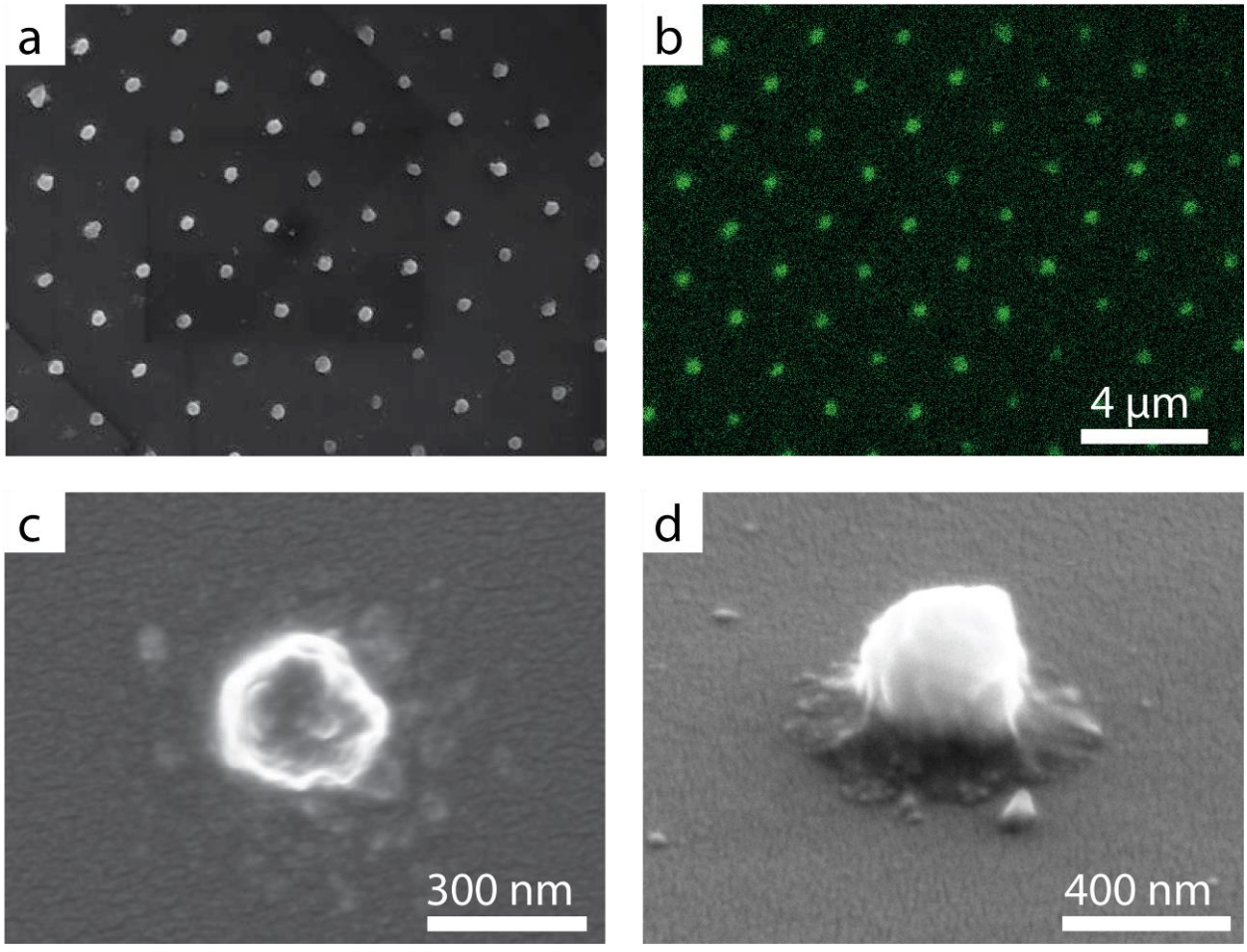

Figure 27: High-resolution SEM images of a patterned sample. (a) An image of a 2D array of dots and (b) its corresponding EDS silver elemental map confirm that silver structures are grown in areas irradiated by the laser. Close-up views of individual dots shown (c) head on and (d) at a 61° tilt angle. SEM imaging requires a washing step to avoid sample contamination from additional silver growth driven by the electron beam.

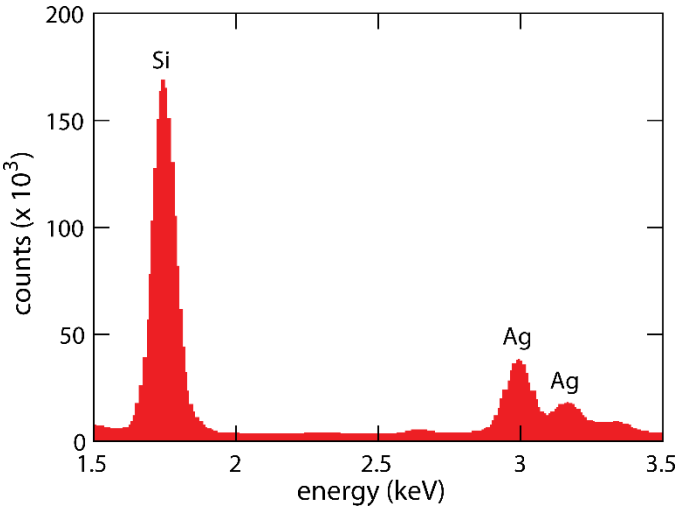

Figure 28: Energy dispersion x-ray spectroscopy (EDS) of a fabricated structure revealing a strong silver signal. The silicon signal is produced by the underlying glass substrate. EDS data collection requires a washing step to avoid sample contamination from additional silver growth driven by the electron beam. The washing step removes the metal ion containing polymer matrix, leaving behind structures fabricated directly on the substrate.

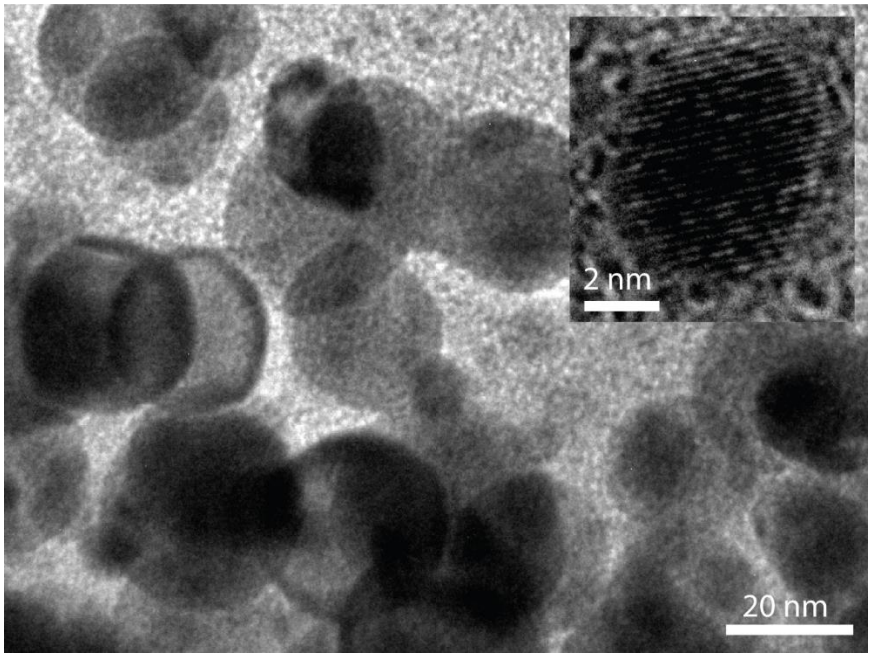

Figure 29: TEM image of fabricated silver structures. The silver does not grow as a single crystal in each irradiated voxel. Instead the silver structures are composed of agglomerations of smaller silver nanoparticles. The inset shows a close-up view of a silver nanoparticle.

The key to our fabrication process is the chemical composition of the sample. Conventional methods to synthesize silver nanoparticles and nanostructures through polyol processes [37, 38] are subject to redox reactions unfavorable for polymer-embedded 3D silver nanofabrication. In the process we present here, PVP is dissolved in H_2O, minimizing reduction reactions outside the laser-irradiated volume. PVP plays an important role in controlling the size and shape of silver nanoparticles: the strong affinity of N and O atoms in the amide groups of PVP to surfaces of transition-metal clusters restrains their growth. [37, 38, 69] By combining PVP and water we obtain both a support matrix and controlled growth; nonlinear light matter interactions then permit the direct writing of silver nanostructures in the bulk of the sample. Transmission measurements show the polymer matrix has several transparency windows in the near-infrared portion of the electromagnetic spectrum; these regions of transparency may be useful for device fabrication.

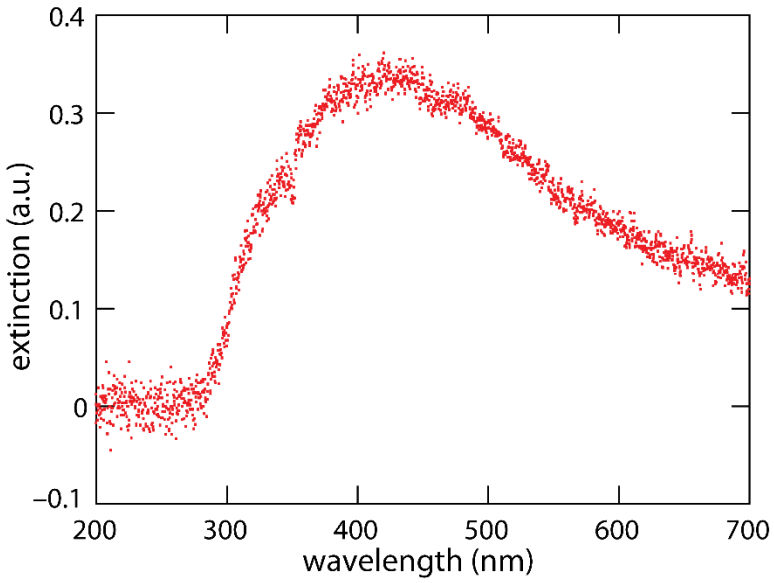

Figure 30: Ultraviolet and visible micro-absorption and scattering spectroscopy of silver patterns. The spectrum shows a silver surface plasmon peak centered around 425 nm. The broad feature of the extinction spectrum indicates polydispersity of the nanoparticle size, in agreement with TEM images.

Methods for patterning metals at the micro- and nano-scales are used extensively in broad ranging applications—from microelectronics, to optics and biosensors—highlighting the importance of metal lithography. We demonstrate high-resolution 3D disconnected silver nanostructure fabrication in a dielectric matrix through multiphoton absorption of ultrashort laser pulses. The approach presented in this Letter may permit the creation of metamaterials and other photonic devices previously limited by current fabrication techniques [1]. The process only requires readily available chemical reagents, a simple experimental setup, and a single fabrication step. By using a higher-NA objective and modifying the chemistry we expect it will be possible to further increase the resolution and fabrication speed and to extend the method to other metals, such as gold.

4.1.1 Methods

Sample preparation

To prepare samples, we dissolve polyvinylpyrrolidone in deionized water and add $AgNO_3$ to the mixture to a concentration of 0.155 M. The surface of a glass slide is then coated with the solution through drop casting. The sample is baked to create a polymer matrix doped with silver ions. Transmission measurements indicate the doped polymer matrix has several transparency windows in the near-infrared and infrared portions of the electromagnetic spectrum. To minimize silver nanoparticle formation, ultraviolet light is filtered from the room lighting.

The excitation source for fabricating silver structures is a FEMTOSOURCE scientific XL Ti:sapphire laser system from Femtolasers producing 50-fs pulses with a center wavelength of 795 nm and a repetition rate of 11 MHz. The fabrication takes place under an upright microscope. A microscope objective with a numerical aperture of 0.8 focuses laser pulses inside the sample and

provides in-situ imaging. A high-precision three-axis translation stage scans the sample in the *x*-, *y*- and *z*-directions, while an acousto-optic modulator shutters the laser beam to control the exposure.

Sample imaging

Sequential optical images taken from a microscope camera were stacked and rendered using the Amira software platform. The process used thresholding and manual adjustments of raw data to obtain 3D reconstruction. To perform scanning electron microscopy of fabricated structures, it is necessary to prevent additional silver growth driven by the electron beam. To this end we washed away the metal ion containing polymer matrix by dipping the sample in ethanol after femtosecond patterning. This leaves behind only structures fabricated at (and attached directly to) the surface of the substrate. The sample was coated with a thin gold layer to remove charging effects during imaging.

For transmission electron microscopy (TEM), we first washed the samples and then transferred the surface structures to a carbon coated TEM grid with a razor blade and ethanol. No further processing was performed on these samples.

Acknowledgments

We acknowledge Paul J. L. Webster for the 3D rendering of the optical data with Amira. Dr. Paul Peng and Professor James M. Fraser provided feedback on the manuscript throughout its development. The research described in this paper was supported by the Air Force Office of Scientific Research under grants FA9550-09-1-0546 and FA9550-10-1-0402.

4.2 3D fabrication in gelatin

This section covers research reported in: S. Kang,* K. Vora,* and E. Mazur (*co-first authors), "Direct laser writing inside a gelatin matrix for sub-100 nm 3D silver nanostructures," *Manuscript in preparation*, 2014.

Three-dimensional (3D) nanofabrication is important for realizing many types of photonic crystals and metamaterials [4, 40, 70]. Although several 3D designs requiring both metal and dielectric components have been developed, a limited number of methods allow fabrication in 3D [4, 40, 70-73]. Femtosecond laser-writing techniques have been steadily improving to provide high resolution fabrication of 3D complex patterns [3]. Direct femtosecond laser-writing is an inherently 3D method that utilizes the nonlinear interaction between laser pulses and nonlinearly absorbing functional groups of various chemicals to achieve material modification inside bulk media [5, 74, 75]. Most developments in direct laser writing have focused on polymer structures; metals, when needed, can be incorporated into certain structures post-patterning [4, 5]. The development of direct laser writing metals in 3D has been slow. Reported resolutions of direct laser written 3D metallic structures are not high enough for applications such as optical metamaterials, and only produce single layers with large surface roughness [8-10]. One exception is a recent report where 3D silver patterns were grown inside PVP; however, the resolution is still not high enough for optical metamaterial applications [53].

In this section we present a chemical mixture that yields high resolution silver nanostructures in 3D using femtosecond laser direct metal writing. Nonlinear absorption inside a gelatin matrix doped with silver ions induces the growth of silver nanostructures embedded inside the matrix.

Chapter 4 - Femtosecond laser fabrication of silver in 3D

Gelatin provides several advantages over previously reported materials for the fabrication of 3D metal nanostructures. Gelatin is an easy to use, inexpensive, non-toxic, biodegradable, water soluble polymer that has hydrogel-like gelling properties. This allows us to make thicker, more durable, less brittle, and longer-lived samples compared to PVP [53]. The doped-gelatin matrix is an order of magnitude thicker [53], allowing more layers to be patterned for bulk 3D nanofabrication. It also has over an order of magnitude longer shelf-life and fewer defects in the matrix [53]. The numerous electron donor groups in the gelatin polymer chain may help the fabrication of high resolution silver structures [76-79]. We show sub-100nm silver structure fabrication in gelatin. The matrix is also stretchable up to 10%, enabling the possibility of flexible devices. It has transparency windows that correspond well to potential applications in optical and THz metamaterials.

To prepare samples, we use a mixture of gelatin, $AgNO_3$, and deionized water. A solution is drop cast onto a glass slide, and allowed to dry at room temperature; the result is a 200-μm thick film of gelatin doped with silver ions. We use a Ti:sapphire laser producing 50-fs pulses (centered at 795 nm) with an 11-MHz repetition for the irradiation process. See Section 4.2.1 for further details into chemical preparation and laser fabrication methods.

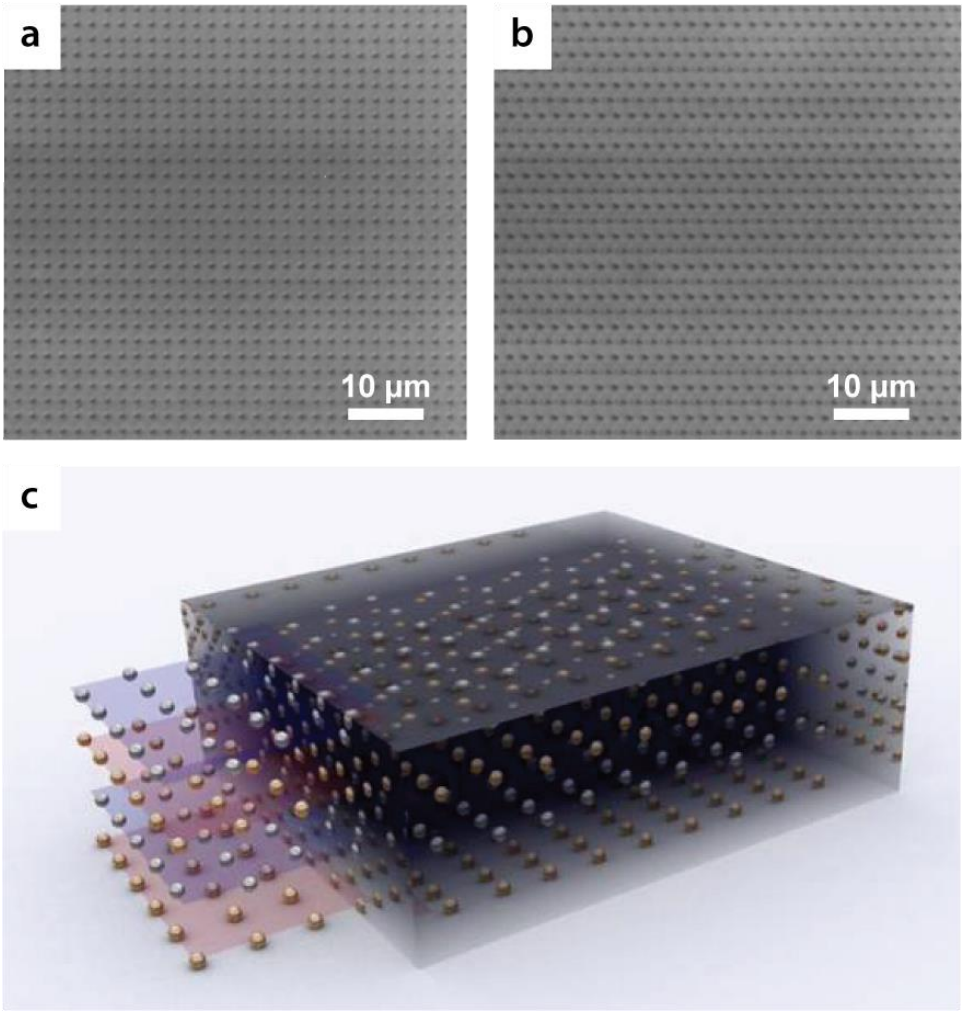

Figure 31: In-situ optical images of interleaved (a) square and (b) pseudo-hexagonal arrays of silver dots that alternate over the *z*-direction as part of a 10-layered 3D pattern inside gelatin. The pitch between dots is 2 µm in the *x*-direction, 2 µm in the *y*- direction and 4 µm in the *z*- direction. (c) (Image courtesy of Thierry Sarnet.) A computer generated image provides a schematic illustration of the 3D pattern.

Transmission optical microscopy images of a fabricated 3D silver pattern are shown in Figure 31**.** Figure 31a and Figure 31b show two representative in-situ images taken from a 10-layer array of dots. The pattern contains alternating layers of silver dots arranged in square (Figure 31a) and pseudo-hexagonal arrays (Figure 31b). The full stack of 10 layers can be seen in a video (available online as Video 1) where the microscope focal plane traverses the sample along the *z*-

axis. Figure 31c shows a computer generated model to illustrate the 3D pattern. The pattern is fabricated by irradiating layers sequentially. Since the background matrix is solid and provides mechanical support, it is possible to create silver structures that are disconnected in the *z*-direction, as shown in Figure 31. We have readily fabricated 3D patterns with over 15 layers using the single step laser writing procedure.

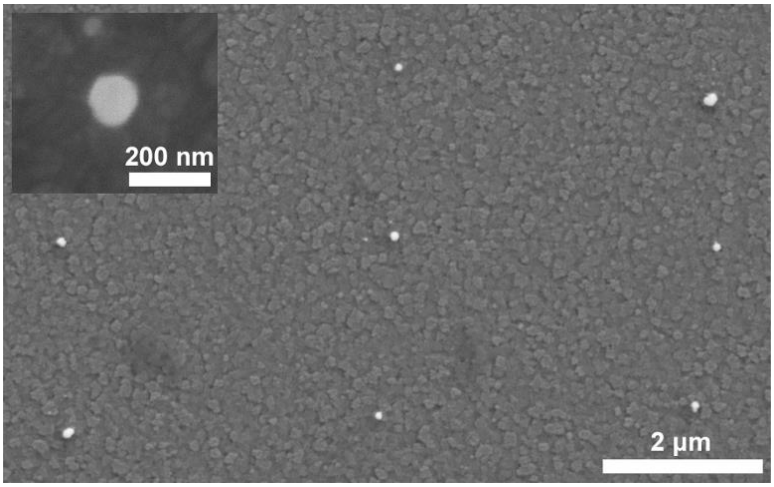

Figure 32: SEM image of an array of fabricated silver nanostructures. There is some variability in the size, with the smallest structures being sub-100nm in diameter. The inset shows a closeup view of a single silver nanostructure.

Figure 32 shows a scanning electron microscopy (SEM) image of an array of silver nanodots. We measure silver diameters as small as 80 nm, which is smaller than any other previously reported feature through direct metal writing [9, 10, 52, 53]. Unlike previous reports showing silver nanoparticle aggregates with high roughness, there are no readily visible domain separations in these nanostructures [9, 10, 52, 53]. The nanodots are fabricated with an exposure of 79,000 pulses with 0.1 nJ per pulse at a stage translation speed of 10 µm/s.

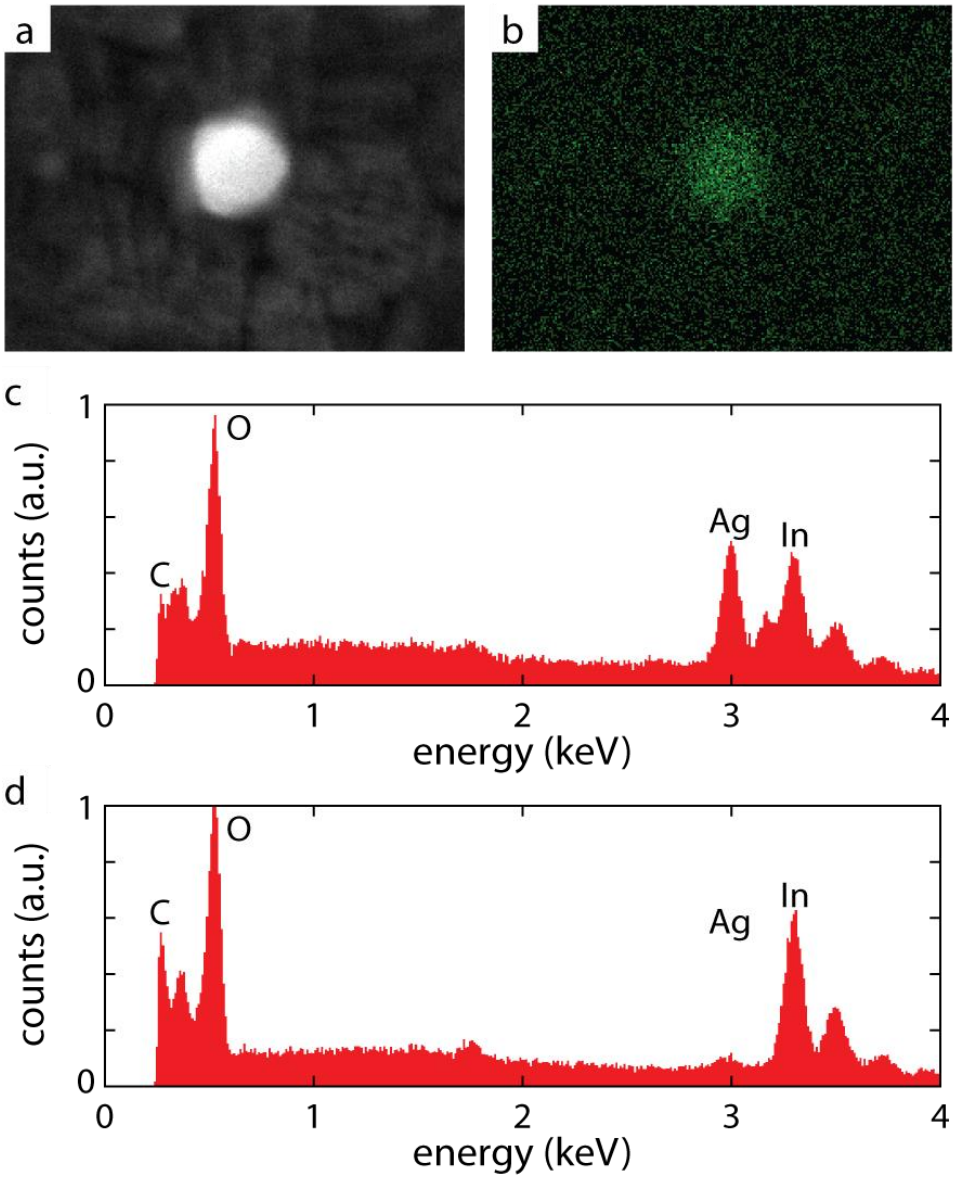

Figure 33: (a) SEM image and its corresponding (b) EDS map of elemental silver for a 100-nm fabricated structure. The EDS map shows strong silver signal from the nano-dot. The EDS spectra taken from (c) the nanodot (d) and its neighboring area clearly indicate that the silver signal stems from the fabricated nanostructure.

Figure 33 shows an SEM image of a 100 nm fabricated dot (Figure 33a) and its corresponding energy dispersion spectroscopy (EDS) map (Figure 33b). We also show EDS spectra from the nanodot and a directly adjacent area in Figure 33c and Figure 33d, respectively.

The spectra show a strong silver signal from the dot compared to the neighboring volume. The In signal is from the indium-tin-oxide layer on the substrate (under the silver dot). EDS data indicate that fabricated dots are composed of silver. Furthermore the SEM image shows a smoother structure compared to previous reports [9, 10, 52, 53]. The Ag signal from the spectrum is also significantly stronger than any previously reported for silver direct laser writing [9, 10, 53].

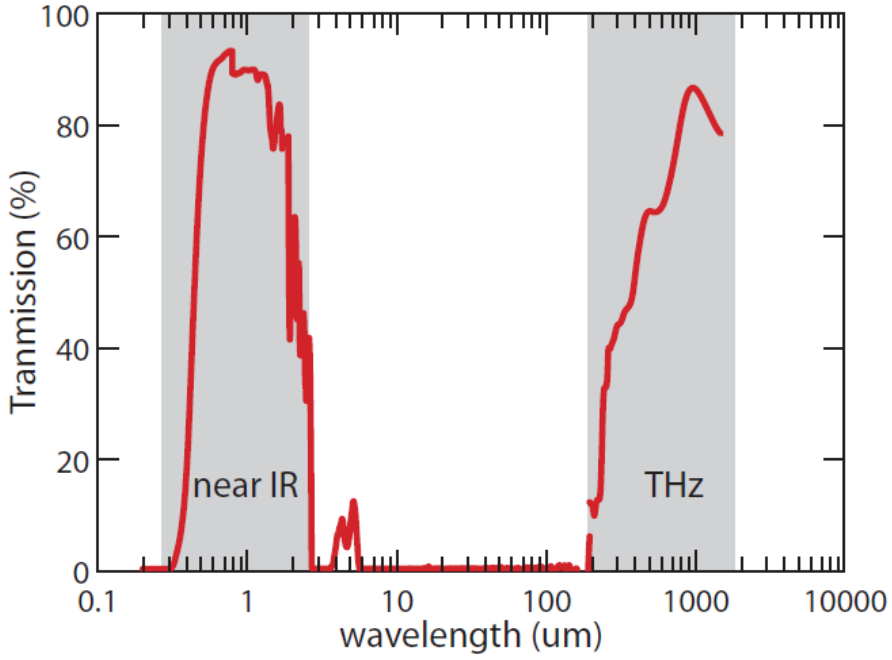

Figure 34: Transmission spectrum for an unpatterned silver-ion-doped gelatin sample. The spectrum, obtained through measurements on multiple instruments, spans the ultraviolet to terahertz wavelength range of the electromagnetic spectrum (0.2–1,500 µm). The *x*-axis is plotted with a log-scale. The spectrum shows two high transmission windows. The first window is in the visible to near-IR range and the second window is in the terahertz range. These windows indicate regions where electromagnetic devices could be designed. Figure courtesy of SeungYeon Kang, and data courtesy of SeungYeon Kang, Phil Munoz, and Alexander Shvonski.

Figure 34 shows a transmission spectrum of the doped gelatin matrix (unpatterned) spanning a range from 0.2 µm to 1,500 µm. There are high transparency windows in the optical

and THz regimes; this enables the possibility of creating electromagnetic metamaterial devices for these regions.

The critical difference between the method described here and previous reports of femtosecond laser writing metal [9, 10, 52, 53] arises from our choice of using gelatin as the background matrix. The matrix both helps growth, and mechanically supports silver nanostructures. Gelatin is comprised of high molecular weight water-soluble long protein strands derived from collagen, which leads to large amounts of –C=O, -COOH and $-NH_2$ polar groups. We hypothesize that a nonlinear optical interactions between the carbonyl group and femtosecond pulses induces a metal-ion photoreduction process, and the extra lone pairs in the polar groups (such as –COOH and $–NH_2$) restrain silver particle growth through strong affinity towards Ag^+ ions. We believe the large amount of lone pair groups with long chains of gelatin compared to other polymers restrains silver growth more effectively during femtosecond laser irradiation and allows us to fabricate silver nanostructures with sub-100-nm resolution.

The silver-ion-doped-gelatin matrix exhibits a much longer shelf-life compared to silver-ion-doped PVP matrices [52, 53]. We observe an order of magnitude increase in shelf-life, measured by monitoring optical transmission over long periods. The doped-gelatin matrix also has a significantly lower amount of defects compared to doped-PVP matrices. This can be observed by comparing optical images in Figure 31 to those from previous reports [52, 53].

Gelatin goes through a gelation process during the air-drying procedure, where abundant oxygen and hydrogen in the long protein strands form weak hydrogen bonds to create a tangled network. Water can remain captured between these hydrophilic strands, which allows gelatin to have hydro-gel like (or elastomer like) behavior. The increased viscosity allows us to make

samples that are thick (over 200 μm). Measurements with an Instron tensile testing instrument also show that samples are stretchable up to approximately 10%. By carefully choosing the gel strength and optimizing concentrations (to tune the amount of water), we obtain gelatin films that exhibit durable (reduced brittleness and increased sample lifetime) and stretchable behavior while being suitable for 3D silver growth during femtosecond laser irradiation.

In summary, the method we describe in this section takes advantage of unique gelatin properties to yield high resolution 3D silver nanostructures in a stable dielectric matrix. SEM images show sub-100-nm silver features that are much smaller than in previously published reports. Compared to other 3D fabrication techniques that yield metal nanostructures [4, 5, 9, 10, 40, 52, 53, 70, 72, 74, 75], the method presented in this section can easily produce many disconnected layers of metal patterns; we readily produce over 15 layers of structures using the single-step writing process. The doped-gelatin matrix enables bulk 3D metal nanofabrication over large volumes (we have patterned volumes tens of cubic millimeters in size). The stretchability of the matrix also opens the possibility of creating tunable optical devices. The method may enable the realization of bulk metal-dielectric optical and THz metamaterial devices that were not feasible using alternate techniques.

4.2.1 Sample preparation methods

To fabricate the nanostructures we use a mixture of gelatin, silver nitrate ($AgNO_3$), and deionized water. We first prepare a solution by dissolving 0.8 g of gelatin in 4 mL of deionized water in a vial. We mix the two components using a vortex mixer and then heat the vial in a 55 °C water bath to dissolve gelatin. We repeat this step until all the gelatin is fully dissolved. Next, we add 0.105g of $AgNO_3$ to the vial and repeat the above mixing step until all the $AgNO_3$ is completely dissolved.

We drop cast the prepared solution onto a glass slide. The sample is air-dried at room temperature overnight. The resulting sample consists of a thick gelatin film doped with silver ions on a glass substrate.

To create 2D samples for SEM analysis, the glass substrate is oxygen plasma treated and silanized with mercapto propyl trimethoxy silane (MPTS) prior to drop casting. Laser irradiated samples that include patterns fabricated at the glass interface are immersed in water at 55 °C to dissolve the polymer layer, leaving behind 2D patterns bound to the substrate for further analysis.

Gelatin and $AgNO_3$ were purchased from Sigma-Aldrich, and MPTS was purchased from Alfa Aesar. Gel strength is determined by a method developed in 1925 by O. T. Bloom [80]. For these experiments, we chose a Bloom grade of 75.

4.2.2 Laser fabrication methods

We use a Ti:sapphire laser centered at 795 nm with an 11-MHz repetition rate, and 50-fs pulse length for the irradiation process. A detailed description of the laser fabrication setup can be found in Chapter 2. 3D structures are created by focusing laser pulses inside the bulk of the gelatin matrix; layers are patterned sequentially starting from the layer closest to the substrate and moving towards the air interface. This is a single step process and does not require any further processing. To create planar 2D patterns that are suitable for SEM analysis for example, laser pulses are focused near the substrate such that the grown silver is bound to the glass.

4.2.3 Characterization methods

SEM and EDS measurements were performed in Zeiss Ultra and SUPRA 55VP microscopes, using in-lens and EDAX detectors.

The stretcheability of a 200-µm thick silver-doped gelatin matrix was determined by using an Instron 3342 tensile measurement setup.

Transmittance measurements were performed on 4 different regions of a 200-µm thick unpatterned matrix. The 0.2–1.75 µm wavelength range was probed using a Cary 500i UV-Vis-NIR dual-beam spectrophotometer. Transmittance in the 1.8–15 µm wavelength range was measured using a Thermo Fisher continuum fourier transform infrared (FTIR) microscope connected to a Thermo Fisher FTIR6700 spectrometer. The 15–200 µm wavelength range was measured using a Thermo Fisher FTIR6700 spectrometer. The 200–1,500 µm (THz) range was measured using a broadband Hg-arc lamp THz source and a liquid helium-cooled Si bolometer detector.

4.3 Summary

We have developed two combinations of silver nitrate and polymer that are suitable for 3D metal nanofabrication.

A simple mixture of PVP, $AgNO_3$ and H_2O allows the creation of sub-micrometer silver nanostructures that are embedded inside a support matrix. We demonstrate 300-nm silver features using our optical setup [52, 53]. The microscope objective used in this experiment has an NA of 0.8 and a working distance of 3.5 mm, allowing the potential to pattern thick 3D samples. Stronger focusing—an NA of 1.4 is typical for femtosecond laser patterning techniques—would lead to a much smaller laser spot size with the tradeoff of a shorter working distance.

We also present the fabrication of silver nanostructures in 3D inside gelatin. Nonlinear absorption inside a gelatin matrix doped with silver ions induces the growth of silver

nanostructures embedded and fixed inside the dielectric matrix. 2D SEM images show sub-100-nm features. Gelatin provides several advantages over previously reported materials for the fabrication of 3D metal nanostructures. We show sub-100nm silver structure fabrication in gelatin. Gelatin is an easy to use, inexpensive, non-toxic, biodegradable, water soluble polymer that has hydrogel-like gelling properties. This allows us to make thicker, more durable, less brittle, and longer-lived samples compared to PVP. The doped-gelatin matrix is an order of magnitude thicker, allowing more layers to be patterned for bulk 3D nanofabrication. It also has over an order of magnitude longer shelf-life and fewer defects in the matrix. The matrix is also stretchable up to 10%, enabling the possibility of flexible devices. It has transparency windows that correspond well to potential applications in optical and THz metamaterials.

The resolution of both methods could be increased with stronger focusing optics. Additional pattern shapes, such as short lines, can be obtained by scanning the laser continuously over a distance (see Chapter 5 and Chapter 6). Potential applications include negative index metamaterials, perfect lenses, and antenna arrays for optical, near-infrared, and THz wavelength regimes [1, 3, 40, 59-61, 68].

Chapter 5 The effects of laser exposure parameters on 3D silver growth in gelatin

This chapter covers research reported in: K. Vora, C. Evans, and E. Mazur, "The effects of laser exposure parameters on 3D silver growth in gelatin," *Manuscript in preparation*, 2014.

Recently, femtosecond laser writing in polymers and glasses has gained significant popularity for creating 3D optical devices [3, 13]. Femtosecond laser writing of silver in 3D has also seen recent developments that enable the fabrication of disconnected metal patterns in three-dimensions [53]. The combination of gelatin and $AgNO_3$ has been shown to have certain advantageous material properties compared to PVP and $AgNO_3$ for use as 3D metal fabrication matrix (see Chapter 4): increased sample thickness, longer material shelf-life, and lower amount of defects in the matrix. We further investigate the material's suitability as host for 3D fabrication by studying the effect of multi-layer patterning on feature size. We show that silver growth is localized around the focal volume and does not affect adjacent features. Further, as previous demonstrations of 3D patterning are limited to simple arrays of dots, we create complex 3D silver patterns to highlight the capabilities of the technique. Several demonstrated patterns cannot be realized, to the best of our knowledge, through any other fabrication technique. Possible applications for direct metal writing include sensing, plasmonics, and metamaterials [1].

Chapter 5 - The effects of laser exposure parameters on 3D silver growth in gelatin

Although a handful of reports demonstrate 3D silver fabrication using irradiation from femtosecond pulses [2, 6-8, 10, 53], a detailed understanding of the silver growth process has not been studied experimentally. Compared to TPP [3, 20], femtosecond laser metal writing is complicated by the fact that the material grown through the irradiation process is not transparent and absorbs light linearly, leading to additional thermally-driven growth. By understanding and exploring this balance between linear and MPA induced metal growth, we investigate a potential opportunity for greater control over metal particle size and location during the laser-writing process. Note that we limit these experiments to the irradiation of individual voxels rather than continuous lines; this minimizes the silver growth's dependence on translation velocity as well as the effect of seeding by silver grown in directly adjacent areas.

Two-photon dyes can be used to facilitate the silver fabrication process [10]; however, no reports observe the effect of nonlinear absorption for the metal growth in the absence of these dyes. Baldacchini et al. show that MPA induces silver growth in PVP by noting a lack of silver growth during continuous wave laser irradiation [11]. No experimental studies explore the interplay between MPA and linear absorption for femtosecond laser growth of silver.

In this chapter, we study the effect of laser exposure on silver particle diameter in gelatin. We observe the size dependence as a function of laser-pulse energy and number of pulses (exposure time), revealing two contributions to the growth mechanism: nonlinear absorption induced (NL) growth and linear absorption induced (LA) growth. We investigate these two mechanisms for silver growth by varying the pulse spacing and pulse duration. By varying the duty cycle (pulse spacing), we show that heat accumulation accelerates growth and leads to larger silver particles with a timescale for heat diffusion on the order of 1 μs. Furthermore, by varying

the laser pulse duration, we find that silver particle size increases for higher peak power (at constant pulse energy); thus, we provide experimental evidence of NL silver growth in the polymer matrix. These results suggest that both LA and NL growth mechanisms are involved during femtosecond laser writing of silver and imply that by tuning these mechanisms, we can achieve tighter control over particle size during 3D fabrication.

To study the effects of LA versus NL growth, we utilize a laser system that generates 66-fs pulses centered at 795 nm with a repetition rate of 11 MHz. We use the experimental setup described in Figure 10 and gelatin films doped with Ag^+ (from $AgNO_3$) as described in Section 4.2.1. We focus the laser pulses into the samples using a 0.8-NA microscope objective. An AOM, ND filters, and a pulse shaper allow us to control exposure conditions. This laser system provides a balance of high pulse-energy and adjustable repetition rate that make our results broadly applicable to many common laser configurations.

5.1 3D patterning

The advantage of femtosecond laser fabrication in doped-gelatin compared to techniques such as TPP is the ability to create disconnected metal structures in 3D. However, the process of patterning a layer of silver structures can affect silver fabrication in subsequently irradiated layers if silver growth is not fully localized around the focal volume. We investigate the material's suitability as host for 3D fabrication by studying the effect of multi-layer patterning on feature size. Furthermore, as previous demonstrations of 3D patterning are limited to simple arrays of dots, we demonstrate complex 3D silver patterns that, to the best of our knowledge, cannot be realized through any other fabrication technique.

Chapter 5 - The effects of laser exposure parameters on 3D silver growth in gelatin

If silver growth is not strictly limited to the focal volume of the laser and there are nanoparticles grown outside this volume, these nanoparticles will act as seeds during subsequent laser irradiation and accelerate growth in adjacent volumes. We would expect subsequently patterned layers to exhibit larger particle size for identical exposure conditions. Thus, highly localized growth is important to obtain predictable features for 3D fabrication.

We create 1-layer and 2-layer patterns and compare feature sizes in each of the three layers. The exposure time is 500 μs at 0.09 nJ per pulse. The layer-to-layer pitch is 5 μm: we choose this dimension to minimize the effects of scattering between layers during optical imaging with the in-situ microscope. Each data point is obtained by averaging the size of over 300 silver particles.

We obtain experimentally identical diameters for the three arrays: each has an average diameter of 1.3 μm, with standard deviations of 0.1 for the 1-layer pattern, and 0.2 and 0.1 for the top and bottom structures of the 2-layer pattern, respectively. There is no measurable difference in silver structure size when patterns are created on top of each other. We thus conclude that, within the imaging limits of our optical microscope, silver growth is strongly localized around the laser focal volume. This localization is especially important for applications requiring bulk 3D patterns.

In Figure 31 of Chapter 4, we show two slices of a 10-layer array of dots. To observe the 3D fabrication capabilities beyond simple arrays of dots, we create silver patterns with increasing complexity. The patterns have a combination of straight and curved lines in all three spatial dimensions, stacked over multiple layers. Figure 35, Figure 36, Figure 37, and Figure 38 show optical images and 3D diagrams of these patterns. The full data sets for these patterns can be seen online in Video 2, Video 3, Video 4, and Video 5, respectively. Figure 35 shows a 15-layer array of intertwined rings (with a diameter of 8 μm), where each subsequent layer is offset by half a

radius. Figure 36 shows a 4-layer array of 2.5-μm donuts, with sub-diffraction dots in between. Figure 37 shows a 5-layer array of unit cells consisting of interconnected pairs of rings draw along vertical and horizontal axes. Figure 38 shows a 3D array of 4 x 4 x 3 disconnected unit cells, where the unit cells have silver rings drawn at the facets of a virtual cube. These patterns are created with the following laser irradiation parameters: pulse energy between 0.12 and 0.15 nJ, translation velocity between 50 and 200 μm/s, and 15 ms exposure windows with 20 ms duty cycles.

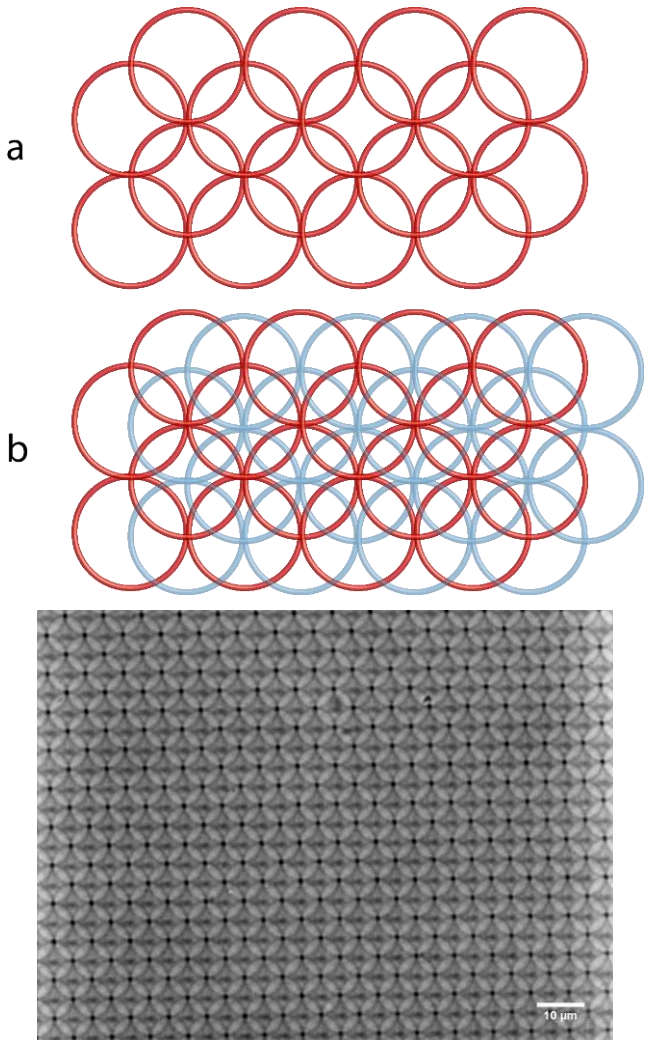

Figure 35: Schematic of (a) one layer of a 15-layer pattern of intertwined rings. (b) Subsequent layer are offset the radius of one ring. The optical image shows layer 12 of a 15 layer pattern. The pattern is created with the following laser irradiation parameters: 0.12 nJ pulse energy, 50 µm/s translation velocity, and 15 ms exposure windows with 20 ms duty cycles.

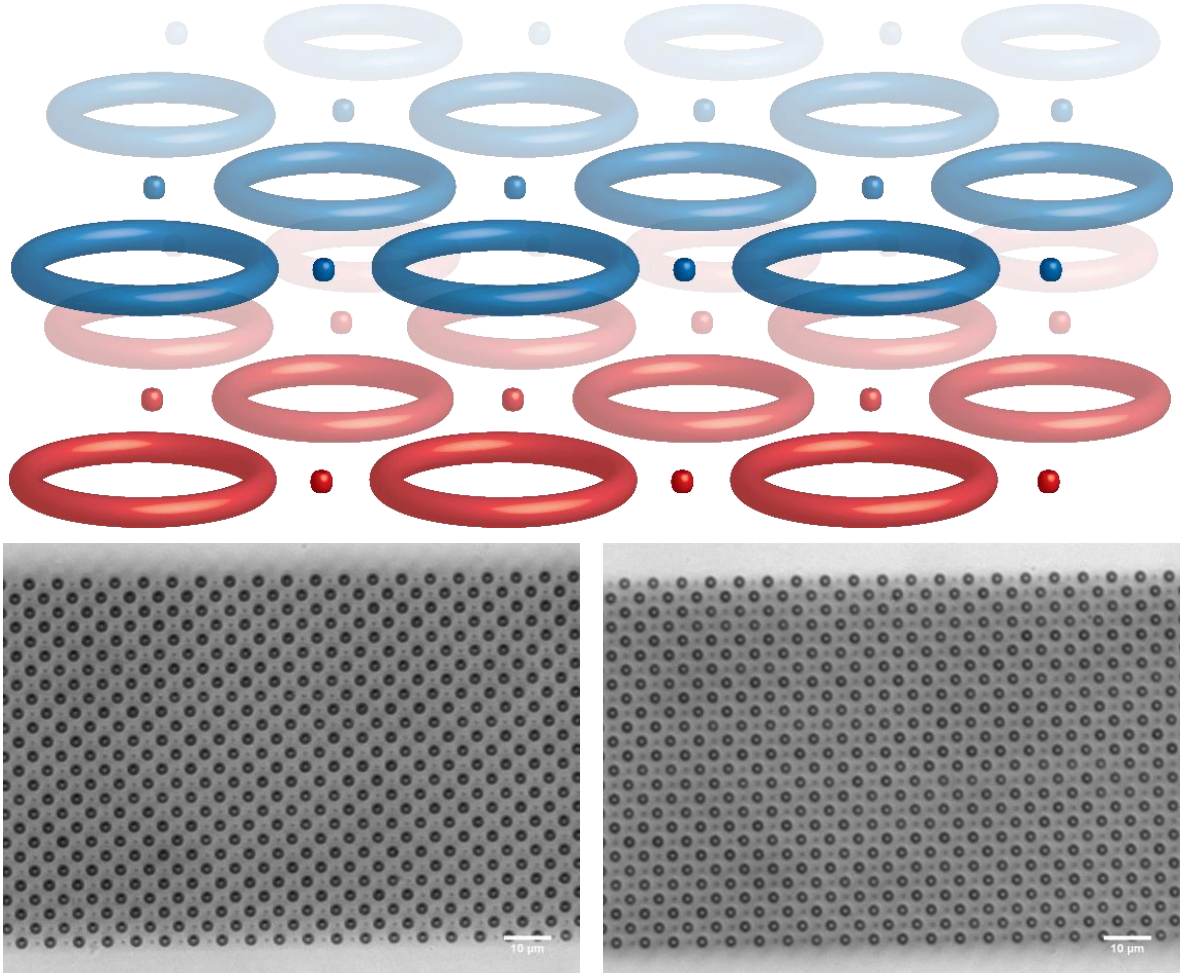

Figure 36: Schematic and optical images of an array of donuts and dots on multiple layers. Optical images show the top and bottom layers of the 4-layer pattern. The pattern is created with the following laser irradiation parameters: 0.14 nJ pulse energy, 50 µm/s translation velocity, and 15 ms exposure windows with 20 ms duty cycles. The donuts are created by scanning the laser in a circular motion three times before proceeding to subsequent features.

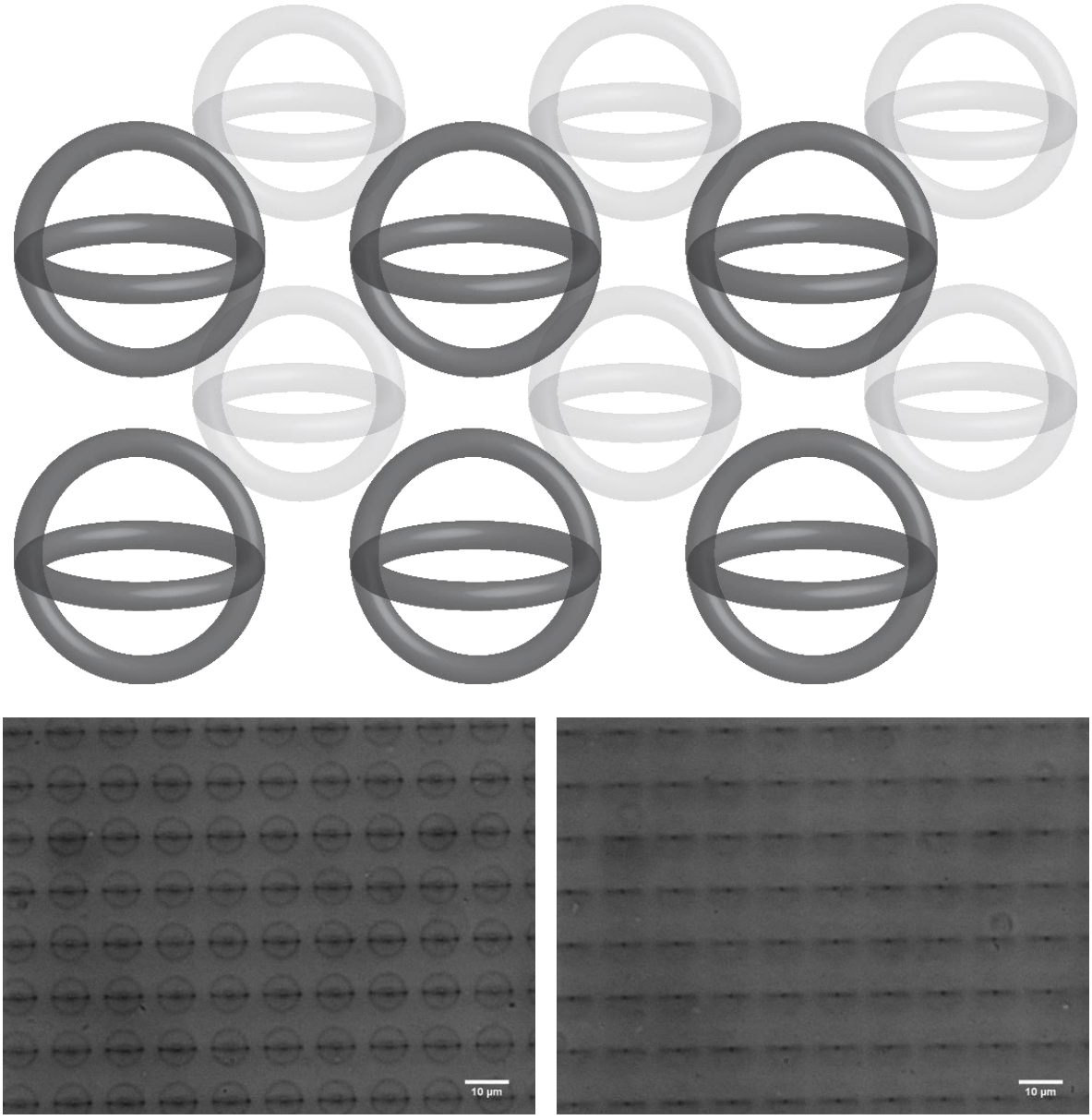

Figure 37: Schematic and optical images of an array of orthogonal double-rings. The rings are unit cells are disconnected from each other in all three spatial directions. Optical images show horizontal rings, and the top of vertical rings. The rings are from the first layer of 5-layer array of ring pairs. The pattern is created with the following laser irradiation parameters: 0.15 nJ pulse energy, 100 µm/s translation velocity, and 15 ms exposure windows with 20 ms duty cycles.

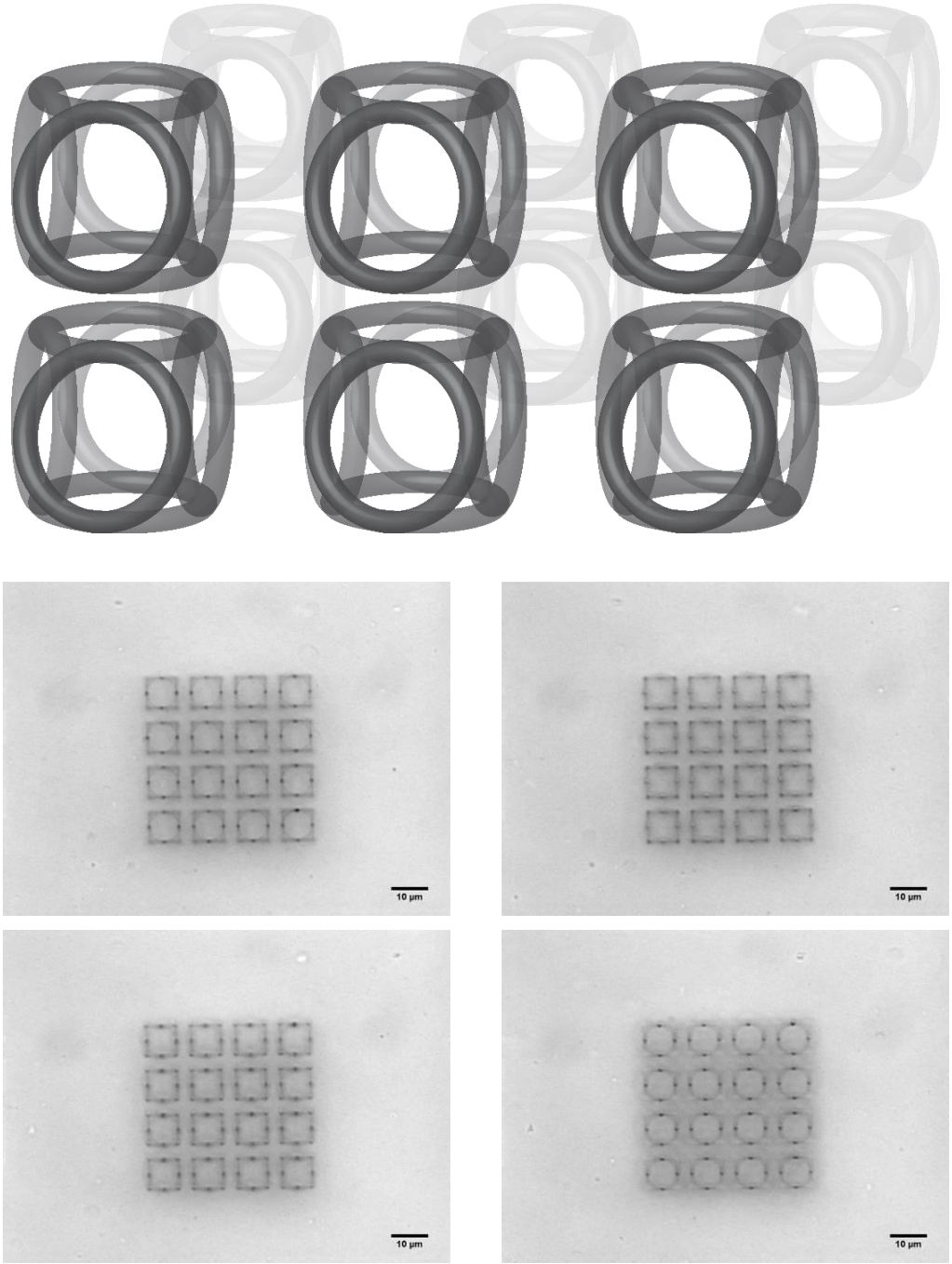

Figure 38: Schematic and optical images of a 3D array of disconnected unit cells, where the unit cells have silver rings drawn at the facets of a virtual cube. The optical images are taken at 4 depths of the first layer of unit cells. The pattern has 3 layers of unit cells. The pattern is created with the following laser irradiation parameters: 0.14 nJ pulse energy, 200 µm/s translation velocity, and 15 ms exposure windows with 20 ms duty cycles.

Chapter 5 - The effects of laser exposure parameters on 3D silver growth in gelatin

Femtosecond laser fabrication in gelatin doped with $AgNO_3$ provides precise control over silver growth in all three spatial dimensions over macroscopic volumes (mm^3). Since the metal structures are created inside the gelatin polymer matrix, they can be supported independently of other metal structures—unit cells can be disconnected over *x*-, *y*-, and *z*-direction. Many of the demonstrated complex metal patterns cannot be realized using any other fabrication technique. The femtosecond writing technique could lead to new experiments and applications in optics, metamaterials, and other fields of research.

The experiments in the following sections explore silver growth by studying size as a function of laser parameters. Note that we limit these experiments to the irradiation of individual voxels rather than continuous lines; this minimizes the silver growth's dependence on translation velocity as well as the effect of seeding by silver grown in directly adjacent areas.

5.2 The effect of pulse energy and exposure time on silver particle size

The size of silver particles grown through femtosecond laser irradiation is affected by several laser parameters. The simplest parameters we can vary are the pulse energy (E) and the exposure time (τ_e). Attenuating our laser system controls E while the AOM controls τ_e. Together with the repetition rate (RR), these parameters determine the number of laser pulses ($n = \tau_e RR$) during irradiation and the dose ($D = nE$). For a linear growth mechanism, we expect that the same dose should produce the same size silver particle. In this study, we explore the relation between pulse energy, exposure time, and dose to quantify their effect on silver growth.

Chapter 5 - The effects of laser exposure parameters on 3D silver growth in gelatin

We observe silver growth while varying both the pulse energy and exposure time over ranges spanning 3 orders of magnitude (from 4 pJ to 2.7 nJ) and 9 orders of magnitude (from 300 ns to 1,000 s), respectively. Figure 39a and Figure 39b show two representative optical images of silver particle growth with exposures of 1.2 μs at 2.7 nJ and, 10 s at 4 pJ. We see that it is possible to grow silver with a very broad range of exposures.

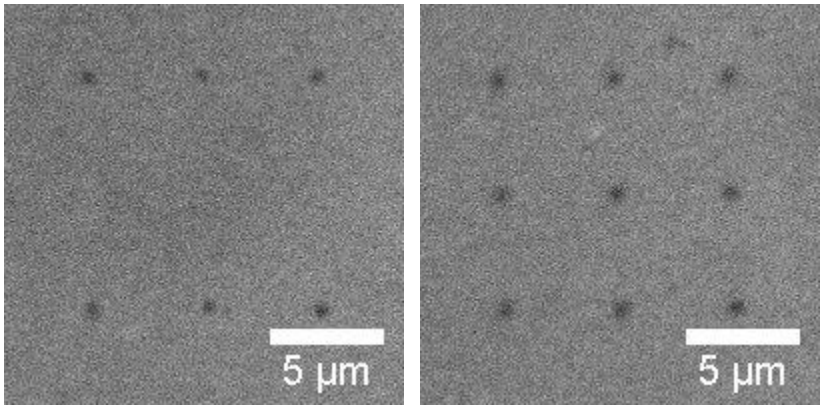

Figure 39: Transmission optical microscopy images of silver particles grown with exposures of (a) 1.2 μs at 2.7 nJ and (b) 10 s at 4 pJ.

We irradiated arrays of spots with a range of exposure conditions and measured the feature sizes in-situ using a transmission optical microscope to determine the dependence of silver particle size on laser exposure. Since we measure particle size in the bulk of the gelatin matrix using an optical microscope, the results are limited by diffraction to approximately 0.6 μm. Particles with apparent diameters below this limit (as determined by our optical images) cannot be accurately measured using this technique and we label them as "sub-diffraction." It is possible to obtain exact sizes for sub-diffraction particles through SEM imaging or analysis of particle scattering signal. Figure 32 in Chapter 4 shows an SEM image of deeply sub-diffraction particles (~100 nm) grown with an exposure of 0.2 nJ and 7 ms. Silver dots larger than approximately 6 μm exhibit irregular

shapes that are difficult to quantify and are less technologically relevant. Thus, we limit our analysis to silver particles between 0.7 and 6 μm in size.

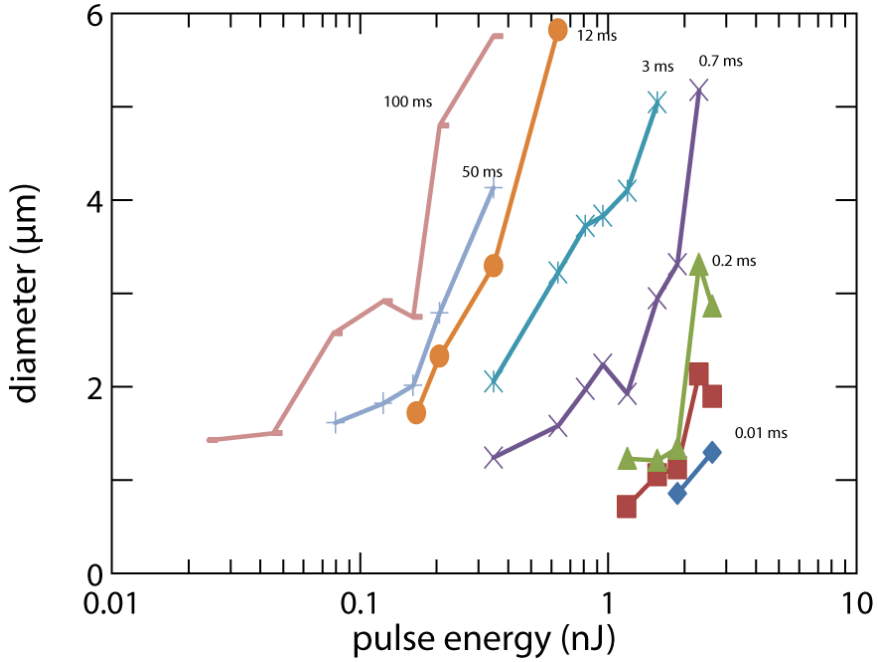

Figure 40: Size versus pulse energy for several constant exposure times.

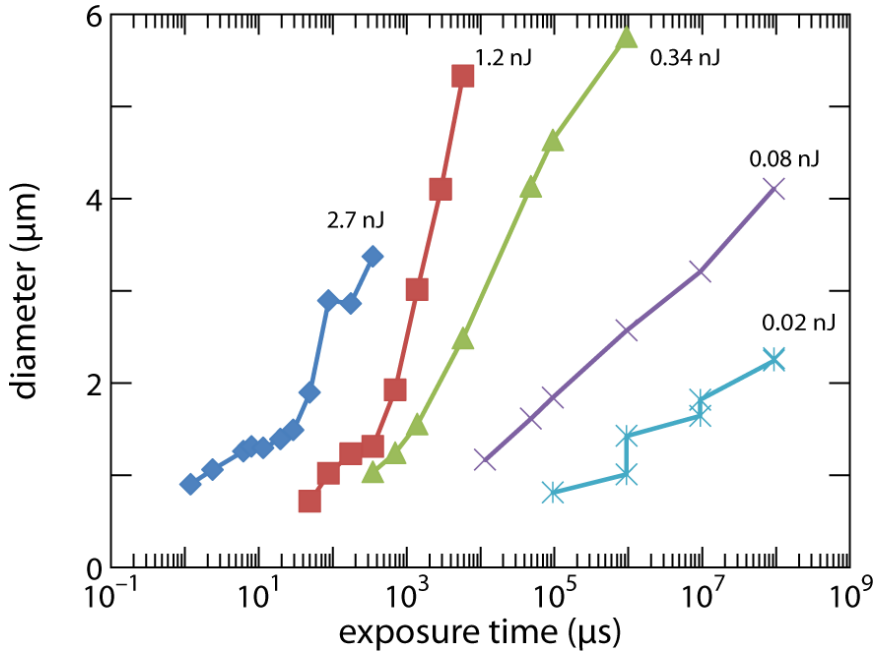

Figure 41: Size versus exposure for several constant pulse energies.

Figure 40 shows the dependence of particle size on pulse energy for several constant exposure times. Figure 41 uses similar data and displays the particle diameter as a function of exposure time for several fixed energies. Both charts show the expected trend: increasing pulse energy or exposure time increases particle diameter.

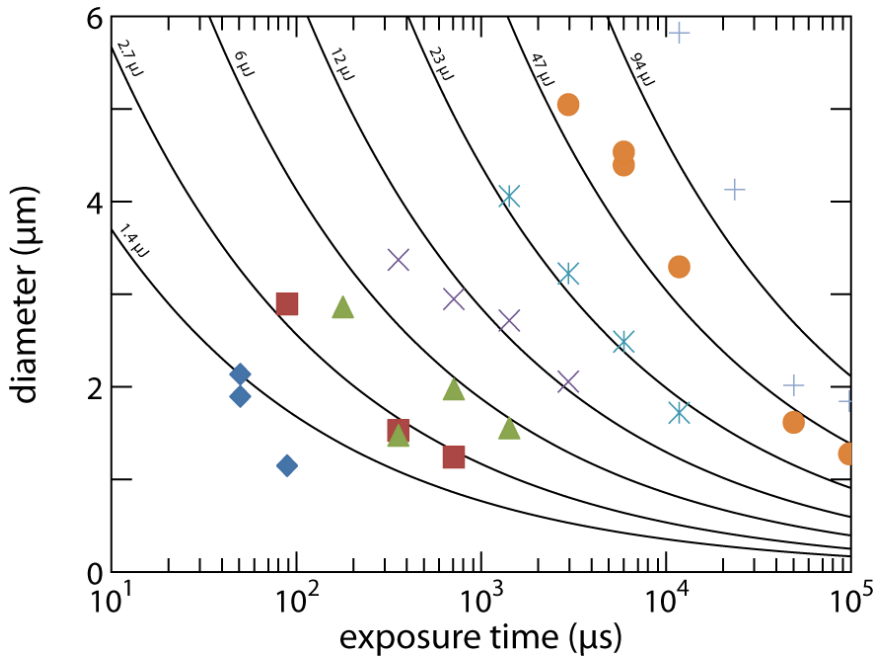

Figure 42: Size versus exposure for constant dose (± 15%) and phenomenological fit using Equation 5.1.

Additional insights can be gleaned through plotting particle size versus exposure time for a constant dose. Figure 42 shows a selection of data for constant doses between 1.4 and 94 μJ. For a linear growth mechanism, we expect a constant dose to produce the same size silver particle irrespective of power or exposure time. However, Figure 42 shows that particle size decreases with longer exposures (lower pulse energies) for the same dose. For example, 10^4 pulses at 0.1 nJ will produce smaller features than 5×10^3 pulses at 0.2 nJ. We are able to fit all the curves from Figure 42 to a single analytical expression:

$$d = cE^{0.62}\tau_e^{0.34}, \tag{5.1}$$

where d is the diameter, and E is pulse energy, and τ_e is exposure time. If we assume that silver dots are perfectly spherical, then the particle volume depends nearly linearly on the exposure time and quadratically on pulse energy. We attribute the nonlinearity of silver growth to the combined effects of heat accumulation and MPA, which we explore in the following sections. Further details into the exact growth mechanism that leads to the nonlinear relationship would require additional analysis of sub-diffraction particles with SEM, and pump-probe spectroscopy.

5.3 The effect of heat accumulation on silver particle size

In the previous section, we discussed the effect of changing laser exposure time, pulse energy, and dose on the size of the resulting silver particles and observed a nonlinear dependence with exposure time for a constant dose. This indicates that the cumulative effect of heat may be an important parameter in determining the final silver particle size; previous studies on femtosecond laser micromachining of glass and TPP have shown that heat accumulation plays a significant role in determining features sizes [20, 81, 82]. In this section, we explore the effect of varying the time gap between pulses (duty cycle) on size to determine the relevant timescale for heat accumulation in the silver-ion-doped gelatin.

When a laser pulse is absorbed by a medium, part of the absorbed energy is converted into heat. After a sufficient amount of time, thermal energy diffuses out of the focal volume, which returns to room temperature. However, if a subsequent pulse of light is absorbed within a very short amount of time, heat is not able to completely diffuse out of the focal volume before the second pulse arrives and thermal energy accumulates. Figure 43 illustrates two scenarios for heat

accumulation arising from the use of a 1-kHz versus a 25-MHz repetition rate laser, where the thermal diffusion time is on the order of 1 μs (which is typical for glass) [82]. In the first case, there is no heat accumulation, whereas in the second, the temperature increases with subsequent pulses. Since silver growth can be driven thermally in gelatin [77], the accumulated heat provides an additional mechanism to drive the silver growth process. It is therefore important to quantify the relevant time-scales for thermal energy accumulation to find a balance between repetition rate, pulse energy, and exposure time for laser-induced silver growth.

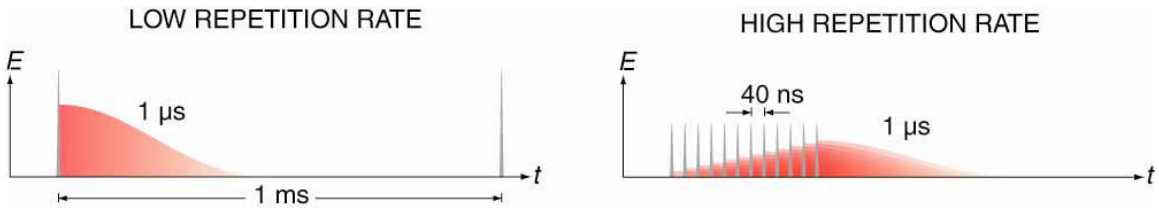

Figure 43: The plots show how thermal energy (red) in a focal volume varies over time during exposure to laser pulses (grey). When the pulse-to-pulse separation time is shorter than the thermal diffusion time of a material, the energy deposited by each pulse diffuses out of the focal volume before the arrival of subsequent pulses (left). When the repetition rate is high compared to thermal diffusion time, energy accumulates in the focal volume and increases the temperature (right) with each pulse. Adapted from Reference [82].

We study the effects of heat accumulation during growth by changing the pulse repetition rate and observe the effect that pulse spacing has on particle size. We use an AOM to change the effective repetition rate of our system. The stage-AOM system is not fast enough to isolate individual pulses; therefore, we create bursts of two-pulses. By changing the burst gap (τ_g) while keeping the dose constant, we infer the timescale for heat diffusion by observing the resulting silver particle diameter.

We obtain a timescale for heat diffusion by studying the effect of varying the time gap τ_g between bursts on particle size. Figure 44 shows a plot of silver nanoparticle diameter (averaged

over 10 separate exposures) as a function of τ_g. We hold the dose constant at 0.52 µJ (200 pulses at 2.6 nJ per pulse), which allows for comparatively short fabrication times. Silver size decreases rapidly when τ_g increases from 0 to 0.2 µs, and then remains constant as τ_g is increased beyond 0.8 µs. Performing additional experiments while varying E (between 1.3 and 2.9 nJ) and dose (between 58 nJ and 26 µJ) yields similar results. We see from these sets of data that a gap-spacing longer than approximately 0.8 µs eliminates the dependence of particle size on τ_g.

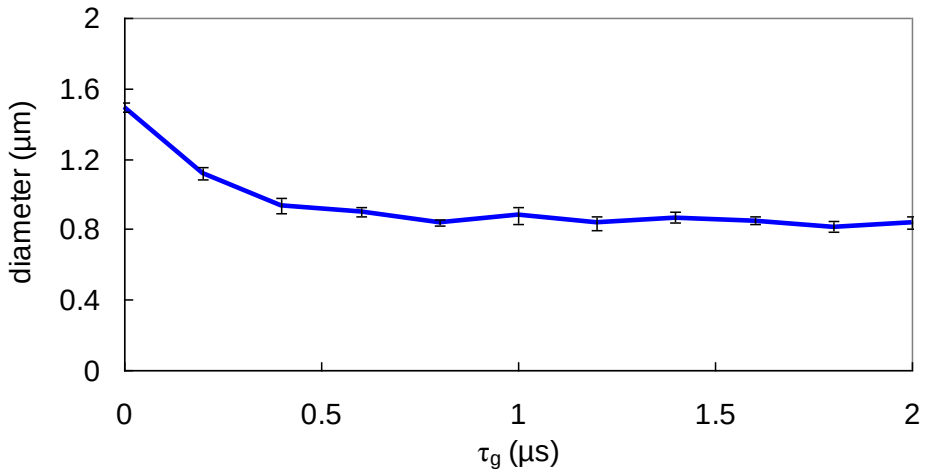

Figure 44: Particle diameter as a function of τ_g for constant total exposure.

The silver particle size dependence on τ_g can be explained by heat accumulation [20, 82]. Part of the energy from laser pulses absorbed by the silver particle in the gelatin matrix is transformed into heat. The heat diffuses from the silver particle to the surrounding polymer medium. When subsequent pulses irradiate the particle within less than 0.8 µs, the heat is not able to completely diffuse out of the growth volume and the temperature increases. The temperature increase significantly increases silver growth. The chart in Figure 44 shows that reducing τ_g from 1 µs to 0 µs yields an 80% increase in final diameter to 1.5 µm for a constant total dose. Thus, we infer that tailoring the laser energy deposition rate into the silver-ion-doped material has a strong

effect on growth dynamics. The 0.8 μs thermal diffusion timescale is consistent with other thermal processes [13] and comparable to heat diffusion in glass [82]. Therefore, growth induced by heat accumulation is significant for nJ pulse energies if pulses are delivered at a spacing shorter than approximately 1 μs.

Our observation of thermally induced growth has important implications for direct laser writing. We conclude that heat diffuses out of the growth volume with a timescale of approximately 1 μs. Thus, we expect that samples irradiated with a laser having a repetition rate greater than approximately 1 MHz will be subject to heat accumulation. As typical femtosecond mode-locked solid-state laser oscillators have repetition rates from 50 – 1000 MHz, we expect heat accumulation to play an even greater role during fabrication with those systems if steps are not taken to mitigate this effect. Meanwhile, systems with much lower repetition rates (< 1 MHz)—particularly amplified solid-state lasers—should not subject samples to heat accumulation. We establish a timescale where repetition rate becomes a third variable, in addition to pulse energy and exposure time, to determine feature size during fabrication. The additional degree of freedom provides a broader choice of parameters for optimizing fabrication speed and feature size. Heat accumulation becomes an important consideration for manufacturing purposes where high throughput is necessary.

5.4 The effect of pulse duration on silver particle size in gelatin

Two-photon dyes can be used to facilitate the silver fabrication process [10]; however, there is a lack of experimental work studying the NL growth mechanism in the absence of these dyes. Baldacchini et al. state that the silver growth in their process—using $AgNO_3$, PVP, ethanol, and

water—is induced by MPA, since they do not observe any growth during continuous-wave irradiation [11]. To gain further understanding of the effect of MPA, we study silver particle size with varying pulse durations to change the peak power. We measure the pulse duration with an autocorrelator and change its duration by introducing chirp (group-delay dispersion) with a pulse shaper.

We hold the pulse energy constant while increasing the pulse duration for several different exposure times. The optical microscopy image in Figure 45 shows silver dots fabricated with pulse durations ranging from 66 to 390 fs and exposure times between 2 and 1000 μs, all with a pulse energy of 2.1 nJ. We see that for the same exposure time, silver features increase in size with shorter pulses (higher peak powers, where peak power is proportional to the pulse energy multiplied by the inverse of pulse duration). For each exposure time, there appears to be a threshold in peak power beyond which the size increases rapidly. This effect of peak power becomes less significant for exposure times of 1 ms with 2.1-nJ pulses.

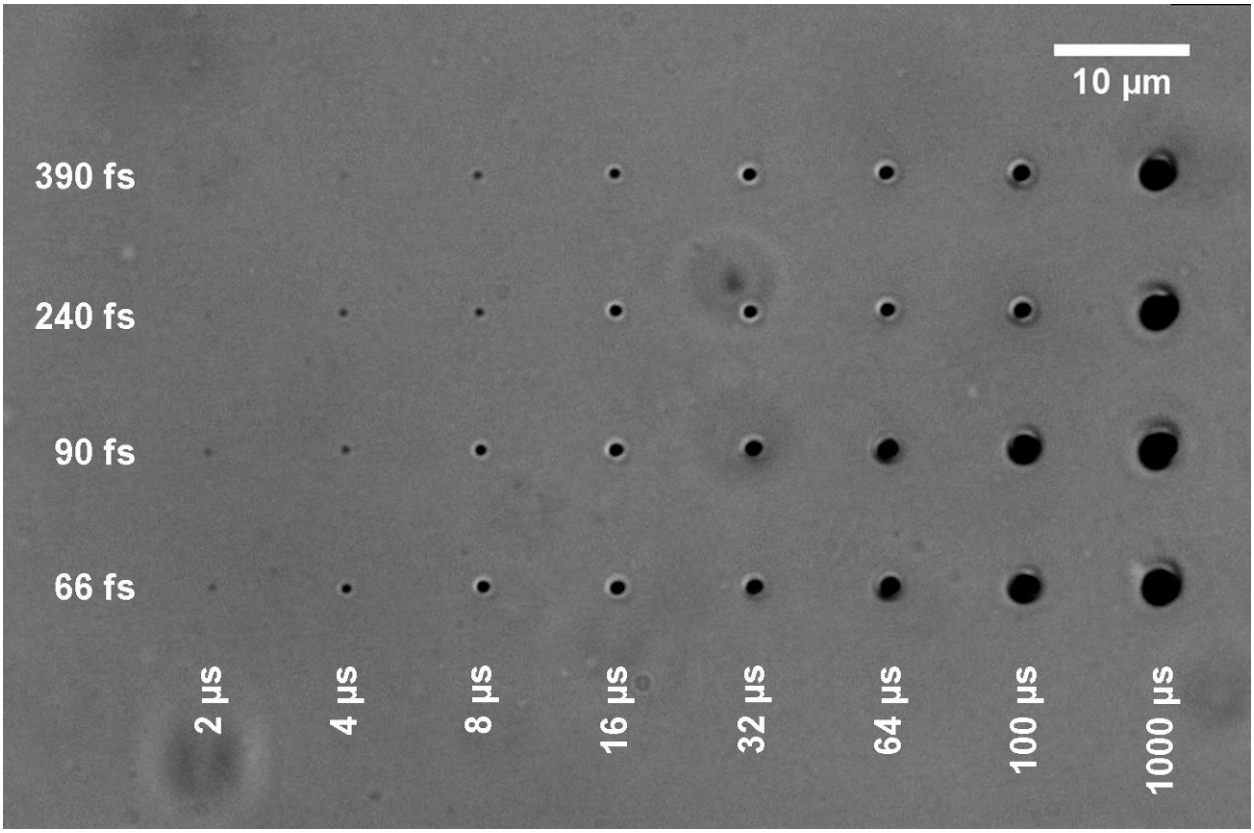

Figure 45: Optical image of silver dots fabricated with a pulse energy of 2.1 nJ. The laser exposure time is varied over the horizontal axis, and pulse duration is varied over the vertical axis.

We show the effect of laser peak power on particle volume for two exposure times in Figure 46 (we use particle volume instead of diameter for ease of visualization). We maintain the same pulse energy (2.2 nJ), calculate volume assuming spherical particles over 20 exposure spots, and represent the standard deviation using error bars. In both cases, low peak powers produce experimentally identical volumes that increase by over a factor of two with increasing peak power. This increase in volume occurs between 22–31 kW (τ_e = 16 µs) and between 8–22 kW for (τ_e = 64 µs), consistent with an exposure-dependent threshold. We note that a higher peak power (31 kW) produces the same particle size (1.2 µm in diameter) as a lower peak powers (8 kW) at four times

the rate (16 μs versus 64 μs exposure, respectively). This data shows that the peak power plays a role in silver particle growth for exposure durations less than 64 μs.

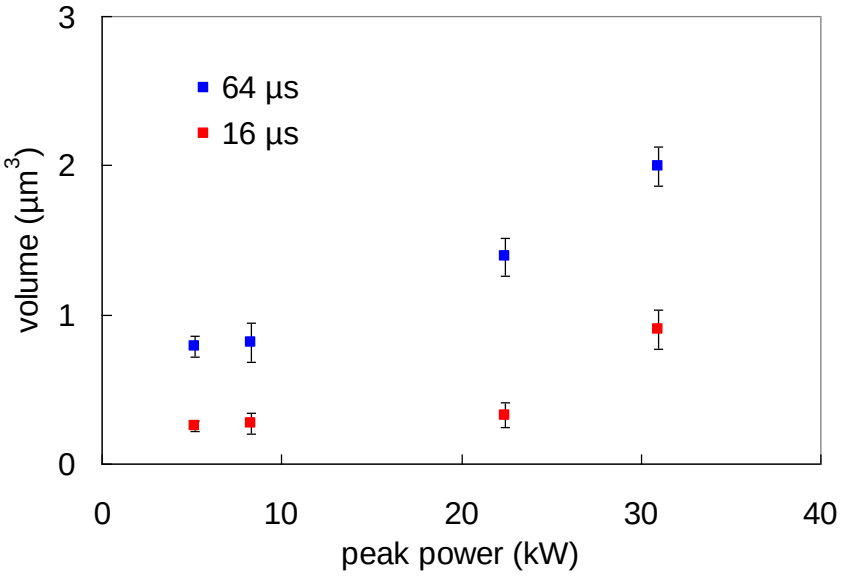

Figure 46: Silver particle volume as a function of peak power for exposure times of 16 and 64 μs. Pulse energy is set to 2.2 nJ.

From the correlation between higher peak-power and particle size, we infer that MPA can contribute to silver growth. For the case of purely LA growth, the particle size should scale with average power, which is proportional to pulse energy. For the case of MPA, the absorption coefficient becomes $\alpha(I) = \alpha_1 + \alpha_2 I + \alpha_3 I^2 + \ldots$, where α is the total absorption coefficient, α_1 is linear absorption, α_2 and α_3 are the two- and three-photon absorption coefficients (respectively), and I is the intensity. For low intensities, nonlinear absorption is negligible. For high intensities, MPA can become dominant, and manifests itself as an intensity-dependent threshold. We observe this threshold behavior in Figure 46, above which particle size increases rapidly with peak power. However, we are unable to determine the exact threshold due to the diffraction limit of our

microscope and limited laser bandwidth (a broader bandwidth allows shorter pulses, broadening the study of the effects of peak power).

Our experimental results give us insight into the mixed linear and nonlinear absorption process that is femtosecond laser writing. We hypothesize that silver growth begins primarily through nonlinear absorption creating seeds in the laser focal volume (NL growth). As silver particles grow larger, the contribution of LA growth increases. Beyond a critical volume of silver, LA growth dominates over NL growth. In the limit where the particle volume is much larger than the focal volume, we expect NL growth to be negligible compared to LA growth. The diffraction limit precludes us studying this purely NL growth regime; however, our pulse duration measurements show the effect of early seeding within the final micron-sized particles. In this situation, higher peak powers lead to earlier NL seeding that allows LA growth to begin faster, leading to larger particles. On the other hand, the effect appears to saturate with very long exposure times. Although our results elucidate one possible mechanism for femtosecond laser induced silver growth, these experiments cannot directly observe the NL growth regime.

The NL growth contribution to femtosecond laser writing is an important aspect for 3D patterning. For example, heating a mixture of dilute $AgNO_3$ and gelatin at 70ºC yields 10 nm particles after 48 hours throughout the sample [77]. To avoid widespread growth, we must locally deposit energy into a sample to restrict material modification inside the bulk of the material and obtain high axial resolution [2, 3, 13]. The NL growth contribution to laser writing ensures tight spatial control, and by using ultrashort laser pulses, we can grow silver with small energy doses that avoid nonlocal growth.

Our experiments show that controlling the optical energy deposition at femtosecond time scales has strong effects on silver growth. Higher peak power requires less irradiation time to achieve desired particle sizes. Thus, the NL growth contribution to nanoparticle size has important implications for scaling the silver writing process for manufacturing purposes.

Ultimately, further study is needed to elucidate the detailed dynamics of silver growth during femtosecond laser irradiations. NL growth may be a result of photochemical, photoionization, or photothermal processes due to MPA. Our approach cannot distinguish between these processes. These possibilities point to the importance of considering peak power during fabrication as a fourth variable to determine particle size, along with pulse energy, exposure time, and repetition rate. The peak power variable provides an additional degree of freedom to determine feature size and fabrication speed. To better understand the details of NL and LA growth contributions, studies using a combination of higher laser peak power, SEM imaging, pump-probe spectroscopy, and *Z*-scan measurements may provide important insight.

5.5 Summary

Femtosecond laser writing in silver-doped gelatin enables the fabrication of 3D metal patterns that can be disconnected in all three spatial dimensions. Here, we study the effect of laser exposure parameters on silver growth to improve control over the fabrication process. We show that, for constant dose, silver particle diameter increases with pulse energy. By varying laser pulse duty cycles, we also obtain results indicating heat diffusion occurs at a timescale on the order of 1 μs and that heat accumulations increases silver growth. Furthermore, by varying the laser pulse duration, we find that silver particle size increases for higher peak power (at constant pulse

energy); thus, we provide experimental evidence that MPA contributes to silver growth in the polymer matrix. These results establish that both linear and MPA contribute to silver growth during femtosecond laser irradiation in gelatin. By tuning the interplay between these mechanisms, we can achieve tighter control over particle size during fabrication. Although these results are obtained using $AgNO_3$ and gelatin, they may provide insights into metal growth mechanisms in alternate material systems.

We also demonstrate that silver growth is confined to a volume around the laser focus, and we can pattern multiple layers above each other. We create complex 3D silver patterns embedded inside gelatin. The broad range of 3D metal patterns produced is unmatched by any other nano- and micro-fabrication technique. By enabling new types of metal patterns, the method could lead to new experiments and applications in optics, metamaterials, and other fields of research.

5.6 Future work

Further experimentation is required to elucidate the complex growth mechanism during fabrication. Repeating the above experiments for full analysis under SEM imaging will yield insights into the dynamics at play for short exposure times and sub-diffraction growth. We expect the process to be highly complex; techniques such as pump probe spectroscopy will help detail growth dynamics with femtosecond and picosecond time resolution.

Chapter 6

Applications

Thus far, we have discussed several developments in femtosecond laser writing of silver in polymer for 2D and 3D fabrication. In this chapter, we discuss potential applications for the fabrication technique in optics. We discuss three areas of potential applications: 3D optical diffraction gratings, zone plates, and THz metamaterials.

6.1 Optical diffraction gratings

This section covers research reported in: M. Moebius,* K. Vora,* P. Munoz, G. Deng, S. Kang, and E. Mazur (*co-first authors), "3D optical diffraction gratings and zone plates in gelatin," *Manuscript in preparation*, 2014.

Similar to x-ray scattering and electron diffraction (using transmission electron microscopy) of crystals, arrays of optical scatterers can lead to Bragg scattering peaks when illuminated with light. Diffraction angles and intensities are functions of material indices and lattice structures. Optical diffraction is frequently used to assess the quality of photonic crystals [83, 84] [85]. Recent work by Brüser et al. [83] extends the range of 3D patterns that can be used to create 3D optical diffraction devices in the high-energy range [85-87], where the lattice constant is equal to or greater than incident wavelength, through TPP.

However, TPP cannot create patterns of disconnected scatterers in 3D, such as a simple 3D cubic lattice. 3D femtosecond laser writing of silver inside gelatin can readily produce such patterns in a single fabrication step. In this section, we demonstrate examples of 3D lattices and their measured optical diffraction patterns.

6.1.1 Fabrication

We prepare substrates with 250-μm thick Ag-doped gelatin films using methods described in Section 4.2.1. Fabrication takes place using 66-fs pulses from an 11-MHz repetition rate laser centered at 795 nm. A high-precision 3-axis stage and AOM combination controls the position and exposure of laser pulses inside the sample. MPA induces the growth of silver structures inside a laser focal volume.

We fabricate simple cubic and body-centered cubic (BCC) crystals of silver particles. The spacing between scatterers ranges between 10 and 20 μm in the *x*-, *y*-, and *z*-directions. The average silver scatterer is approximately 1 μm in diameter. The total crystal size in the horizontal plane is 4 mm by 4 mm. We choose these dimensions to easily observe a large number of diffraction orders on a screen. 3D arrays are composed of 2 to 12 layers. We use a stage translation velocity of 250 μm/s, and exposure of 500 μs at 18 mW to produce scattering elements in cubic and 1-atom BCC lattices. For 2-atom BCC crystals, mimicking a 2-atom crystallographic lattice, we use 2 different doses (500 and 1000 μs) to create scatterers of two different diameters: 1 μm and 2.5 μm.

6.1.2 Measurements

We measure optical diffraction with a 633-nm HeNe laser at incidence angles between -60 and 60 degrees. The laser beam diameter is 700 µm. Diffraction patterns were captured by a camera on a screen. Figure 47 shows a schematic of the measurement setup. A beam block is placed in the center of the screen to block the 0^{th} order beam. The 0^{th} order beam is blocked due to its high intensity that saturates the camera.

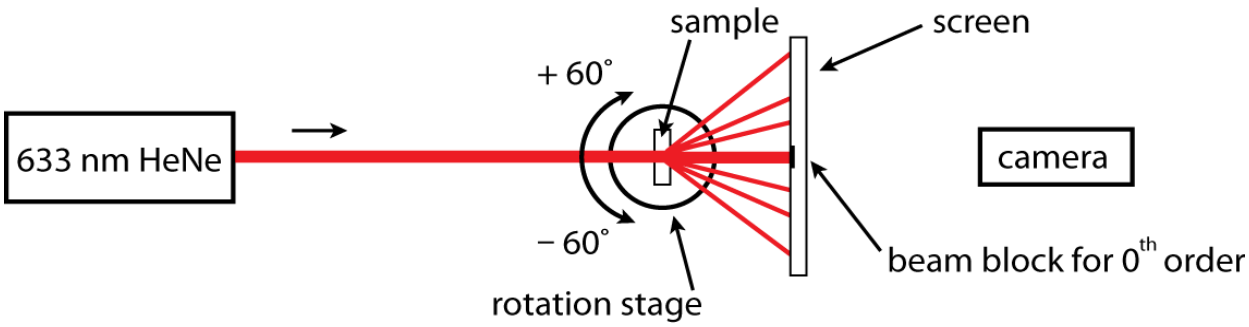

Figure 47: Optical setup for measuring optical diffraction grating patterns.

6.1.3 Results and discussion

The measured diffraction pattern for multilayered patterns is more complex than patterns obtained from simple 2D lattices due to interference of light scattered by different layers. For comparison purposes, Figure 48 shows calculated diffraction patterns for a 1-layer square array of scatterers, as well as 4- and 12-layer cubic arrays. The patterns are obtained with a MATLAB script that calculates far-field interference from an array of spherical scatterers. The incident radiation wavelength is set to 633 nm, and the beam diameter is 700 µm. Even though our experimental

samples consist of large ellipsoidal Mie scatterers, the calculations provide a first order approximation for features to expect in the measured diffraction patterns.

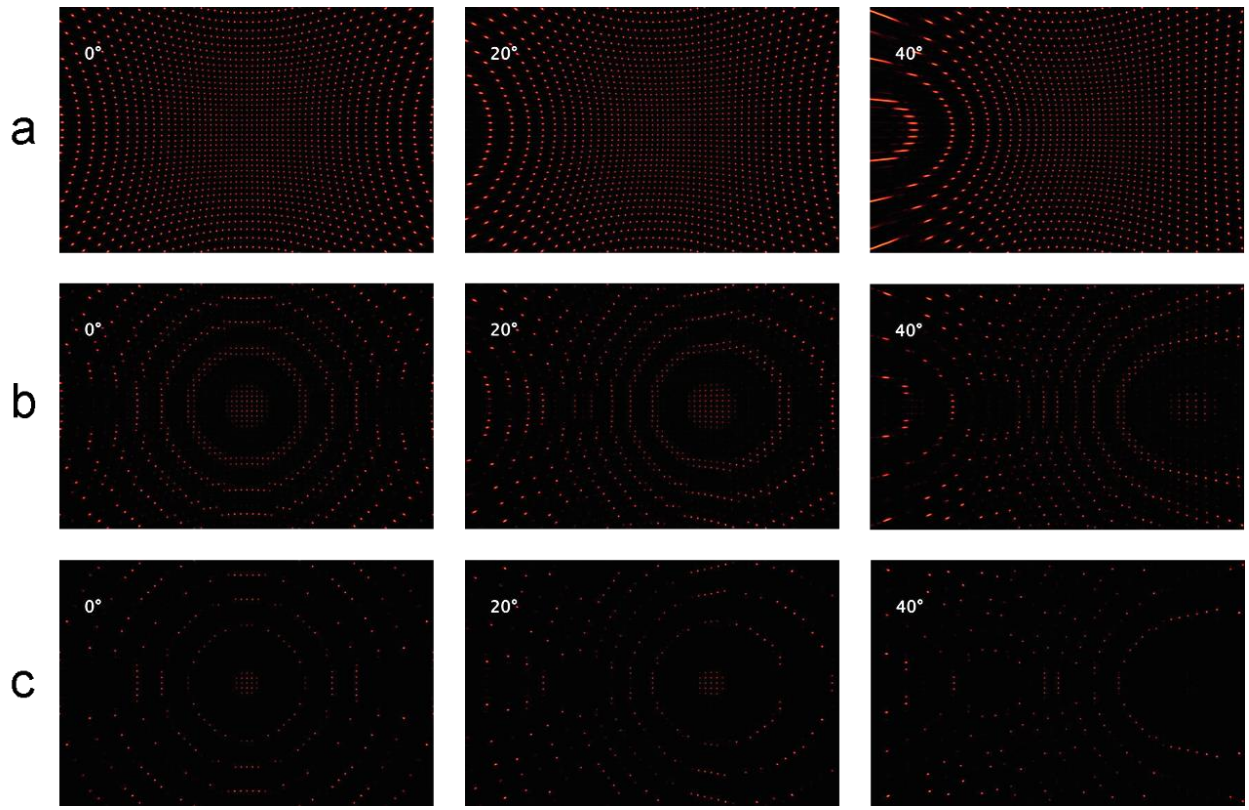

Figure 48: Calculated optical diffraction grating patterns for (a) 1-layer, (b) 4-layer, and (c) 12-layer cubic lattices.

In the 1-layer calculation versus 4-layer and 12-layer calculations, we note the presence of empty rings where no diffraction maxima are visible. This feature is characteristic of the 3D nature of the lattice and can be explained through the Ewald construction in reciprocal space. Thus, for a defined incident beam on 3D crystal lattices, different orders of diffraction meet the conditions for constructive interference at specific ranges of angles, resulting in rings in the observed diffraction patterns. As the number of layers in the crystal increases, the width of these empty rings increases in real-space.

We measure diffraction patterns from samples with 2 to 12 layers. Figure 49 shows representative optical images of diffraction patterns for 10-layer and 12-layer cubic lattices at 0, 20, and 40 degrees, and Figure 50 shows similar results for 10-layer, 2-atom and 1-atom BCC lattices. Several diffraction orders from the 3D lattices are visible on the screen.

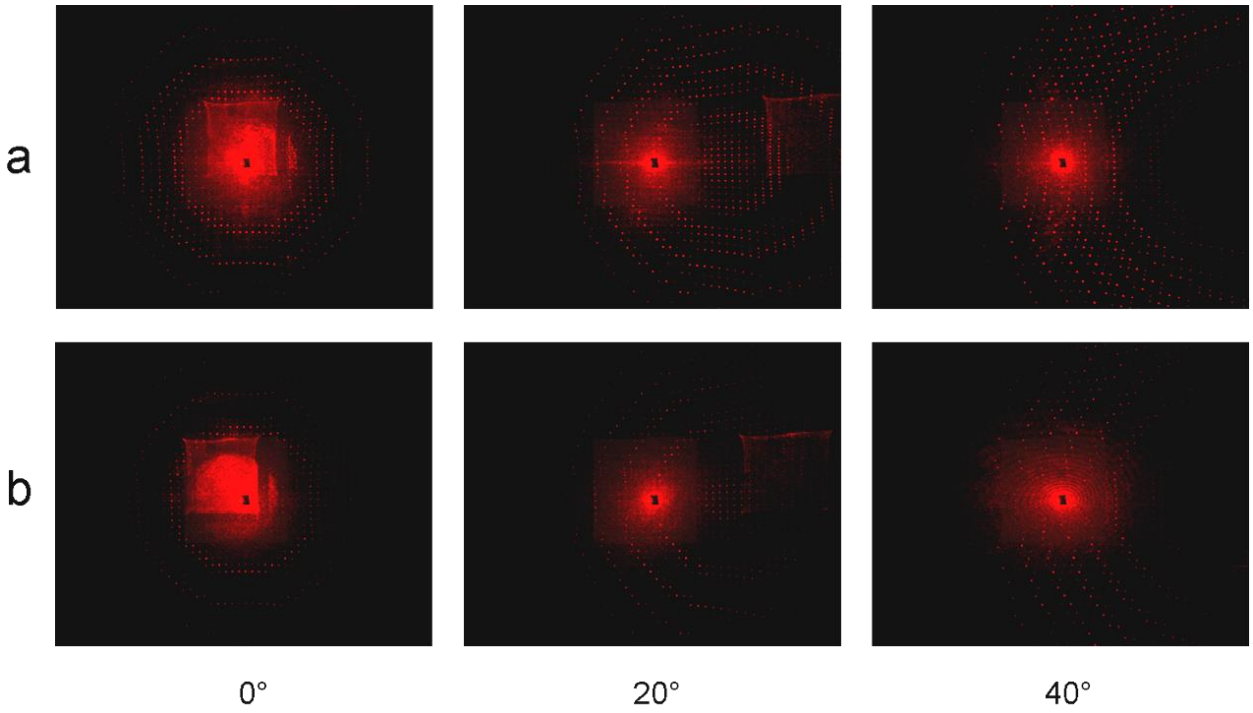

Figure 49: Optical images of diffraction patterns from (a) 10-layer and (b) 12-layer cubic lattices. Images are taken with 0, 20, and 40° angles between the laser and sample. An identical contrast enhancement was applied to all images to improve visibility of intensity maxima. Note that scattering from the zero order beam and a projection of the sample substrate reduces the signal-to-noise near the center of the image.

In Figure 49, the cubic diffraction patterns for 10- and 12-layer structures have similarly positioned intensity maxima. However, we note a difference between diffraction orders: the 12-layer has slightly narrower bands of diffraction orders. This difference becomes more evident at higher sample angles. This behavior is expected for crystals with increasing thickness (more specifically, increasing number of layers).

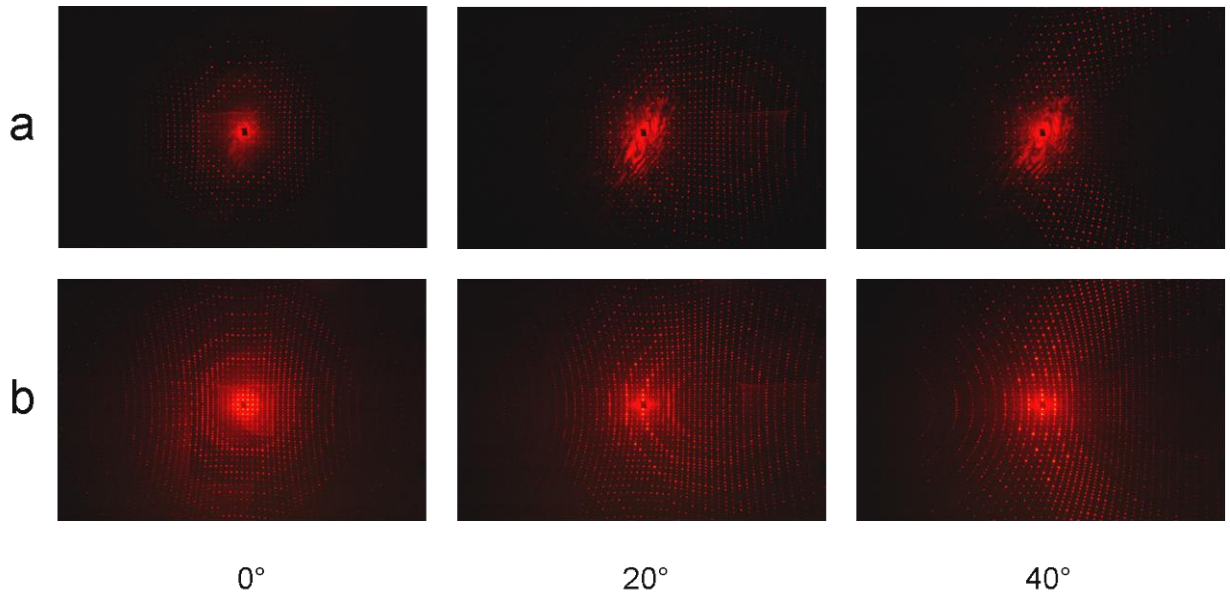

Figure 50: Optical images of diffraction patterns from (a) 1-atom and (b) 2-atom BCC lattices with 10-layers. Images are taken with 0, 20, and 40° angles between the laser and sample. Note that scattering from the zero order beam and a projection of the sample substrate reduces the signal-to-noise near the center of the image.

For the 2-atom BCC lattice Figure 50, we observe greater intensity variations compared to the 1-atom system. This is due to the differently-sized scatterers having different scattering cross-sections. The constructive and destructive interference conditions change as a result of the difference in scattering cross-section. As shown in Chapter 3 and Chapter 4, silver dot sizes can range from 100 nm to several micrometers in size. Thus, by tuning size, it is possible to alter the scattering properties of the unit cells to obtain desired effects.

In Figure 49 and Figure 50, the presence of bands of diffraction orders similar to those in the calculated patterns indicate multiple layers in the sample. However, there are several differences between the measured and calculated diffraction patterns. These discrepancies are expected due to several approximations in the calculations, as well as non-idealities in the fabricated structures. For example, the MATLAB script assumes that light is only scattered once

by lattice points and that there is no angular dependence. For the fabricated structures, we expect multiple scattering events [83]. We also expect shadowing effects due to absorption in silver (as well as a small amount of linear absorption in the polymer) to affect constructive and destructive interference between scattered waves. An improved fit between experimental and calculated values may be obtained by modifying the MATLAB model to include Mie scatterers, and fabricating silver dots with lower scattering cross-sections.

6.1.4 Summary and future work

We demonstrate the fabrication of 3D arrays of silver dots for optical diffraction experiments; the measured diffraction patterns confirm that the lattices are 3D. Through modifications of the fabrication parameters, it may be possible to create optical analogues of electron diffraction patterns found through transmission electron microscopy.

Recent work by Brüser et al. extends the range of patterns that can be created for 3D optical diffraction through TPP [83]. However, TPP cannot create patterns of disconnected scatterers in 3D, such as a simple 3D cubic lattice. The 3D fabrication of silver inside polymer complements the range of 3D devices that can be created by TPP for optical diffraction applications. In this section, we demonstrate examples of 3D lattices and show their measured optical diffraction patterns.

Optical diffraction patterns may also be used to characterize the 3D fabrication process itself. Diffraction can be used to determine the quality of 3D optical lattices [83-85], and determine fabrication limits for feature size and resolution in TPP [88]. The technique is especially valuable for extracting the physical properties of high resolution 3D patterns since SEM does not provide

structural information on the bulk of volumetric samples. The analysis of diffraction patterns from 3D arrays of silver dots may provide insights into resolution and feature size when optical imaging is insufficient. Such characterization is critical for applications such as optical metamaterials.

6.2 Zone plates

This section covers research reported in: M. Moebius,* K. Vora,* P. Munoz, G. Deng, S. Kang, and E. Mazur (*co-first authors), "3D optical diffraction gratings and zone plates in gelatin," *Manuscript in preparation*, 2014.

Lenses are typically made from refractive optical elements. However, it is possible to focus light through diffractive elements such as zone plates. Zone plates are composed of a series of concentric annular apertures that alternate between opaque and transparent. Each of these rings is called a Fresnel zone. Light is diffracted by opaque zones and interferes constructively at the designed focus position. Zone plates are technologically interesting because they are planar elements and display a high amount of dispersion. Zone plates and arrays of zone plates have been used for applications in dispersion [89], maskless optical lithography [90], and parallelized fluorescence imaging [91].

In this section, we describe the fabrication of zone plates using femtosecond laser writing of silver in gelatin. We test the devices in a transmission optical microscope using an LED light source. To showcase the laser fabrication capabilities, we create multi-layer arrays of zone plates with varying distances over the *z*-axis that would be very difficult to pattern using electron beam lithography. These types of structures may be useful for imaging, telescoping, and 3D integrated optics.

6.2.1 Design and fabrication

We design zone plates to focus 633 nm light at distances ranging from 4 μm to 50 μm (in free space) above the sample. The inner and outer radii of each zone is calculated through

$$r_n = \sqrt{n\lambda f + \frac{n^2\lambda^2}{4}}, \tag{6.1}$$

where r is the radius, n is an integer, λ is the wavelength, and f is the focal length.

We fabricate zone plates with 5 opaque rings. They are patterned through continuous irradiation of the doped gelatin (see Chapter 4) at laser powers ranging between 3 and 15 mW, and translation speeds between 5 and 250 μm/s.

6.2.2 Results

We test the zone plates in a transmission optical microscope using a white LED light source. The spectrum of the light source is shown in Figure 51. All the zone plates are designed for a wavelength of 633 nm. We expect red-shifted wavelengths to experience focusing at shorter distances, and blue-shifted wavelengths to experience focusing at longer distances.

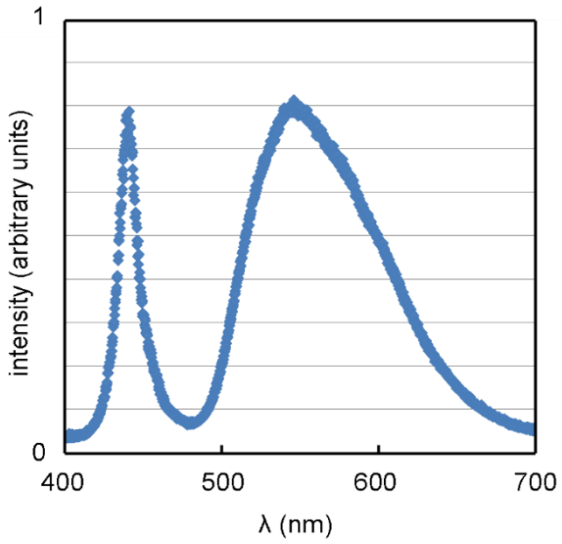

Figure 51: Spectrum of LED light source focused by the zone plate.

Figure 52 shows representative optical microscopy images of zone plates designed with a 50 µm focal distance. The zone plates are in clear focus in Figure 52a. We translate the sample away from the microscope the focal plane (over the *z*-axis) by a distance of 50, 60, and 70 µm, shown in Figure 52b, Figure 52c, and Figure 52d, respectively. The images show focused illumination spots from the LED light source at each distance. We expect the color of the focus spots to be centered at approximately 633 nm, 550 nm, and 450 nm for each of these distances (a blue-shift with increasing distance).

The broad spectral nature of the illumination and saturation in the camera sensor make it difficult to distinguish colors in Figure 52b and Figure 52c. However, we observe a blue-shift in the color of the focal spots at 60 µm compared with 50 µm. The blue-shift becomes most clear at a distance of 70 µm (Figure 52d), where we expect to see focused light centered at 450 nm. The blue color of the focal spot is clearly distinguishable in Figure 52d due to an emission peak of the illumination spectrum at a corresponding wavelength. We also use long-pass (550 nm) and short-pass (500 nm) filters to isolate specific wavelength ranges during imaging to confirm the presence

of expected colors at different focal distances. The application of a 550 nm long-pass filter leads to a bright focal spot at 50 µm and the application of a 500 nm short-pass filter leads to a bright focal spot at 72 µm. These results closely match the expected focusing of 633 nm and 450 nm light, respectively.

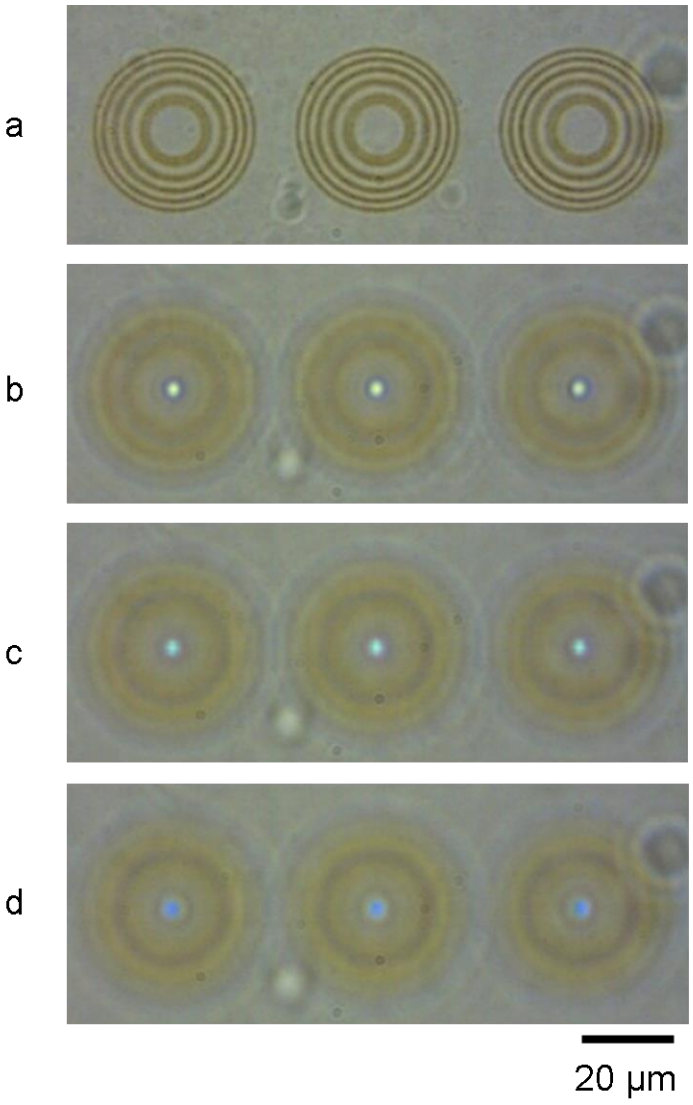

Figure 52: Zone plates viewed under an optical microscope. The sample is position such that the zone plates are (a) 0 µm, (b) 50 µm, (c) 60 µm, and (d) 70 µm away from the focal plane of the microscope. Light from an LED illumination source is focused by the zone plates.

These zone plates, although functional, do not provide new experimental capabilities that cannot be achieved using alternate fabrication techniques. For example, we also pattern zone plates with identical design parameters using electron beam lithography and metal deposition that yield similar results to those obtained with the laser patterned samples. However, the devices validate the use of femtosecond laser fabrication of silver for applications in diffractive optics. One advantage of laser fabrication is that structures can be arbitrarily oriented. Another advantage is the ability to pattern multilayered devices. For example, parallel zone plates in multiple layers could be used to create multi-element lenses or telescopes.

We create a sample 3D pattern of zone plates that cannot be readily achieved with alternate techniques: an array of 80 zone plates distributed over 2 layers. The first layer contains 40 identical zone plates. Below each of these is a second parallel zone plate. Each vertical pair has a unique separation distance that ranges from 2.5 μm to 22 μm. Figure 53 shows in-situ optical microscopy images of a portion of the array.

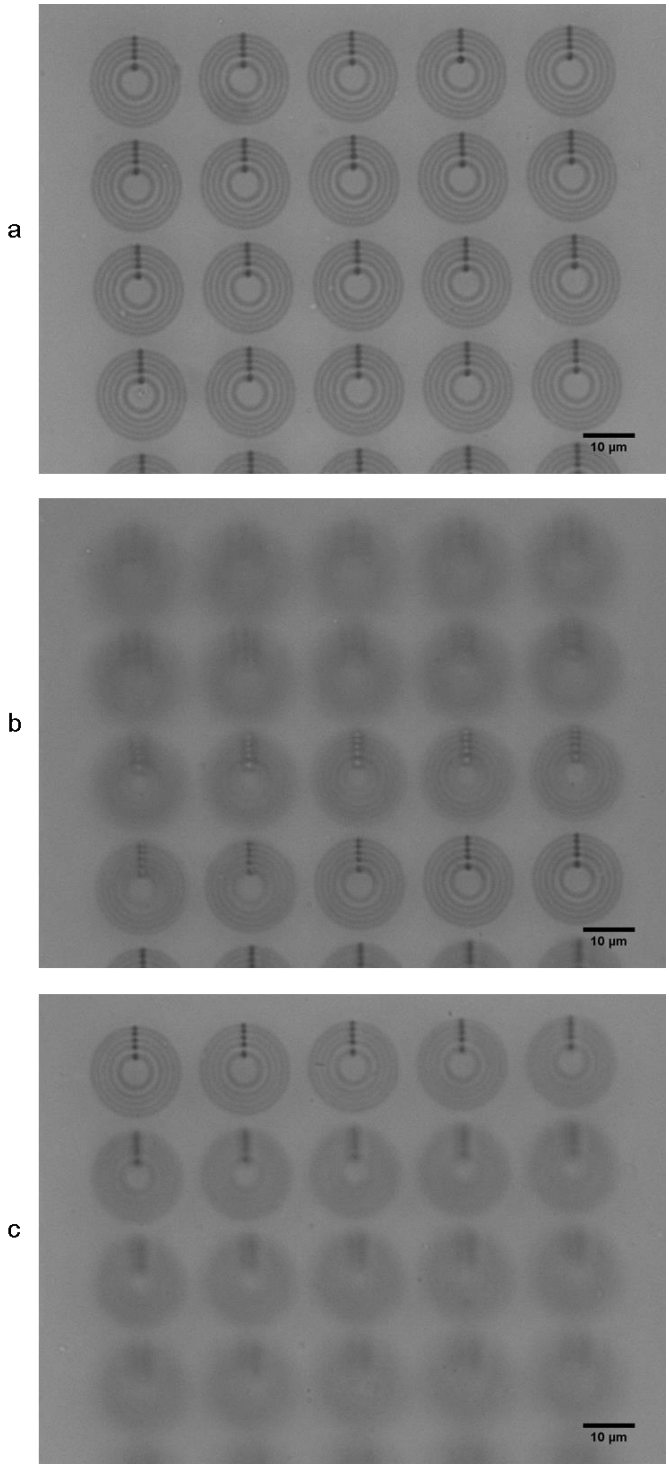

Figure 53: Optical microscopy images of multilayer zone plate array. The microscope focus is positioned (a) 0 µm, (b) 12.5 µm, and (c) 22 µm below the upper layer of zone plates along the *z*-axis.

Figure 53a shows 20 zone plates patterned in the top layer. Figure 53b shows an image where the focus is shifted below by 12.5 μm, and Figure 53c shows an image where the focus is shifted below by 22 μm. (The defects in each zone plate are caused by an additional laser dwell time during the writing process and can be corrected.) This type of multilayer structure is very difficult to achieve using standard nanofabrication tools due to varying zone plate pair separations.

6.2.3 Summary

In this section, we demonstrate functional 2D zone plates fabricated with femtosecond laser writing of silver in gelatin. They are tested using a white LED illumination source and show expected behavior: focused light becomes blue-shifted with increasing focal distance.

We create multi-layer arrays of zone plates with varying distances over the *z*-axis that would be very difficult to pattern using electron beam lithography. Although we limit patterns to pairs of zone plates, it is possible to create larger arrays with arbitrary orientations.

6.3 Metamaterials

The burgeoning field of metamaterials has seen many ground-breaking advances in recent years, from negative refraction to invisibility cloaks. However, the practical application of certain metamaterials designs is hampered by the difficulty in patterning metals in three dimensions [1]. The 3D fabrication method presented in this thesis may help overcome some of these practical limitations.

In Figure 34 of Chapter 4, we show that the doped-gelatin material has two prominent transparency windows: the optical and THz regimes. Thus, it is possible to create metamaterials

for those two regions of the electromagnetic spectrum through careful design. We focus on two designs for silver rings operating in the THz regime, and based on work by Xu Zhang of Durdu Guney's group at Michigan Technological University. Both designs were tested through simulations of silver structures inside gelatin.

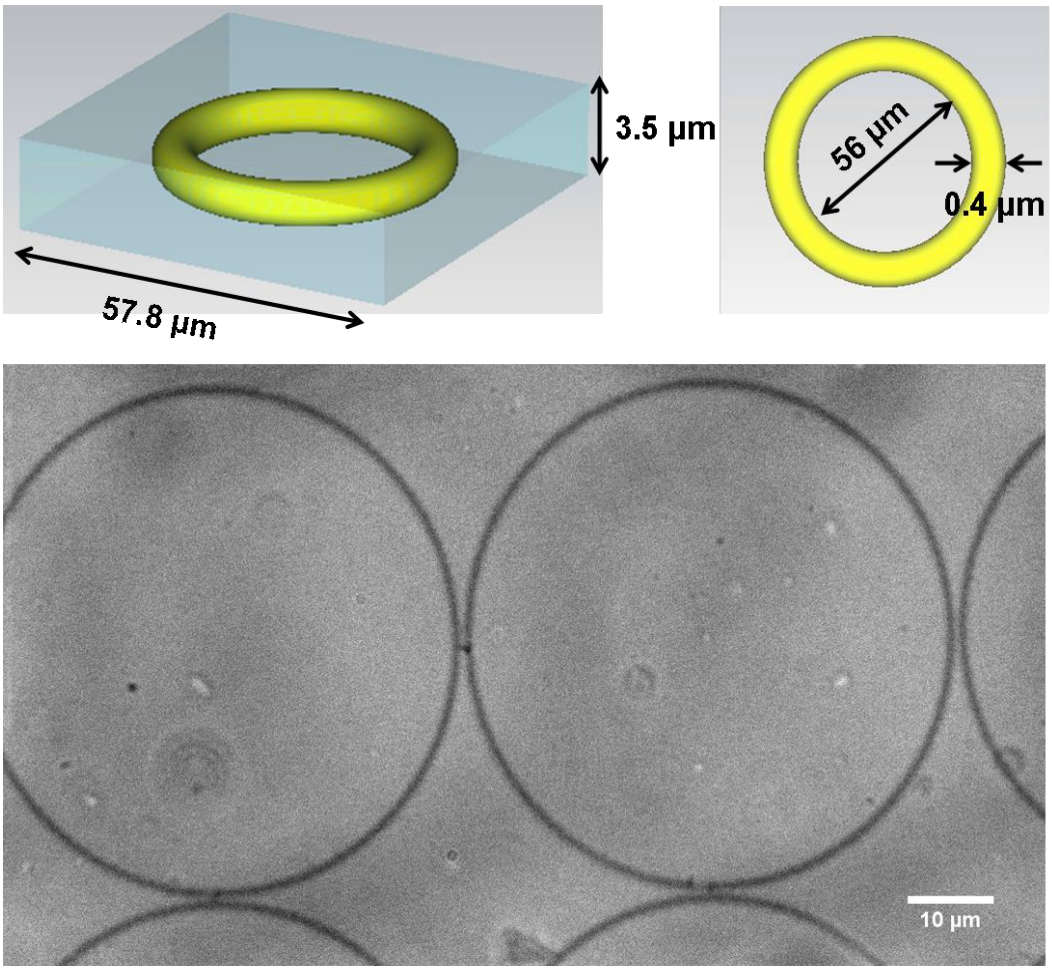

Figure 54: Schematic of a metamaterial design with 56-µm diameter silver rings that exhibits negative permittivity at a wavelength of 400 µm (image courtesy of Xu Zhang), and optical image of the fabricated structure.

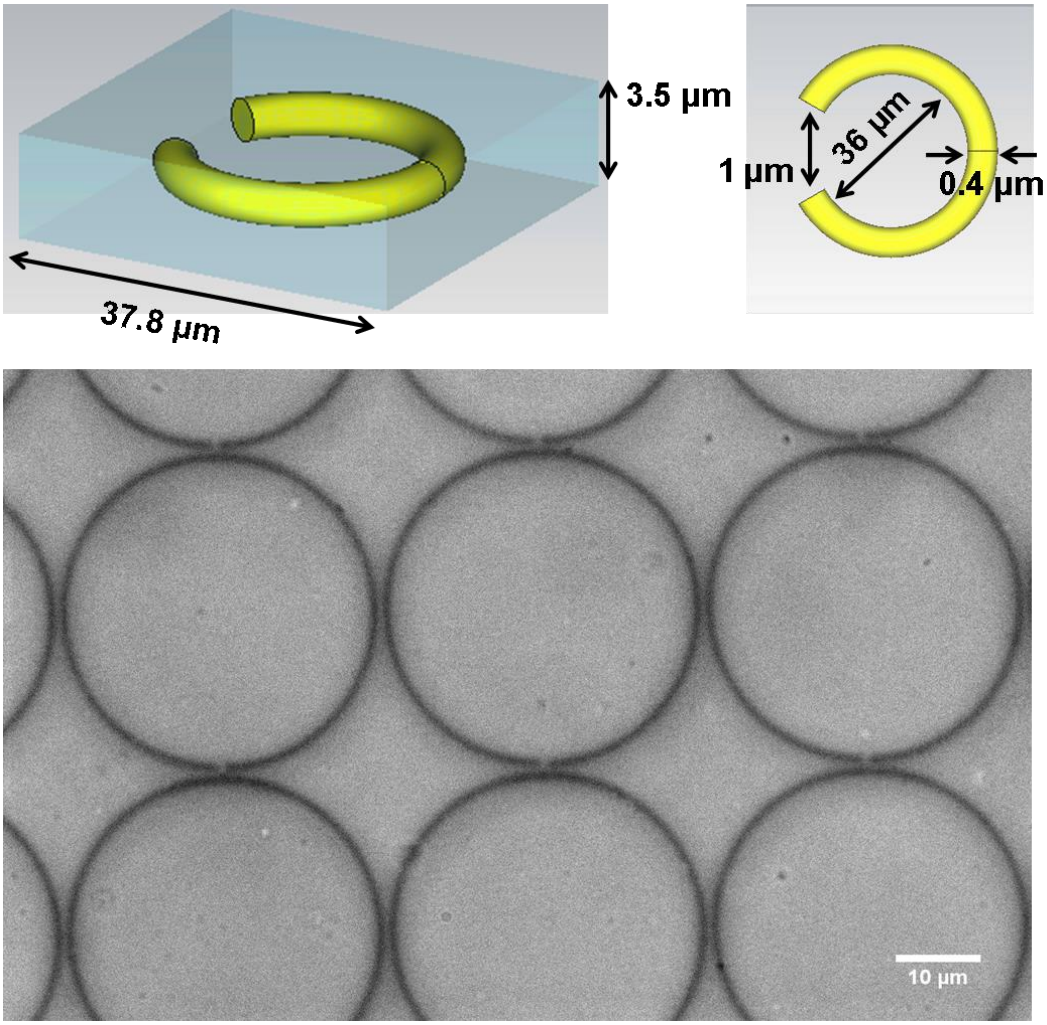

Figure 55: Schematic of a metamaterial design with 36-µm diameter silver split rings that exhibits negative permittivity at a wavelength of 400 µm (image courtesy of Xu Zhang), and optical image of the fabricated structure.

Figure 54 and Figure 55 show the pattern design parameters and optical images of fabricated structures. Both designs are expected to exhibit negative electrical permittivity in the THz transmission window of the gelatin material (at $\lambda = 400$ µm). The patterns were fabricated in 3D arrays with 10 to 20 layers in the vertical dimension, spanning 5 mm by 5 mm over the lateral dimensions. The designs require sub-micrometer linewidth over mesoscopic to macroscopic length scales. The laser technique is readily able to accommodate these requirements through a careful

choice of laser parameters (continuous irradiation with 0.3 nJ pulses at 11 MHz with a sample translation velocity of 100 μm/s). We demonstrate the ability to fabricate structures that may be useful for metamaterial applications.

Creating functional metamaterials will require an iterative process between design and fabrication. The original designs created by Guney et al. assume standard optical properties for silver. However, we expect the true optical properties of fabricated silver to differ from these values. Maruo et al. found that the DC electrical conductivity of silver fabricated in PVP was an order of magnitude lower than for bulk silver [8]; we can infer that the optical properties of their silver also deviated from standard values. Similarly, we expect there will be a difference in optical properties for our material. Standard techniques such as thin film variable angle spectroscopic ellipsometry cannot be used to obtain the optical properties of our silver material since we do not grow uniform films. A combination of Fourier transform infrared spectroscopy or THz time-domain spectroscopy with effective medium theory may provide the required data.

6.4 Summary

We discuss potential applications of the 3D fabrication technique to diffraction optics and metamaterials. We show preliminary fabrication results based on several designs. Characterization and optimization steps are necessary before creating functional devices. We demonstrate the first steps towards practical use of the laser technique in device applications. Additional applications may include 3D microelectronic circuits, plasmonics, and sensing.

Chapter 7

Summary and outlook

This dissertation describes methodology that significantly improves the state of femtosecond laser writing of metals. The developments address two major shortcomings: poor material quality, and limited 3D patterning capabilities. In two dimensions, we grow monocrystalline silver prisms through femtosecond laser irradiation. We thus demonstrate the ability to create high quality material (with limited number of domains), unlike published reports of 2D structures composed of nanoparticle aggregates. This development has broader implications beyond metal writing, as it demonstrates a one-step fabrication process to localize bottom-up growth of high quality monocrystalline material on a substrate. In three dimensions, we direct laser write fully disconnected 3D silver structures in a polymer matrix. Since the silver structures are embedded in a stable matrix, they are not required to be self-supported, enabling the one-step fabrication of multiple disconnected layers of metal patterns. This latter development addresses a broader limitation of fabrication technologies, where 3D patterning of 3D metal structures is difficult. Several of the demonstrated 3D silver patterns cannot be obtained through any other fabrication technique known to us. We expect these advances to contribute to developments of new devices in optics, plasmonics, and metamaterials [1, 40]. With further improvements in these fabrication

methods, the list of potential applications broadens to include electronics (e.g. 3D microelectronic circuits), chemistry (e.g. catalysis), and biology (e.g. plasmonic biosensing).

Although a handful of reports demonstrate 3D silver fabrication using irradiation from femtosecond pulses [2, 6-8, 10], a detailed understanding of the silver growth process has not been studied experimentally. Compared to TPP [3, 20], femtosecond laser metal writing is complicated by the fact that the material grown through the irradiation process is not transparent and absorbs light linearly, leading to additional thermally-driven growth. We study the effect of laser exposure on silver particle diameter in gelatin. We observe the size dependence as a function of laser-pulse energy and number of pulses. We further investigate silver growth by varying the pulse spacing and pulse duration. By varying the duty cycle (pulse spacing), we show that heat accumulation accelerates growth and leads to larger silver particles with a timescale for heat diffusion on the order of 1 μs. Furthermore, by varying the laser pulse duration, we find that silver particle size increases for higher peak power (at constant pulse energy); thus, we provide experimental evidence of nonlinear absorption-induced silver growth in the polymer matrix. These results suggest that both linear and nonlinear absorption are involved during femtosecond laser writing of silver and imply that by tuning these mechanisms, we can achieve tighter control over particle size during 3D fabrication. Our work establishes the groundwork for further studies of femtosecond laser induced silver growth mechanisms. An improved understanding of the fabrication process is important for scaling the technique for manufacturing purposes.

7.1 Future directions

The future directions can be separated into two categories: developments of the fabrication technique, and applications.

Further experimentation is required to elucidate the complex growth mechanism during fabrication. A combination of pump-probe spectroscopy, z-scan measurements, and SEM imaging will help reveal detailed growth dynamics. Determining the interplay between photochemical and photothermal processes during growth will provide greater fabrication control.

The appropriate combination of solvents, metal salts, and polymers is important to obtain a stable background medium without limiting growth during laser irradiation. Exploring the chemical composition of samples may further improve performance for sample lifetime, resolution, laser damage threshold, flexibility, or transparency spectrum. The use of gelatin instead of PVP, for example, improved sample lifetime, reduced scattering defects, and increased sample thickness. Further optimization of the background material may be important for scalable fabrication. As another example, the addition of ethanol to the mixture of PVP and $AgNO_3$ yielded the production of high quality crystals in 2D. Careful control of the reagents and laser parameters may improve control over the shapes of nanoparticles during laser growth.

We primarily limit our laser fabrication to silver. However, it is possible to grow other metals, such as gold and copper, through femtosecond laser irradiation [12, 92]. Expanding the range of materials for patterning will also expand potential applications. Recent results have shown that femtosecond pulses centered at 400-nm can induce localized reactions to create core-shell

nanoparticles inside a polymer [92]. It may be possible to extend the fabrication methods beyond metals to include semiconductors.

Several demonstrated patterns through 3D fabrication cannot be realized, to the best of our knowledge, through any other fabrication technique. As seen in Chapter 6, the current state of the laser technique is already suitable for applications in diffraction optics, for example. Careful design, fabrication, and characterization will enable devices that were not previously technologically feasible. For example, a combination of novel design with laser fabrication will lead to bulk 3D metamaterials in the near future. As the fabrication methods for 2D and 3D laser writing are improved, applications will broaden to include electronics (e.g. 3D microelectronic circuits), chemistry (e.g. catalysis), and biology (e.g. plasmonic biosensing).

On a broader scope, the 3D fabrication technique demonstrates the creation of nanocomposite materials where we control the position of nanostructures through laser irradiation. Such materials can have engineered electrical, optical, and mechanical properties [92]. Thus, further exploring the interaction between femtosecond laser pulses and chemical reagents is an important avenue for material design.

Bibliography

[1] D. Ö. Güney, T. Koschny, C. M. Soukoulis, Opt. Express **18**, 12348 (2010).

[2] C. N. LaFratta, J. T. Fourkas, T. Baldacchini, R. A. Farrer, Angewandte Chemie International Edition **46**, 6238 (2007).

[3] G. von Freymann, A. Ledermann, M. Thiel, I. Staude, S. Essig, K. Busch, M. Wegener, Advanced Functional Materials **20**, 1038 (2010).

[4] J. K. Gansel, M. Thiel, M. S. Rill, M. Decker, K. Bade, V. Saile, G. von Freymann, S. Linden, M. Wegener, Science **325**, 1513 (2009).

[5] M. S. Rill, C. Plet, M. Thiel, I. Staude, G. von Freymann, S. Linden, M. Wegener, Nat Mater **7**, 543 (2008).

[6] Y.-Y. Cao, N. Takeyasu, T. Tanaka, X.-M. Duan, S. Kawata, Small **5**, 1144 (2009).

[7] Y.-Y. Cao, X.-Z. Dong, N. Takeyasu, T. Tanaka, Z.-S. Zhao, X.-M. Duan, S. Kawata, Applied Physics A: Materials Science & Processing **96**, 453 (2009).

[8] S. Maruo, T. Saeki, Opt. Express **16**, 1174 (2008).

[9] T. Tanaka, A. Ishikawa, S. Kawata, Appl Phys Lett **88**, 081107 (2006).

[10] A. Ishikawa, T. Tanaka, S. Kawata, Appl Phys Lett **89**, 113102 (2006).

[11] T. Baldacchini, A.-C. Pons, J. Pons, C. LaFratta, J. Fourkas, Y. Sun, M. Naughton, Opt. Express **13**, 1275 (2005).

[12] F. Stellacci, C. A. Bauer, T. Meyer-Friedrichsen, W. Wenseleers, V. Alain, S. M. Kuebler, S. J. K. Pond, Y. Zhang, S. R. Marder, J. W. Perry, Advanced Materials **14**, 194 (2002).

[13] R. R. Gattass, E. Mazur, Nat Photon **2**, 219 (2008).

[14] B. Y. Ahn, S. B. Walker, S. C. Slimmer, A. Russo, A. Gupta, S. Kranz, E. B. Duoss, T. F. Malkowski, J. A. Lewis, e3189 (2011).

[15] L. M. Tong, R. R. Gattass, I. Maxwell, J. B. Ashcom, E. Mazur, Optics Communications **259**, 626 (2006).

[16] E. N. Glezer, E. Mazur, Applied Physics Letters **71**, 882 (1997).

[17] E. N. Glezer, M. Milosavljevic, L. Huang, R. J. Finlay, T. H. Her, J. P. Callan, E. Mazur, Optics Letters **21**, 2023 (1996).

[18] C. R. Mendonca, T. Baldacchini, P. Tayalia, E. Mazur, Journal of Applied Physics **102**, 4 (2007).

[19] C. R. Mendonca, D. S. Correa, T. Baldacchini, P. Tayalia, E. Mazur, Applied Physics a-Materials Science & Processing **90**, 633 (2008).

[20] T. Baldacchini, S. Snider, R. Zadoyan, Opt Express **20**, 29890 (2012).

[21] M. Goppert-Mayer, Ann Phys-Berlin **9**, 273 (1931).

[22] R. W. Boyd, *Nonlinear Optics*, 3rd ed. (Academic Press, Boston, 2008).

[23] P. Tayalia, Ph.D. thesis, Harvard University, 2009.

[24] V. N. Sigaev, V. I. Savinkov, S. V. Lotarev, G. Y. Shakhgildyan, R. Lorenzi, A. Paleari, Nanotechnology **24**, (2013).

[25] T. S. Taberner, A. Martin-Villodre, J. M. Pla-Delfina, J. V. Herraez, Int J Pharm **233**, 43 (2002).

[26] C. Altucci, A. Nebbioso, R. Benedetti, R. Esposito, V. Carafa, M. Conte, M. Micciarelli, L. Altucci, R. Velotta, Laser Phys Lett **9**, 234 (2012).

[27] M. Yoshida, P. N. Prasad, Appl Optics **35**, 1500 (1996).

[28] M. T. Raimondi, S. M. Eaton, M. M. Nava, M. Lagana, G. Cerullo, R. Osellame, J Appl Biomater Func **10**, 56 (2012).

[29] E. D. Diebold, N. H. Mack, S. K. Doom, E. Mazur, Langmuir **25**, 1790 (2009).

[30] P. D. Nallathamby, K. J. Lee, X. H. N. Xu, Acs Nano **2**, 1371 (2008).

[31] F. Mafune, J. Kohno, Y. Takeda, T. Kondow, H. Sawabe, J Phys Chem B **104**, 8333 (2000).

[32] A. Pal, S. Shah, S. Devi, Mater Chem Phys **114**, 530 (2009).

[33] C. M. Gonzalez, Y. Liu, J. C. Scaiano, J Phys Chem C **113**, 11861 (2009).

[34] R. A. Salkar, P. Jeevanandam, S. T. Aruna, Y. Koltypin, A. Gedanken, J Mater Chem **9**, 1333 (1999).

[35] M. Starowicz, B. Stypula, J. Banas, Electrochem Commun **8**, 227 (2006).

[36] J. H. Zhang, H. Y. Liu, P. Zhan, Z. L. Wang, N. B. Ming, Advanced Functional Materials **17**, 1558 (2007).

[37] Y. G. Sun, Y. N. Xia, Science **298**, 2176 (2002).

[38] B. Wiley, Y. G. Sun, B. Mayers, Y. N. Xia, Chem-Eur J **11**, 454 (2005).

[39] J. S. Kim, J Ind Eng Chem **13**, 566 (2007).

[40] C. M. Soukoulis, M. Wegener, Nat Photonics **5**, 523 (2011).

[41] M. M. Mariscal, J. J. Velazquez-Salazar, M. J. Yacaman, Crystengcomm **14**, 544 (2012).

[42] A. Thiaville, J. Miltat, Science **284**, 1939 (1999).

[43] T. Bein, G. D. Stucky, Chemistry of Materials **8**, 1569 (1996).

[44] G. A. Ozin, Advanced Materials **4**, 612 (1992).

[45] Z. H. Huang, X. L. Jiang, D. W. Guo, N. Gu, J Nanosci Nanotechno **11**, 9395 (2011).

[46] D. T. Schoen, A. P. Schoen, L. B. Hu, H. S. Kim, S. C. Heilshorn, Y. Cui, Nano Lett **10**, 3628 (2010).

[47] D. P. Chen, X. L. Qiao, X. L. Qiu, J. G. Chen, J Mater Sci **44**, 1076 (2009).

[48] K. J. Lee, B. H. Jun, T. H. Kim, J. Joung, Nanotechnology **17**, 2424 (2006).

[49] Z. J. Jiang, C. Y. Liu, L. W. Sun, J Phys Chem B **109**, 1730 (2005).

[50] P. Jain, T. Pradeep, Biotechnol Bioeng **90**, 59 (2005).

[51] P. Alivisatos, Nat Biotechnol **22**, 47 (2004).

[52] K. Vora, S. Kang, E. Mazur, e4399 (2012).

[53] K. Vora, S. Y. Kang, S. Shukla, E. Mazur, Appl Phys Lett **100**, (2012).

[54] K. L. Kelly, E. Coronado, L. L. Zhao, G. C. Schatz, J Phys Chem B **107**, 668 (2003).

[55] W. Haske, V. W. Chen, J. M. Hales, W. Dong, S. Barlow, S. R. Marder, J. W. Perry, Opt. Express **15**, 3426 (2007).

[56] L. Li, R. R. Gattass, E. Gershgoren, H. Hwang, J. T. Fourkas, Science **324**, 910 (2009).

[57] D. Tan, Y. Li, F. Qi, H. Yang, Q. Gong, X. Dong, X. Duan, Appl Phys Lett **90**, 071106 (2007).

[58] J. F. Xing, X. Z. Dong, W. Q. Chen, X. M. Duan, N. Takeyasu, T. Tanaka, S. Kawata, Appl Phys Lett **90**, 131106 (2007).

[59] A. N. Grigorenko, Opt. Lett. **31**, 2483 (2006).

[60] A. N. Grigorenko, A. K. Geim, H. F. Gleeson, Y. Zhang, A. A. Firsov, I. Y. Khrushchev, J. Petrovic, Nat Photon **438**, 335 (2005).

[61] V. M. Shalaev, W. Cai, U. K. Chettiar, H.-K. Yuan, A. K. Sarychev, V. P. Drachev, A. V. Kildishev, Opt. Lett. **30**, 3356 (2005).

[62] R. A. Shelby, D. R. Smith, S. Schultz, Science **292**, 77 (2001).

[63] V. M. Shalaev, Nat Photon **1**, 41 (2007).

[64] D. R. Smith, J. B. Pendry, M. C. K. Wiltshire, Science **305**, 788 (2004).

[65] F. Formanek, N. Takeyasu, T. Tanaka, K. Chiyoda, A. Ishikawa, S. Kawata, Opt. Express **14**, 800 (2006).

[66] N. Takeyasu, T. Tanaka, S. Kawata, Applied Physics A: Materials Science & Processing **90**, 205 (2008).

[67] K. Kaneko, K. Yamamoto, S. Kawata, H. Xia, J.-F. Song, H.-B. Sun, Opt. Lett. **33**, 1999 (2008).

[68] A. Ishikawa, T. Tanaka, S. Kawata, Appl Phys Lett **91**, 113118 (2007).

[69] H. H. Huang, X. P. Ni, G. L. Loy, C. H. Chew, K. L. Tan, F. C. Loh, J. F. Deng, G. Q. Xu, Langmuir **12**, 909 (1996).

[70] J. Valentine, S. Zhang, T. Zentgraf, E. Ulin-Avila, D. A. Genov, G. Bartal, X. Zhang, Nature **455**, 376 (2008).

[71] H. Y. Fan, K. Yang, D. M. Boye, T. Sigmon, K. J. Malloy, H. F. Xu, G. P. Lopez, C. J. Brinker, Science **304**, 567 (2004).

[72] N. Liu, H. C. Guo, L. W. Fu, S. Kaiser, H. Schweizer, H. Giessen, Nature Materials **7**, 31 (2008).

[73] M. Fu, K. Chaudhary, J. G. Lange, H. S. Kim, J. J. Juarez, J. A. Lewis, P. V. Braun, Advanced Materials, n/a (2013).

[74] K. S. Lee, D. Y. Yang, S. H. Park, R. H. Kim, Polym Advan Technol **17**, 72 (2006).

[75] M. Deubel, G. Von Freymann, M. Wegener, S. Pereira, K. Busch, C. M. Soukoulis, Nature Materials **3**, 444 (2004).

[76] R. Zamiri, B. Z. Azmi, H. Ahangar, G. Zamiri, M. Husin, Z. A. Wahab, Bull Mater Sci **35**, 727 (2012).

[77] C. Lee, P. Zhang*, Journal of Raman Spectroscopy **44**, 823 (2013).

[78] M. Darroudi, M. B. Ahmad, A. K. Zak, R. Zamiri, M. Hakimi, Int J Mol Sci **12**, 6346 (2011).

[79] M. Bin Ahmad, J. J. Lim, K. Shameli, N. A. Ibrahim, M. Y. Tay, Molecules **16**, 7237 (2011).

[80] F. L. DeBeukelaer, O. T. Bloom, J. T. DeRose, Industrial & Engineering Chemistry Analytical Edition **17**, 64 (1945).

[81] S. M. Eaton, H. B. Zhang, P. R. Herman, Opt Express **13**, 4708 (2005).

[82] R. R. Gattass, L. R. Cerami, E. Mazur, Opt Express **14**, 5279 (2006).

[83] B. Bruser, I. Staude, G. von Freymann, M. Wegener, U. Pietsch, Appl Optics **51**, 6732 (2012).

[84] A. V. Baryshev, V. A. Kosobukin, K. B. Samusev, D. E. Usvyat, M. F. Limonov, Physical Review B **73**, 205118 (2006).

[85] J. F. Galisteo-López, C. López, Physical Review B **70**, 035108 (2004).

[86] F. García-Santamaría, J. F. Galisteo-López, P. V. Braun, C. López, Physical Review B **71**, 195112 (2005).

[87] L. A. Dorado, R. A. Depine, H. Míguez, Physical Review B **75**, 241101 (2007).

[88] J. Fischer, M. Wegener, Opt. Mater. Express **1**, 614 (2011).

[89] M. C. Hutley, R. F. Stevens, Journal of Physics E: Scientific Instruments **21**, 1037 (1988).

[90] H. I. Smith, R. Menon, A. Patel, D. Chao, M. Walsh, G. Barbastathis, Microelectron Eng **83**, 956 (2006).

[91] E. Schonbrun, A. R. Abate, P. E. Steinvurzel, D. A. Weitz, K. B. Crozier, Lab Chip **10**, 852 (2010).

[92] T. J. DeJournett, J. B. Spicer, Phys Chem Chem Phys **15**, 19753 (2013).